

Technische Universität München  
Institut für Energietechnik

Lehrstuhl für Thermodynamik

# **Numerical Modelling of Boundary Layer Flashback in Premixed Hydrogen-Air Combustion Systems**

**Aaron Ömer Endres**

Vollständiger Abdruck der von der Fakultät für Maschinenwesen der  
Technischen Universität München zur Erlangung des akademischen Grades  
eines

DOKTOR – INGENIEURS

genehmigten Dissertation.

Vorsitzender:

Priv.-Doz. Dr.-Ing. habil. Thomas Indinger

Prüfer der Dissertation:

1. Prof. Dr.-Ing. Thomas Sattelmayer
2. Prof. Dr.-Ing. Christian Hasse

Die Dissertation wurde am 06.02.2020 bei der Technischen Universität München eingereicht  
und durch die Fakultät für Maschinenwesen am 17.06.2020 angenommen.



## **Acknowledgements**

This work was conducted during my time at the Institute of Thermodynamics of the Technical University of Munich. It was part of a project on boundary layer flashback of harmonically excited flames, which was mainly financed by the German Research Association (DFG). I gratefully acknowledge the financial support from the DFG and additional financial support from the Bavaria California Technology Center. The computing time on the Linux Cluster provided by the Leibniz Supercomputing Centre is also greatly appreciated.

I would like to thank Professor Dr.-Ing. Thomas Sattelmayer for giving me the opportunity to work at his renowned institute and for the scientific supervision of my work. I highly appreciate the balance between liberties and guidance he has given me for setting the goals of the project and finding an effective way to achieve these goals.

I am also very thankful to Professor Dr.-Ing. Christian Hasse for being the second examiner of this thesis and PD Dr.-Ing. habil. Thomas Indinger for taking over the examination presidency.

Thanks also to the colleagues at the Institute of Thermodynamics for numerous professional discussions, the good collaboration and the good overall atmosphere. Special thanks goes to Vera Hoferichter for welcoming me in the flashback research team and to Daniel Heilbronn and Pedro Romero for reviewing this thesis. I am also very thankful to Prof. Vince McDonell and his group for the warm welcome at the UC Irvine Combustion Laboratory and for making my research stay in Irvine very pleasant.

Last but not least, I would like to thank my family and friends, especially my wife Sophia, for giving me the vital personal support throughout writing this thesis.

Munich, January 2020

Aaron Endres



# Kurzfassung

Vorgemischte Verbrennung in Gasturbinen birgt das Risiko von Flammenrückschlag in die Vormischzone des Brenners. Flammenrückschlag in der Wandgrenzschicht, sogenannter Wandrückschlag, tritt besonders bei der Verwendung von wasserstoffhaltigen Brennstoffen auf. Die Vorhersage der Betriebsbedingung, unter denen Wandrückschlag auftritt, ist daher unentbehrlich für den sicheren Betrieb von Gasturbinen mit wasserstoffhaltigen Brennstoffen. Zu diesem Zweck wird in der vorliegenden Arbeit die Vorhersagbarkeit von Wandrückschlaggrenzen mit Hilfe von numerischen Simulationen untersucht. Hierzu werden Large Eddy Simulationen mit detaillierter Chemie, einem detaillierten Diffusionsmodell und dem quasi-laminaren Verbrennungsmodell angewandt. Die Simulationen des eingeschlossenen und nicht eingeschlossenen Wandrückschlags zeigen, dass der gewählte Modellierungsansatz geeignet ist, um experimentelle Rückschlaggrenzen quantitativ wiederzugeben. Des Weiteren ermöglichen die Simulationen einen detaillierten Einblick in den Rückschlagvorgang und dessen Einflussgrößen. Im eingeschlossenen Fall zeigt sich, dass der Rückschlagvorgang sowohl von globalen Parametern wie der turbulenten Flammengeschwindigkeit, als auch von lokalen Parametern wie dem lokalen Löschabstand und der Ablösung vor der propagierenden Flammenzunge stark beeinflusst wird. Im nicht eingeschlossenen Fall zeigt sich, dass der Übergang von einer nicht eingeschlossenen stabilen Flamme zu einer propagierenden eingeschlossenen Flamme direkt an der Wand stattfindet, wenn die lokale Strömungsgeschwindigkeit zeitweise von der turbulenten Flammengeschwindigkeit übertroffen wird.



# Abstract

Flame flashback into the premixing section of a burner is an inherent threat associated with premixed combustion in gas turbines. Hydrogen-containing fuels are particularly prone to flame flashback in the boundary layer (boundary layer flashback, BLF). The prediction of BLF is therefore essential for the safe operation of gas turbines with hydrogen-containing fuels. In the current work, the numerical prediction of confined and unconfined BLF limits of hydrogen-air flames is investigated by means of large eddy simulations with detailed chemical kinetics, a detailed diffusion model and the quasi-laminar combustion model. It is shown that the chosen modelling approach is capable of quantitatively reproducing experimental flashback limits. Furthermore, detailed insight into the flashback process is obtained from the numerical simulations. For confined BLF it is shown that global flame parameters as well as local effects at the leading flame tip have a significant influence on confined BLF limits and the confined flame propagation process. The numerical analysis of the transition from an unconfined to a confined flame configuration indicates that flame flashback occurs directly at the burner rim when the turbulent flame speed temporarily exceeds the local gas velocity.



# Contents

<b>1</b>	<b>Introduction</b>	<b>1</b>
1.1	Current Knowledge of Boundary Layer Flashback . . . . .	4
1.2	Prediction of Boundary Layer Flashback Limits . . . . .	8
1.2.1	Numerical Flashback Models . . . . .	8
1.2.1.1	Laminar Boundary Layer Flashback . . . . .	8
1.2.1.2	Turbulent Boundary Layer Flashback . . . . .	10
1.2.2	Analytical Flashback Models . . . . .	12
1.2.2.1	Confined Boundary Layer Flashback . . . . .	13
1.2.2.2	Unconfined Boundary Layer Flashback . . . . .	15
1.3	Scope and Structure of this Thesis . . . . .	17
<b>2</b>	<b>Lean Premixed Hydrogen Combustion</b>	<b>21</b>
2.1	Planar Laminar Premixed Flames . . . . .	21
2.2	Combustion Instabilities . . . . .	22
2.2.1	Rayleigh-Taylor Instability . . . . .	23
2.2.2	Darrieus-Landau Instability . . . . .	24
2.2.3	Thermal-diffusive Instabilities . . . . .	24
2.3	Cellular Flames in Lean Premixed Hydrogen Combustion . . . . .	27
2.4	Implications for Numerical Models of Boundary Layer Flashback	29
<b>3</b>	<b>Numerical Model for Boundary Layer Flashback</b>	<b>33</b>
3.1	Governing Equations for Reactive LES . . . . .	33
3.2	Low Mach Number Approximation for Reactive LES . . . . .	36
3.3	Governing Equations for Inert LES . . . . .	37
3.4	LES Turbulence Models . . . . .	38
3.4.1	The Smagorinsky Turbulence Model . . . . .	38
3.4.2	The Smagorinsky Turbulence Model in OpenFOAM . . . . .	39

---

3.4.3	The Dynamic One-Equation Model . . . . .	41
3.4.4	Implicit Turbulence Modelling . . . . .	43
3.5	Turbulent Combustion Modelling . . . . .	44
3.6	Transport Properties . . . . .	49
3.6.1	Species Diffusion Model . . . . .	49
3.6.2	Thermal Diffusivity Calculation . . . . .	51
3.6.3	Molecular Viscosity Calculation . . . . .	51
<b>4</b>	<b>Inert LES of Turbulent Duct Flow</b>	<b>53</b>
4.1	Numerical Setup for Inert LES . . . . .	53
4.1.1	Discretization Schemes . . . . .	54
4.1.2	Computational Grid for Channel Simulations . . . . .	54
4.1.3	Computational Grid for Pipe Simulations . . . . .	56
4.1.4	Turbulence Model Parameters . . . . .	57
4.2	Results of Inert LES . . . . .	58
4.2.1	Inert Duct Flow with the Smagorinsky Turbulence Model	58
4.2.1.1	Inert Channel Flow . . . . .	58
4.2.1.2	Inert Pipe Flow . . . . .	62
4.2.2	Duct Length Influence . . . . .	63
4.2.3	Turbulence Model Influence on Low Reynolds Number Flow . . . . .	66
4.2.4	Summary of Inert LES Results . . . . .	68
<b>5</b>	<b>Reactive LES of Confined Boundary Layer Flashback</b>	<b>69</b>
5.1	Numerical Setup for Confined Flashback Simulations . . . . .	69
5.1.1	Computational Grid and Boundary Conditions . . . . .	70
5.1.2	Procedure for Confined Flashback Simulations . . . . .	72
5.2	Confined Flashback at Atmospheric Pressure . . . . .	73
5.2.1	Confined Boundary Layer Flashback Process . . . . .	73
5.2.2	Confined Boundary Layer Flashback Limits at Atmo- spheric Pressure . . . . .	78
5.2.3	Validity of the Results . . . . .	79
5.2.4	Influence of Molecular Diffusion on Hydrogen Combustion	83
5.2.5	Inert Channel Size Influence on Flashback Results . . . . .	89
5.3	Pressure Influence on Confined Boundary Layer Flashback . . . . .	90

5.3.1	Pressure Influence on Confined Flashback Limits . . . . .	93
5.3.2	Macroscopic Flame Structure . . . . .	94
5.3.3	Average Flame Shape and Turbulent Flame Speed . . . . .	97
5.3.4	Average Pressure and Velocity Fields . . . . .	99
5.3.5	Quenching Distance and Local Boundary Layer Separation	103
5.4	Implications for Analytical Flashback Prediction . . . . .	108
5.5	Summary of Confined BLF Results . . . . .	110
<b>6</b>	<b>Reactive LES of Unconfined Boundary Layer Flashback</b>	<b>113</b>
6.1	Numerical Setup for Unconfined Flashback Simulations . . . . .	113
6.2	Stable Combustion . . . . .	116
6.3	The Unconfined Boundary Layer Flashback Process . . . . .	120
6.3.1	Flame Quenching during Unconfined Flashback . . . . .	124
6.3.2	Comparison with Experimental Results . . . . .	125
6.3.3	Comparison with Analytical Boundary Layer Flashback Models . . . . .	126
<b>7</b>	<b>Summary and Conclusions</b>	<b>129</b>



# List of Figures

1.1	Critical gradient model. . . . .	4
1.2	Confined flashback model according to Eichler. . . . .	6
1.3	Unconfined flashback model according to Baumgartner. . . . .	6
2.1	Planar laminar lean premixed hydrogen-air flame. . . . .	22
2.2	Darrieus-Landau instability. . . . .	25
2.3	Thermal-diffusive instabilities. . . . .	25
2.4	Spectrum of turbulent kinetic energy density $E_l$ as a function of the inverse eddy size $l_E$ . . . . .	30
3.1	Combustion regime diagram for LES. . . . .	47
4.1	Computational domain for inert channel simulations. . . . .	55
4.2	Computational domain for inert pipe simulations (a) and spatial discretization of the inlet (b). . . . .	57
4.3	Average velocity profiles of the turbulent channel flow compared to DNS results of Moser et al. [110]. . . . .	60
4.4	Turbulent kinetic energy profiles of the turbulent channel flow compared to DNS results of Moser et al. [110]. . . . .	61
4.5	Average velocity profile and turbulent kinetic energy profiles of the turbulent pipe flow compared to DNS results of El Khoury et al. [37]. . . . .	63
4.6	Duct length influence on turbulent kinetic energy profiles of the turbulent channel flow at $U_b = 6\text{ms}^{-1}$ and $U_b = 10\text{ms}^{-1}$ compared to DNS results of Moser et al. [110]. . . . .	65

4.7	Turbulence model influence on average velocity and turbulent kinetic energy profiles of the turbulent channel flow at $U_b = 6 \text{ ms}^{-1}$ compared to DNS results of Moser et al. [110] at $\text{Re}_\tau = 180$ .	67
5.1	Computational domain and expected confined stable flame shape.	71
5.2	Stable flame front and flashback at $U_b = 6 \text{ ms}^{-1}$ .	74
5.3	Top view of upstream flame propagation at $U_b = 20 \text{ ms}^{-1}$ and $\Phi = 0.55$ .	75
5.4	Top view of upstream flame propagation at $U_b = 20 \text{ ms}^{-1}$ and $\Phi = 0.60$ .	77
5.5	Confined boundary layer flashback limits at atmospheric pressure compared to experimental flashback limits obtained by Eichler [36].	79
5.6	LES combustion regimes at atmospheric pressure.	81
5.7	Atmospheric flame thickness profiles at flashback conditions . .	83
5.8	Average stable flame shape at $U_b = 10 \text{ ms}^{-1}$ and $\Phi = 0.38$ with one and two cell splits.	84
5.9	JPDF of hydrogen mass fraction and temperature at $U_b = 10 \text{ ms}^{-1}$ and $\Phi = 0.38$ .	85
5.10	Influence of Soret diffusion on the average flame shape and turbulent flame speed at $U_b = 10 \text{ ms}^{-1}$ and $\Phi = 0.38$ .	87
5.11	Median of the JPDFs of hydrogen reaction rate and temperature and of $Y_{\text{H}}$ and temperature with and without Soret diffusion. . .	88
5.12	LES combustion regimes at subatmospheric and elevated pressures.	92
5.13	Pressure influence on numerical confined BLF limits.	93
5.14	Instantaneous flame fronts during flashback at different pressure levels.	95
5.15	Flame thickness profiles at flashback conditions for different pressure levels.	96
5.16	Pressure influence on the laminar flame thickness.	96
5.17	Effective equivalence ratios at the highest stable equivalence ratios.	98
5.18	Stable average flame shapes at different pressure levels.	98

5.19	Normalized turbulent flame speed profiles at different bulk velocities and pressure levels. . . . .	100
5.20	Average streamlines, flame shape and pressure field at the highest stable equivalence ratio at $U_b = 10 \text{ ms}^{-1}$ . . . . .	101
5.21	Flow deflection mechanism ahead of a confined flame front. . .	101
5.22	Hydrogen reaction rate and flame separation zone at one time step during (a) upstream flame propagation and (b) flame washout at $U_b = 20 \text{ ms}^{-1}$ and $p = 1 \text{ bar}$ . . . . .	104
5.23	Flame front position, local separation zone size and average quenching thickness during flame flashback. . . . .	105
5.24	Hydrogen reaction rate and flame separation zone at one time step during upstream flame propagation at $U_b = 10 \text{ ms}^{-1}$ and $p = 0.5 \text{ bar}$ . . . . .	106
5.25	Wall-normal average pressure profile ahead of the flame front. .	109
6.1	Computational domain for unconfined flashback simulations with the expected stable flame shape (a) and spatial discretization at the premixing tube inlet (b). . . . .	114
6.2	Average streamlines, flame shape and pressure field at stable conditions of the unconfined case. . . . .	117
6.3	Profiles of (a) average temperature and (b) average hydrogen mass fraction, oxygen mass fraction and equivalence ratio in the premixing tube. . . . .	118
6.4	Turbulent flame speed profile of the unconfined stable flame at $\Phi = 0.5$ and axial velocity profile in the premixing tube. . . . .	120
6.5	Unconfined flashback process. . . . .	122
6.6	Hydrogen reaction rate and separation zone during unconfined BLF. . . . .	123



# List of Tables

3.1	Polynomial coefficients for species thermal diffusivities $\alpha_k$ . . . .	52
4.1	Initial simulation parameters for the inert channel simulations.	56
4.2	Channel flow results of LES with the Smagorinsky turbulence model. . . . .	59
4.3	Channel length influence on inert LES results with the Smagorinsky turbulence model. . . . .	65
5.1	Parameters for the atmospheric combustion regime analysis. . .	80
5.2	Parameters for the combustion regime analysis at subatmospheric and elevated pressure. . . . .	92
5.3	Quenching and separation parameters at flashback conditions.	107



# Nomenclature

## Latin Symbols

$a_f$	Filter dependent constant for dissipation rate	–
$A$	Area	$m^2$
$A_r$	Pre-exponential factor of reaction r	–
$A_S$	Sutherland coefficient	$kg/(m s K^{0.5})$
$A^+$	Van Driest damping model constant	–
$b_{p,k}$	Polynomial coefficient for species thermal diffusivity	–
$c$	Reaction progress variable	–
$c_k$	Smagorinsky model constant in OpenFOAM	–
$c_K$	Kolmogorov constant	–
$c_p$	Isobaric specific heat capacity	$J/(kg K)$
$c_S$	Smagorinsky constant	–
$c_{ht}$	Coefficient for heat transfer profile	–
$c_\Delta$	Van Driest damping model constant	–
$c_\epsilon$	Model constant for dissipation rate	–
$d$	Tube diameter	m
$d_h$	Hydraulic duct diameter	m
$D$	Global mixture diffusion coefficient	$m^2/s$
$D_k$	Diffusivity of species k	$m^2/s$
$D_k^T$	Soret diffusion coefficient of species k	$m^2/s$
$D_{s,k}$	Binary diffusion coefficient of species s through species k	$m^2/s$
$e$	Pressure exponent of the laminar flame speed	–
$E$	Activation energy	$J/mol$
$E_l$	Density of turbulent kinetic energy	$m^3/s^2$
$f$	Pipe friction factor	–
$g$	Stratford exponent	–

$h_{f,k}^0$	Specific enthalpy of formation of species k	J/kg
$h_s$	Specific sensible enthalpy	J/kg
$j_{k,i}$	Diffusion mass flux of species k in direction i	kg/(m <sup>2</sup> s)
$j_{k,i}^T$	Soret diffusion mass flux	kg/(m <sup>2</sup> s)
$j_{k,i}^Y$	Diffusion mass flux due to species mass fraction gradients	kg/(m <sup>2</sup> s)
$k$	Total kinetic energy	m <sup>2</sup> /s <sup>2</sup>
$k_B$	Boltzmann constant	J/K
$k_{DNS}$	Turbulent kinetic energy of DNS	m <sup>2</sup> /s <sup>2</sup>
$k_{res}$	Resolved turbulent kinetic energy of LES	m <sup>2</sup> /s <sup>2</sup>
$k_{tot}$	Total turbulent kinetic energy of LES	m <sup>2</sup> /s <sup>2</sup>
$k_r^b$	Backward reaction rate constant	
$k_r^f$	Forward reaction rate constant	
$K_r$	Equilibrium constant of reaction r	–
$l_\delta$	Reaction zone thickness or inner flame length scale	m
$l_E$	Eddy size	m
$l_f$	Laminar flame length scale	m
$l_S$	Smagorinsky length scale	m
$L$	Length	m
$m$	Mass	kg
$m_k$	Mass of species k	kg
$n$	Pressure exponent for flashback equivalence ratio	–
$N_p$	Number of polynomial coefficients for thermal diffusivity	–
$N_s$	Number of species	–
$p$	Pressure	Pa
$p_d$	Fluid dynamic pressure	Pa
$p_0$	Thermodynamic pressure	Pa
$P$	Turbulent kinetic energy production	kg/(m s <sup>3</sup> )
$\dot{q}$	Specific heat release rate	W/m <sup>3</sup>
$q_i$	Energy flux	W/m <sup>2</sup>
$r$	Radial coordinate	m
$R$	Universal gas constant	J/(mol K)
$s_f$	Flame speed	m/s
$s_{l,0}$	Laminar flame speed	m/s
$s_t$	Turbulent flame speed	m/s

## Nomenclature

---

$S$	Strain rate	1/s
$S_{ij}$	Strain rate tensor	1/s
$t$	Time	s
$t_f$	Laminar flame time scale	s
$t_\eta$	Time scale of Kolmogorov eddies	s
$T$	Temperature	K
$T_{ad}$	Adiabatic flame temperature	K
$T_S$	Sutherland temperature	K
$T_0$	Reference temperature	K
$T^*$	Dimensionless temperature	–
$u$	Velocity	m/s
$u_i$	Velocity component in direction i	m/s
$u_\tau$	Friction velocity	m/s
$u_{\tau,LES}$	Friction velocity from LES	m/s
$u_{\tau,Pope}$	Friction velocity according to Pope	m/s
$U_b$	Bulk velocity	m/s
$U_c$	Centerline velocity	m/s
$V_c$	Cell volume	m <sup>3</sup>
$W$	Mixture molar mass	kg/kmol
$W_k$	Molar mass of species k	kg/kmol
$x$	Axial position	m
$x_i$	Cartesian coordinate i	m
$X_k$	Mole fraction of species k	–
$y$	Wall-normal distance	m
$y_s$	Separation zone size	m
$Y_k$	Mass fraction of species k	–
$z$	Lateral position	m

## Greek Symbols

$\alpha$	Mixture thermal diffusivity	m <sup>2</sup> /s
$\alpha_k$	Thermal diffusivity of species k	m <sup>2</sup> /s
$\beta_r$	Temperature exponent of reaction r	–
$\delta$	Half channel height	m

$\delta_f$	Flame thickness	m
$\delta_{ij}$	Kronecker delta	–
$\delta_q$	Quenching distance	m
$\Delta$	Filter width	m
$\widehat{\Delta}$	Test filter width	m
$\Delta H_2$	Hydrogen consumption in a cell	1/m
$\gamma_{s,r}$	Third body efficiency of species s in reaction r	–
$\epsilon$	Turbulent kinetic energy dissipation rate	kg/(m s <sup>3</sup> )
$\epsilon_s$	Characteristic Lennard-Jones energy of species s	J
$\zeta_{global}$	Global flame brush angle	°
$\zeta_{local}$	Local flame brush angle	°
$\eta$	Kolmogorov length scale	m
$\kappa$	Von Karman constant	–
$\lambda$	Thermal conductivity	W/(mK)
$\mu$	Dynamic viscosity	kg/(m s)
$\nu$	Kinematic viscosity	m <sup>2</sup> /s
$\nu'_{s,r}$	Forward stoichiometric coefficient	–
$\nu''_{s,r}$	Backward stoichiometric coefficient	–
$\xi$	Weight for the mixture Lewis number calculation	–
$\Xi$	Arbitrary chemical symbol	–
$\rho$	Density	kg/m <sup>3</sup>
$\sigma_k$	Collision diameter of species k	Å
$\tau_{ij}$	Viscous stress tensor	N/m <sup>2</sup>
$\phi$	Arbitrary field variable	–
$\varphi$	Circumferential angle	–
$\Phi$	Equivalence ratio	–
$\Phi_{eff}$	Effective equivalence ratio	–
$\Phi_{FB}$	Flashback equivalence ratio	–
$\dot{\omega}_k$	Chemical reaction rate of species k	kg/(m <sup>3</sup> s)
$\Omega$	Collision integral	–

### Subscripts

$b$	Burnt
$dev$	Deviatoric part of a tensor
$f$	At the flame front
$F$	Fuel
$FB$	At flashback conditions
$global$	Global quantity averaged over the duct height
$inc$	Incompressible
$O$	Oxidant
$r$	At the burner rim
$st$	Stoichiometric
$u$	Unburnt
$W$	Evaluated at the wall
$\infty$	Far upstream

### Superscripts

$\bar{\phantom{0}}$	Filtered
$\tilde{\phantom{0}}$	Favre filtered
$\hat{\phantom{0}}$	Test filtered
$\phantom{0}'$	Fluctuating component
$\phantom{0}^+$	Non-dimensional value
$\langle \phantom{0} \rangle$	Average

### Dimensionless Numbers

$Ka$	Karlovitz number
$Ka_\delta$	Inner flame length scale Karlovitz number
$Le$	Mixture Lewis number
$Le_k$	Lewis number of species $k$
$Pe_q$	Quenching Peclet number
$Pr$	Prandtl number
$Re$	Reynolds number

$Re_\tau$	Friction Reynolds number
Sc	Schmidt number
Ze	Zeldovich number

**Acronyms**

CIVB	Combustion-induced vortex breakdown
DNS	Direct numerical simulation
JPDF	Joint probability density function
LES	Large eddy simulation
PDF	Probability density function
SGS	Subgrid scale
STF	Sub test filter
TKE	Turbulent kinetic energy

# 1 Introduction

In 2015, the Paris Agreement was adopted by the parties to the United Nations Framework Convention on Climate Change [112]. The agreement established the goal to limit global warming to a maximum of 2 °C compared to pre-industrial levels and further to make efforts to limit the temperature rise to 1.5 °C. According to the World Energy Outlook 2017 [74] the 2 °C goal can only be achieved if the global anthropogenic greenhouse gas emissions are balanced with their removal by the year 2100 at the latest. It is thus important to reduce anthropogenic emissions while simultaneously removing greenhouse gases from the atmosphere. CO<sub>2</sub> can be removed from the atmosphere for example by afforestation or carbon capture and storage (CCS) technologies. Burning hydrogen-rich synthetic fuels in gas turbines prevents the release of CO<sub>2</sub> in the first place. Hydrogen-rich synthetic fuels can be produced by reforming or gasification of hydrocarbon fuels. During this synthesis process, the original fuel is decarbonized which prevents the formation of CO<sub>2</sub> during combustion. The CO<sub>2</sub> produced during the synthesis process on the other hand can be captured and stored prior to the combustion process [9, 143].

Another measure to reduce anthropogenic CO<sub>2</sub> emission is the exploitation of renewable energy resources for power production. Power production from renewable energy resources and the power demand are naturally subject to strong fluctuations [54]. Potential periods of power shortage can be prevented by power-to-gas technologies. In times of excess power output hydrogen is produced via electrolysis [139]. The produced hydrogen can either be converted into methane and fed into the natural gas grid [54], or directly used for power production in gas turbines when required [143].

Lean premixed combustion is usually applied in modern gas turbines in order to meet the low NO<sub>x</sub> emission levels prescribed by regulations [128]. In pre-

mixed combustion, fuel and oxidizer are mixed in the premixing section of the gas turbine combustor prior to combustion. This leads to a homogeneous lean mixture and low local flame temperatures, which reduces  $\text{NO}_x$  emissions compared to non-premixed flames without dilution. The drawback of this method is that flammable gas mixtures prevail in regions upstream of the combustion chamber. This leads to the risk of flame propagation or flame flashback into the premixing section of the burner. As the premixing section is not designed to endure high temperatures, flame flashback can cause critical damage to the gas turbine [101] or require engine shutdown. It is thus important to understand the mechanisms leading to flame flashback and predict the operating conditions under which flashback potentially occurs.

Four different mechanisms leading to flashback have been identified so far: turbulent flame propagation in the core flow, boundary layer flashback (BLF), flashback due to combustion instabilities and flashback due to combustion-induced vortex breakdown (CIVB) [47, 102, 137].

Turbulent flame propagation in the core flow occurs when the turbulent flame speed exceeds the local gas velocity. Hydrogen has higher laminar and turbulent flame speeds than hydrocarbon fuels, which makes hydrogen flames more susceptible to flame propagation in the core flow [102]. However, for a well designed premixing section without strong wakes or high turbulence regions it is unlikely that the turbulent flame speed exceeds the core flow velocity [86, 102]. Turbulent flame propagation in the core flow is thus not a critical mechanism for flame flashback [102].

In contrast to the high gas velocities in the core flow, low gas velocities prevail near the walls of the premixing duct. In addition, high turbulence levels in the boundary layer lead to high turbulent flame speeds. The combination of low gas velocities and high flame speeds promotes flashback in boundary layers [102]. Flame quenching at cold walls usually prevents propagation of hydrocarbon flames directly at the wall [102]. Hydrogen however has high flame speeds and a high reactivity near walls. This makes BLF a critical flashback mechanism in premixed combustion systems with hydrogen-rich fuels [23, 57].

---

The third flashback mechanism is flashback due to combustion instabilities. Combustion instabilities lead to a periodic drop of the bulk velocity in the premixing duct and to periodic vortex shedding at the edge of the premixing duct. This periodically lifts the flame into the premixing duct [84, 102, 137]. If the frequency of the instabilities is low enough, the flame is not flushed out of the premixing duct but propagates upstream in the boundary layer of the premixing duct [102, 137]. The initiation of flashback due to combustion induced instabilities is thus followed by flame propagation similar to BLF. This is confirmed by the investigation of acoustically excited flames by Hoferichter and Sattelmayer [72]. They showed that the flashback tendency of unconfined flames increases under acoustic excitation. The flashback limits of acoustically excited unconfined flames approach the confined BLF limits of the same burner without acoustic excitation. The flashback safety of a burner which exhibits acoustic instabilities is thus restricted by the BLF limits of confined flames.

Flashback due to CIVB exclusively occurs in swirl-stabilized burners. Here, the flame is stabilized in the recirculation zone caused by vortex breakdown at the sudden area increase from the premixing section to the combustion chamber [69, 90]. The recirculation zone and vortex breakdown are influenced by the pressure and density gradients due to combustion [87, 89, 90, 102]. By increasing the equivalence ratio or reducing the mixture mass flow, the reaction zone thickness decreases and the reaction zone moves towards the stagnation point at the upstream tip of the recirculation zone. This in turn increases the induced negative axial velocities in the recirculation zone due to baroclinic torque. At a critical equivalence ratio or mixture mass flow, the negative axial velocity in the recirculation zone is large enough for the flame and the vortex breakdown to propagate upstream into the premixing section, thus initiating flashback [87, 89]. As soon as the flame reaches the walls of the premixing duct, combustion-induced vortex breakdown is typically followed by BLF [4, 108, 126].

To summarize, BLF is highly relevant for the safe operation of burners with hydrogen-rich fuels. BLF is therefore investigated in the current work. The focus here is on BLF in non-swirling flows without acoustic excitation. In order

to establish the detailed scope of this work, the current knowledge of BLF is briefly presented in the following section. This is followed by an analysis of the existing flashback prediction models. Finally, the scope and goals of this work are given.

## 1.1 Current Knowledge of Boundary Layer Flashback

An early groundbreaking work on BLF was presented by Lewis and von Elbe in 1943 [97]. They investigated the stability of laminar natural gas-air flames in tube burners experimentally. Based on their results, they developed the critical gradient model for BLF. The critical gradient model states that BLF occurs when the local flame speed  $s_f$  exceeds the local axial gas velocity  $u_x$  at some penetration distance  $\delta_p$  from the wall. When assuming a linear velocity profile at the wall, this condition for BLF can be reformulated in terms of the velocity gradient at the wall,

$$g = \left. \frac{\partial u_x}{\partial y} \right|_w = \frac{s_f(\delta_p)}{\delta_p}, \quad (1.1)$$

as depicted in Figure 1.1. Flashback occurs when the velocity gradient at the wall is smaller than a critical velocity gradient given by the quotient of flame speed and penetration thickness.

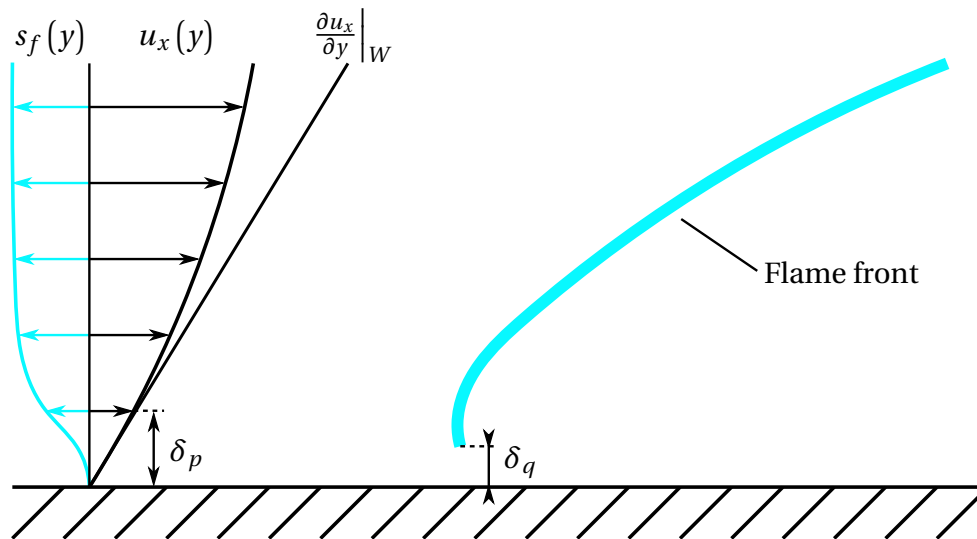


**Figure 1.1:** Critical gradient model. Adapted from [36].

The critical gradient model has been used in multiple studies to quantify the influencing parameters on the flashback propensity of laminar and turbulent flames [79]. Lee and T'ien [95] however noticed in early simulations that confined flames induce a pressure rise ahead of the flame front which deflects the streamlines in the fresh gas. The critical gradient model conversely presumes an undisturbed velocity profile in the boundary layer. This was the first indication that the critical gradient model is not valid when the flame is confined inside a duct. Later Heeger et al. [65] experimentally detected boundary layer separation zones during upstream propagation of flames inside the premixing duct of a swirl burner. Eichler et al. [34, 36] experimentally investigated the influence of flame confinement on the flashback characteristics of a backward facing step burner with rectangular cross section. They changed the step height of the burner in order to gradually change the configuration from an unconfined flame stabilized at the downstream end of the premixing channel to a confined flame stabilized inside the channel. In the latter case, the flame was stabilized by a flush hot ceramic tile. They concluded that flame confinement substantially changes the critical velocity gradients and the flashback characteristics. With optical measurement techniques, they identified a strong interaction between the confined flame and the approaching boundary layer flow. The assumptions of an undisturbed boundary layer are thus not fulfilled in confined BLF and the critical gradient model can not be applied. Eichler [34, 36] therefore developed a new model for confined BLF, which is depicted in Figure 1.2. Combustion induces a pressure rise ahead of the leading flame front, which leads to boundary layer separation and the formation of a recirculation zone. When the separation zone size  $y_s$  exceeds the quenching thickness  $\delta_q$ , the flame can anchor inside the separation zone and flashback occurs [34].

On the basis of the experiments of Eichler et al. [34, 36], Baumgartner et al. [3, 5] experimentally investigated the transition mechanism from an unconfined flame stabilized at the exit of a rectangular channel burner to flame propagation inside the premixing duct. In contrast to the confined case, it was found that the flame does not influence the velocity profile in the boundary layer upstream of the burner rim. The critical gradient model was nevertheless found to be invalid in the unconfined case as well. Figure 1.3 depicts the sta-

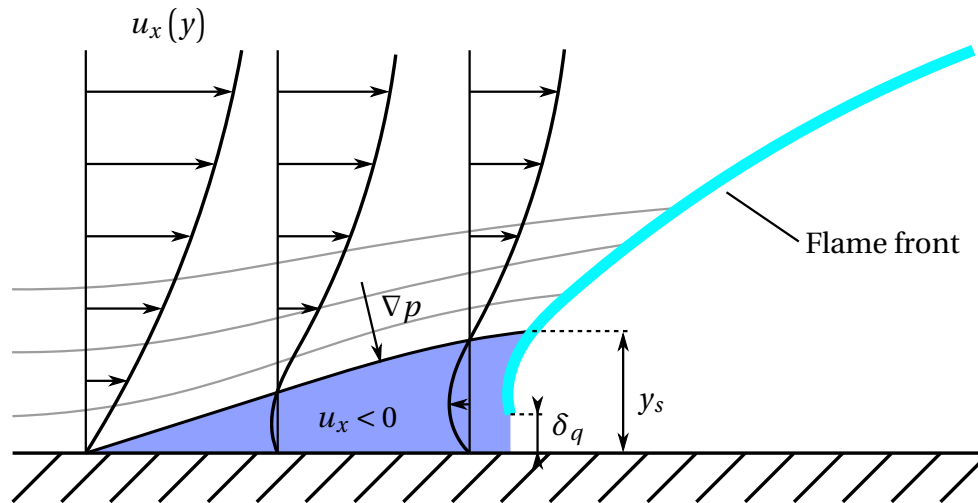


**Figure 1.2:** Confined flashback model according to Eichler. Streamlines are depicted in gray. The dark blue region is the separation zone. Adapted from [36].

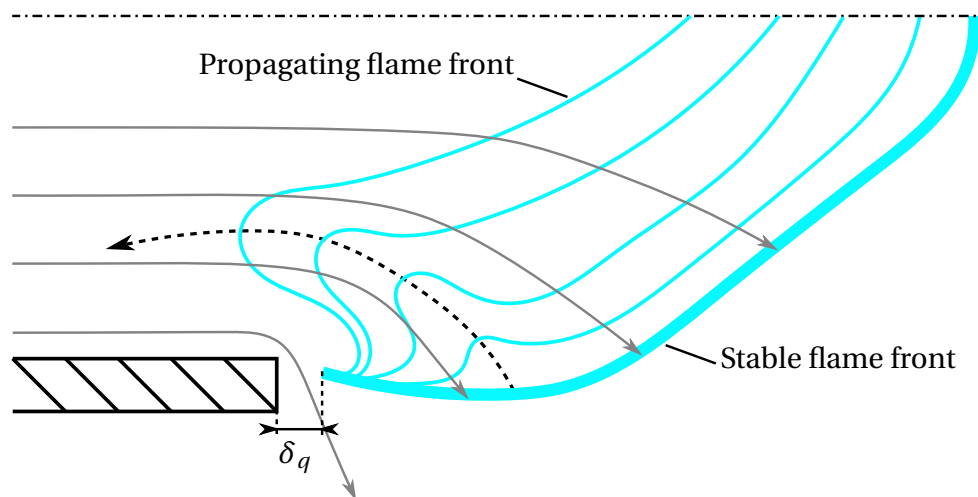


**Figure 1.3:** Unconfined flashback model according to Baumgartner. Streamlines are depicted in gray. The black dashed line depicts the formation point of the initial flame cusp and the propagation path of the leading flame tip. Adapted from [5].

ble flame shape and the transition process to flame propagation as observed by Baumgartner et al. with optical measurement techniques. The flame front is stabilized at the exit of the premixing duct. The offset between the burner rim and the stable flame front is the quenching distance  $\delta_q$ . Flame quenching at the burner rim allows for fresh gas to leak through the quenching gap without being directly consumed. Downstream of the burner rim, the stable flame shape is first bent outwards before adapting to the common cone shape. When increasing the equivalence ratio beyond the flashback limit, upstream flame propagation is initiated by the formation of a flame cusp. After the initial flame cusp formation, the flame approximately follows the dashed propagation path in Figure 1.3. The burner rim distance of the initial flame cusp and the flame front trajectory observed by Baumgartner et al. was significantly larger than the quenching distance. This flame tip trajectory and the gap flow between the stable flame and the burner rim are not represented by the critical gradient model. The critical gradient model is therefore also not applicable to unconfined BLF according to Baumgartner [5]. The reason for the peculiar stable flame shape and for the initiation of BLF at a certain distance away from the burner rim remains unclear [5].

Besides the phenomenological investigation of the boundary layer flashback process, studies have been conducted on different influencing parameters on flashback limits. The influence of preheat temperature [31, 43, 45, 85], burner rim temperature [10, 129, 131], choice of fuel [60, 61, 129, 142], burner diameter [23, 44, 46] and pressure [43–45, 149] have been investigated amongst others. A detailed and comprehensive review on flashback literature is given by Kalantari and McDonnell [79]. Hoferichter and Sattelmayer [72] investigated the influence of acoustic excitation on BLF limits of unconfined flames. They concluded that with increasing acoustic excitation, the flashback propensity of unconfined flames increases and approaches the flashback propensity of confined flames without acoustic excitation. In the presence of thermoacoustic instabilities, the confined case of BLF is thus the critical case for the flashback propensity of a burner.

Elevated pressure levels are very common in gas turbine combustion. Daniele et al. [24] and Kalantari et al. [80] therefore investigated the influence of pres-

sure on unconfined BLF limits. Their experiments showed a strong influence of pressure on the measured flashback limits. Daniele et al. [24] estimated the pressure influence on different combustion parameters from literature data. They concluded that the pressure influence on flashback limits is mainly driven by the pressure influence on the quenching distance. The pressure influence on confined boundary layer flashback, on the other hand, has not been investigated so far.

## **1.2 Prediction of Boundary Layer Flashback Limits**

For the safe and economical operation of gas turbines it is important to assess the flashback propensity at different operating conditions. Different numerical simulations have been carried out in order to predict the flashback limits of confined and unconfined flames. Furthermore, analytical flashback prediction models have been developed based on experimental results. The different numerical and analytical tools for flashback prediction are presented in the following.

### **1.2.1 Numerical Flashback Models**

#### **1.2.1.1 Laminar Boundary Layer Flashback**

Lee and T'ien [95] made first attempts to numerically predict laminar BLF limits. They modelled combustion of stoichiometric methane flames confined inside a pipe with a stationary solver and single-step finite-rate chemistry. The velocity at the inlet of the two-dimensional computational domain was adapted to obtain a stationary flame. The critical velocity gradient for BLF was then obtained from the velocity profile at stationary conditions. The resulting critical velocity gradients were generally higher than the experimental BLF limits of unconfined flames. Although the flashback propensity was overestimated by these early numerical simulations, they allowed for a detailed insight into the flashback process. It was noted that the confined configuration in the numerical simulations is the main reason for the discrepancy between

the numerical and experimental flashback limits. They observed that in confined BLF, the two-dimensional flame shape generates a back pressure ahead of the flame front. This back pressure in turn deflects the streamlines ahead of the flame front. However, no backflow regions were observed in these simulations. The formation of backflow regions was probably prevented by the limited size of the computational domain [36].

Kurdyumov et al. [92] presented steady two-dimensional simulations of a stationary confined flame in a moving reference frame. Combustion was modeled with single-step chemistry of an arbitrary fuel with variable heat release rate, activation energy and Lewis number. The duct wall was modeled as an adiabatic wall in one configuration and as an isothermal wall in a second configuration. The numerical results were compared to experimental results of unconfined BLF of lean propane-air and methane-air flames. The flow structure observed in the numerical simulations was similar to the flow structure observed in the experiments. Kurdyumov et al. stated that the numerically predicted flashback limits were primarily influenced by the thermal boundary condition. The heat release rate and the activation energy on the other hand only had a limited effect on the predicted flashback limits. Furthermore, they found that the experimental flashback limits are between the numerical solutions with adiabatic walls and with isothermal walls. It was therefore concluded that the simulation results are in reasonable agreement with the experimental results. It was however not taken into account that the numerical simulations represented the confined case of BLF, while the experimental data was obtained from unconfined flashback events. This prohibits the comparison of the numerical and experimental flashback limits and the conclusion that the crude combustion model with single-step chemistry accurately captures all relevant physical effects.

Mallens and de Goey [106] used a steady solver for modelling the unconfined case of laminar BLF. The numerical simulations were initialized with methane-air flame stabilized at the exit of a two-dimensional axisymmetrical duct. Combustion was again modeled with single-step finite-rate chemistry. Flashback limits were obtained by continuously decreasing the inlet velocity until the numerical solution failed to converge as the flame propagated into

the burner duct. The numerically obtained critical gradients had a deviation of only 10 % from critical gradients obtained from experiments with a similar tube burner. Despite the steady solver and the single-step chemistry, the simulations by Mallens and de Goey were thus the first to accurately reproduce experimental laminar flashback limits in a quantitative manner.

Eichler [36] carried out unsteady simulations of confined boundary layer flashback of two-dimensional laminar hydrogen-air flames. Combustion was modelled by finite-rate chemistry with three reactions and five species. Similar to his experimental setup, the confined flame was initially stabilized by a hot surface. The surface temperature was set to the adiabatic flame temperature. The equivalence ratio of the gas mixture was increased until upstream flame propagation into the premixing channel with cold isothermal walls began. These simulations were the first to reproduce the recirculation zones during BLF previously observed in experiments. Furthermore, the simulations showed that boundary layer separation even occurs when the flame is still stabilized at the hot ceramic tile prior to BLF. In addition, the pressure fields obtained from the simulations verified that the pressure rise ahead of the flame tip has a two-dimensional character and is caused by the two-dimensional nature of the flame front. The pressure rise can therefore only be predicted by two-dimensional instead of one-dimensional estimations. The numerical simulations of Eichler thus granted a detailed insight into the confined laminar boundary layer flashback process. The numerical model was however not used for reproducing experimental flashback limits.

### **1.2.1.2 Turbulent Boundary Layer Flashback**

The first numerical simulations of turbulent confined BLF in a channel were presented by Gruber et al. [57]. In these direct numerical simulations (DNS), combustion of hydrogen in air was modeled by finite-rate chemistry and a detailed chemical reaction mechanism. The initially flat flame was wrinkled by intrinsic instabilities and turbulent velocity fluctuations until upstream flame propagation began. During upstream flame propagation, high local pressure levels ahead of the convex flame bulges resulted in local zones of boundary

layer separation. The occurrence of local boundary layer separation observed in experimental studies of turbulent BLF was therefore also verified by simulations of turbulent BLF. Furthermore, the DNS results provided worthwhile information about physical parameters during upstream flame propagation. The data was used to model the mean flame shape during upstream propagation of a turbulent flame [58]. Flashback limits were however not obtained from the numerical simulations.

Lietz et al. [100] tried to reproduce DNS results similar to those of Gruber et al. [57] with large eddy simulations (LES). They used different combustion models such as the algebraic flame surface density model and tabulated chemistry with and without filtering the tabulated laminar flamelets. The comparison of the different combustion models showed that the filtered tabulated chemistry model delivered the best results. The structure of the DNS flame front was accurately predicted by the LES with tabulated chemistry. The propagation velocity of the flame front was however generally underpredicted. The algebraic flame surface density model on the other hand could be tuned to accurately predict the propagation velocity of the flame. This in turn resulted in a poor representation of the DNS flame structure. The chosen combustion models are thus not suited for accurately reproducing the upstream propagation process of a turbulent hydrogen-air flame.

LES with filtered tabulated chemistry were also applied by Clemens and Raman [18] for modelling the boundary layer flashback process in a swirl burner. Although only flashback in non-swirling flows is treated in the current work, the simulations of Clemens and Raman still provide interesting findings on modelling BLF in non-swirling flow with LES. They compared the LES results of methane-air flames and methane-hydrogen-air flames at atmospheric pressure with experimental results of a tubular swirl burner with centerbody. For pure methane-air flames, the numerical model predicted the experimentally measured flashback limit very accurately. Despite attempting to take account of the influence of heat loss and differential diffusion in the tabulated chemistry model, the LES could not accurately predict the flashback limit of methane-hydrogen-air flames. The modelling approach chosen by Clemens and Raman is therefore also not expected to accurately reproduce the flash-

back behaviour of pure hydrogen-air flames.

To summarize, previously presented numerical models have not succeeded in accurately predicting the BLF limits of turbulent hydrogen flames. Therefore, analytical flashback models have been developed based on experimental results.

### **1.2.2 Analytical Flashback Models**

The critical gradient is a non-uniform parameter which has to be determined experimentally for different burners and operating conditions [5]. The critical gradient model is therefore not useful to predict BLF limits of a new configuration. However, several attempts have been made to correlate the critical gradients of burners to non-dimensional parameters such as the Peclet number [124] and the Damköhler number [79–81, 92].

Baumgartner [5] presented the first analytical flashback prediction models which are not merely correlations to experimental flashback data. These models are based on the findings of Eichler et al. [34–36] and Baumgartner et al. [3–5] on the flashback process. Baumgartner [5] used the Stratford separation criterion [133] in combination with a one-dimensional estimation of the pressure rise ahead of the flame to predict experimental flashback limits of confined boundary layer flashback. For unconfined flashback, Baumgartner developed a prediction model with the assumption that flashback occurs when the local turbulent flame speed exceeds the minimum axial gas velocity at a certain wall distance in the turbulent boundary layer. Both models for flashback prediction delivered only poor agreement with experimental data. Hoferichter et al. [69–71] later presented analytical flashback prediction models that successfully predicted experimental flashback limits of confined and unconfined flames. These analytical flashback prediction models are presented in the following.

### 1.2.2.1 Confined Boundary Layer Flashback

Hoferichter et al. [69, 71] continued developing a prediction model for confined BLF based on the Stratford separation criterion [133] and a one-dimensional estimation of the pressure rise ahead of the flame front. The Stratford separation criterion predicts the separation point of a boundary layer which is subjected to a uniform pressure gradient. It is based on boundary layer theory and experimental data from a wind tunnel with an expanding cross section. The validity of the boundary layer theory during BLF is questionable. Eichler [36] found that the pressure rise ahead of the flame tip has a two-dimensional character. Pressure is thus not uniform in wall-normal direction. A prerequisite for the application of the boundary layer theory is however a uniform wall-normal pressure. The pressure rise ahead of the flame front was furthermore found to be underpredicted by one-dimensional approximations [36].

The analytical flashback prediction model nevertheless assumes that flashback occurs when a one-dimensional pressure rise ahead of the flame is large enough to cause boundary layer separation according to the Stratford separation criterion [69, 71]. The Stratford separation criterion was therefore reformulated to

$$\sqrt{2} \left( \frac{2\Delta p}{\rho_u U_{c,FB}^2} \right)^{3/2} = 0.39 \left( 10^{-6} \frac{U_{c,FB} x_f}{\nu_u} \right)^g \quad (1.2)$$

by assuming a quadratic pressure profile. In order to make the separation criterion independent of the axial flame position  $x_f$ , the original Stratford exponent  $g = 0.1$  was changed to  $g = 0$ . This results in the new criterion for the flashback centerline velocity  $U_{c,FB}$ ,

$$\frac{\Delta p}{\rho_u U_{c,FB}^2} = 0.0975^{2/3}. \quad (1.3)$$

The pressure rise  $\Delta p$  ahead of the flame front was derived from mass conservation,

$$\rho_f u_f = \rho_b u_b, \quad (1.4)$$

and momentum conservation,

$$\rho_f u_f^2 + p_f = \rho_b u_b^2 + p_b, \quad (1.5)$$

between the unburnt gas at the flame front  $f$  and the burnt gas  $b$ . Combining these two equations results in an equation for the pressure difference  $p_f - p_b$ :

$$p_f - p_b = \rho_f u_f^2 \left( \frac{\rho_f}{\rho_b} - 1 \right) = \rho_u u_f^2 \left( \frac{\rho_u}{\rho_b} - 1 \right). \quad (1.6)$$

The density decreases from  $\rho_f = \rho_u$  to  $\rho_b$  across the flame front. As  $\rho_u/\rho_b > 1$ , the mass and momentum conservation equations predict a pressure drop across the flame front. Hoferichter et al. [69, 71] assumed that the pressure upstream and downstream of a flame front has to be equal in isobaric combustion. The pressure drop  $p_f - p_b$  across the flame front then has to be balanced by the pressure rise  $\Delta p = p_f - p_u$  ahead of the flame front. The gas velocity at a stationary flame front is equal to the turbulent flame speed. The gas velocity  $u_f$  in equation (1.6) can therefore be replaced by the turbulent flame speed  $s_t$ . The maximum pressure rise is then obtained from the maximum turbulent flame speed  $s_{t,max}$ . For an ideal gas, where  $\rho_u/\rho_b \approx T_{ad}/T_u$  this results in the pressure rise

$$\Delta p = \rho_u s_{t,max}^2 \left( \frac{T_{ad}}{T_u} - 1 \right) \quad (1.7)$$

ahead of the flame front. The pressure rise is thus dependent on the unburnt gas density  $\rho_u$ , the maximum turbulent flame speed  $s_{t,max}$  and the expansion ratio given by the adiabatic flame temperature  $T_{ad}$  and the unburnt gas temperature  $T_u$ . The maximum turbulent flame speed is in turn obtained from the maximum stretched laminar flame speed  $s_{l,s,max}$  and the maximum turbulent velocity fluctuation  $u'_{max}$ :

$$s_{t,max} = s_{l,s,max} \left( 1 + 2.3 \left( \frac{u'_{max}}{s_{l,s,max}} \right)^{0.5} \right). \quad (1.8)$$

The turbulent velocity fluctuations for the analytical prediction model were obtained from a fitting function to experimental inert channel data. The stretched laminar flame speed was calculated from the laminar flame speed, a stretch rate and the Markstein length of the flame. Details on the exact calculation of the stretched laminar flame speed can be found in the original publication of Hoferichter et al. [71].

With the pressure rise according to Equation (1.7), the adapted Stratford criterion (1.3) leads to the flashback criterion

$$U_{c,FB} = 0.0975^{-1/3} s_{t,max} \sqrt{\frac{T_{ad}}{T_u}} - 1. \quad (1.9)$$

The turbulent flame speed also depends on the bulk velocity in the channel. Iterative procedures therefore have to be applied to obtain the flashback limits of a burner.

The flashback criterion (1.9) implies that the flashback limit is solely dependent on the maximum turbulent flame speed and the gas expansion ratio. The quenching distance however is not directly accounted for in this flashback prediction model. This contradicts the finding of Daniele et al. [24] and Kalantari et al. [80] that a large influence on flashback limits is attributed to the quenching distance. The analytical flashback prediction model nevertheless accurately predicted the experimental confined flashback limits of Eichler [36] at different preheat temperatures.

### 1.2.2.2 Unconfined Boundary Layer Flashback

Hoferichter et al. [69, 70] also developed an analytical flashback prediction model for the unconfined case of turbulent BLF. They assumed that upstream flame propagation is initiated when the local flame brush angle close to the wall is equal to or exceeds the average flame brush angle. This condition was associated with a high probability of creating an initial distortion in the flame front, which can then propagate upstream due to flame front instabilities. The analytical flashback model for unconfined flames is therefore split into a local and a global analysis of the flame angle. It is assumed that flame flashback is initiated at the wall distance of maximum turbulent flame speed,  $y_{FB}^+ = 16.4$ . The local flame angle  $\zeta_{local}$  is then obtained from the condition that the component of the axial gas velocity  $u_x$  perpendicular to the flame front is equal to the turbulent flame speed, or

$$\sin(\zeta_{local}) = \frac{s_t(y_{FB}^+)}{u_x(y_{FB}^+)} = \frac{s_{t,max}}{u_x(y_{FB}^+)}. \quad (1.10)$$

The maximum turbulent flame speed is again obtained from Equation (1.8). On the basis of experimental data of Baumgartner [5], the maximum turbulent velocity fluctuation is estimated to 1.5 times the friction velocity of the inert velocity profile.

The global turbulent flame brush angle  $\zeta_{global}$  is evaluated from the bulk velocity  $U_b$  and the global turbulent flame speed  $s_{t,global}$ ,

$$\sin(\zeta_{global}) = \frac{s_{t,global}}{U_b}. \quad (1.11)$$

The global turbulent flame speed is again obtained from equation (1.8). A global turbulent velocity fluctuation and a global stretched laminar flame speed are however used for the turbulent flame speed calculation. The global turbulent velocity fluctuation  $u'_{global,r}$  at the burner rim is estimated from the bulk velocity, the unburnt gas viscosity and the hydraulic duct diameter,

$$\frac{u'_{global,r}}{U_b} = 0.16 \left( \frac{d_h U_b}{\nu_u} \right)^{-1/8}, \quad (1.12)$$

according to the Fluent user's guide [2]. The turbulence intensity was found to rise downstream of the burner duct due to flame generated turbulence. According to Hoferichter et al. [69, 70], Liu [104] presented a correlation for flame generated turbulent velocity fluctuations:

$$\frac{u'}{u'_r} = 1 + 0.181 \left( \frac{s_{l,0}}{u'} \right)^{2.1}. \quad (1.13)$$

By adapting the constants of this correlation, Hoferichter et al. [69, 70] applied a similar correlation to obtain the global turbulent velocity fluctuation  $u'_{global}$  at the flame front,

$$\frac{u'_{global}}{u'_{global,r}} = 1 + 1.8 \left( \frac{s_{l,s,global}}{u'_{global,r}} \right)^{1.1}. \quad (1.14)$$

Compared to the original correlation of Liu [104], this new correlation significantly overestimates the flame generated turbulence for low ratios of  $s_{l,s,global}$  to  $u'_{global,r}$ . The experimental flame brush angles of turbulent flames evaluated at an arbitrary value of combustion progress were nevertheless well reproduced by the new correlation (1.14) and equation (1.11) [69, 70].

The analytical flashback prediction model is based on the assumption that flashback occurs, when the local flame angle  $\zeta_{local}$  is equal to the global flame brush angle  $\zeta_{global}$ . With equations (1.10) and (1.11) this results in the flashback criterion

$$U_{b,FB} = \frac{S_{t,global}}{s_t(y_{FB}^+)} u_x(y_{FB}^+) \quad (1.15)$$

for the bulk velocity at flashback conditions. The right hand side of the flashback criterion depends on the bulk velocity  $U_{b,FB}$ . An iterative procedure therefore has to be applied in order to obtain the flashback limits of a burner. The quenching distance does not have a direct influence on the predicted flashback limits, which contradicts the finding of Daniele et al. [24] and Kalantari et al. [80]. Hoferichter et al. [69, 70] nevertheless used this analytical model to predict the unconfined flashback limits of a tube and channel burner at ambient temperature and different preheating temperatures. The study showed that the analytical model is capable of accurately predicting experimentally obtained flashback limits.

### 1.3 Scope and Structure of this Thesis

Recent experimental, numerical and analytical studies contributed to a better understanding of the BLF process and the predictability of the corresponding flashback limits. Numerical simulations have however not yet succeeded in accurately predicting the BLF limits of confined and unconfined turbulent hydrogen flames. The goal of this work is to develop a numerical model which accurately represents the BLF process of hydrogen-air flames. This numerical model is then applied to the confined and unconfined cases of BLF in order to get a more detailed insight into the BLF process.

The influence of the quenching distance on the flashback process remains unclear from the experimental results and the analytical flashback prediction models presented in literature. Experimental studies indicate that the quenching distance has a strong influence on confined and unconfined flashback limits. In the analytical flashback prediction models however [69–71], the quenching distance does not have an effect on the predicted flashback limits.

The influence of the quenching distance on the flashback process is therefore assessed in the current project on the basis of numerical simulations. The pressure influence on the quenching distance and other combustion parameters is particularly interesting for practical applications. The pressure influence on the confined BLF process and the influencing physical parameters are therefore also investigated in the current project. These results are then utilized to revisit the analytical flashback models of Hoferichter et al. [69–71].

The transition process of unconfined flame to confined flame is not yet fully understood. Baumgartner et al. [3, 5] observed that unconfined BLF sets in at a certain distance downstream of the burner rim and not directly at the burner rim. The reason for this particular behaviour remains unclear. The propagation path in the transition process of an unconfined stable flame to BLF is therefore analyzed in detail by means of numerical simulations.

The thesis is structured as follows: Chapter 2 gives an overview of the basic principles of hydrogen combustion, which are relevant for the development of the numerical model. Chapter 3 presents the numerical model for flashback simulations of hydrogen-air flames. This is followed by inert simulation results of the turbulent base flow in Chapter 4. The inert duct flow has a strong influence on the flashback process. An accurate representation of the inert duct flow is therefore the foundation for an accurate numerical reproduction of experimental flashback limits. The reactive simulation results of confined BLF are presented in Chapter 5. The numerical setup for confined flashback simulations is first presented. The numerical setup aims at accurately representing the experimental setup of Eichler et al. [34, 36]. The model is therefore validated by comparing the numerical atmospheric flashback limits with experimental flashback limits of Eichler et al. [34, 36]. At last, the pressure influence on confined BLF is analyzed. The comparison of the simulation results at different pressure levels allows for investigating the influence of different quantities such as the turbulent flame speed, average flow deflection, the quenching distance and the local separation zone size on the flashback process. These results are then utilized to reassess the analytical flashback prediction model for confined BLF [69, 71]. The unconfined flashback process is analyzed in Chapter 6. After presenting the numerical setup for the unconfined flashback simu-

lations, the stable flame shape is analyzed and compared to experimental results. The flashback experiments of Duan, Shaffer and McDonell [29] are used as reference results for the unconfined simulations. Detailed wall temperature measurements are available from these experiments, which facilitates capturing the wall temperature influence on the flashback process. The flashback process is then investigated in regard to the propagation path and the role of the quenching distance for BLF. These results are then compared to previous BLF models. The thesis is concluded by a summary of the results and the conclusions drawn from the results.

Some of the results presented in the current thesis have already been presented in the author's previous publications [38, 39].



## 2 Lean Premixed Hydrogen Combustion

The goal of this study is to numerically investigate BLF of lean premixed hydrogen-air flames. Compared to the combustion of hydrocarbon fuels, hydrogen shows some particular combustion phenomena which have to be accounted for in the numerical model. The peculiarities of hydrogen combustion and the implications for modelling hydrogen combustion are elaborated in this chapter.

### 2.1 Planar Laminar Premixed Flames

Without the influence of heat loss, turbulence and combustion instabilities, a nearly planar flame would form inside a duct after the ignition of a quiescent combustible gas. Planar flames propagate at a constant subsonic laminar flame speed  $s_{l,0}$  [147]. Figure 2.1 shows the heat release rate, temperature and some species mass fraction profiles of a stationary freely propagating flame for hydrogen-air combustion at fuel-lean conditions. In a stationary state, fuel and oxidant enter the domain at  $x/\max(x) = 0$  with the flame propagation speed  $s_{l,0}$  [140]. The reaction products exit the flame at  $x/\max(x) = 1$  at a higher velocity. The mass fraction  $Y_k$  of species  $k$  is the mass  $m_k$  of species  $k$  in a specific volume divided by the total mass  $m$  in the same volume [119].

$$Y_k = \frac{m_k}{m} \quad (2.1)$$

The flame can be divided into the preheat zone and the reaction zone. The majority of the chemical energy is released in the reaction zone. The reaction zone of the laminar flame in Figure 2.1 approximately stretches from  $x/\max(x) = 0.4$  to  $x/\max(x) = 0.52$ . Fast chemical reactions lead to the disintegration of the fuel molecules and to the creation of highly reactive chemical

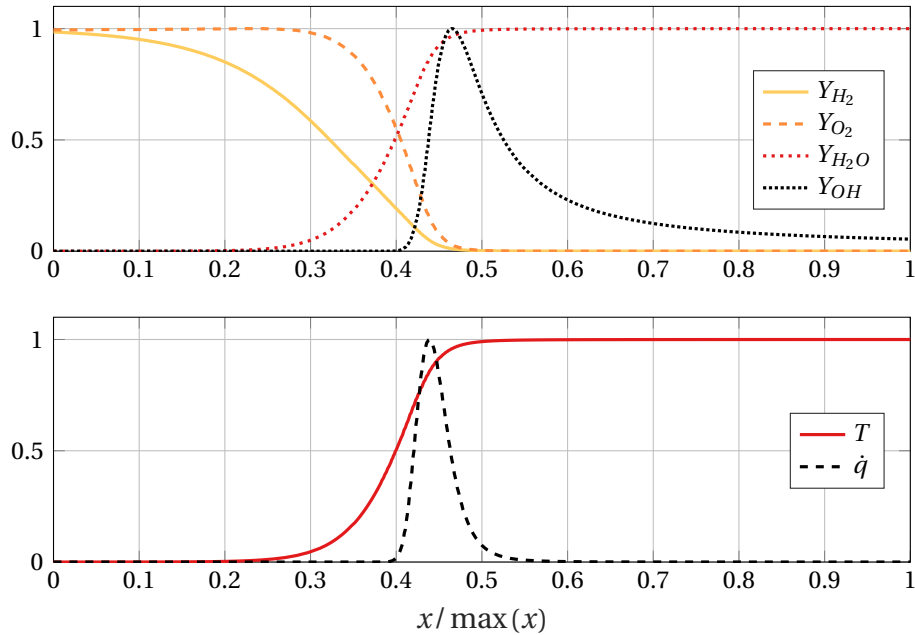


**Figure 2.1:** Planar laminar lean premixed hydrogen-air flame. Species mass fractions  $Y$ , temperature  $T$  and specific heat release rate  $\dot{q}$  are non-dimensionalized by the maximum and minimum value of their profile,  $(\phi - \min(\phi)) / (\max(\phi) - \min(\phi))$ .

radicals. This is followed by slower radical recombination reactions. The pre-heat zone is dominated by diffusion processes. Driven by temperature and species mass fraction gradients, heat and radicals diffuse into the preheat zone between  $x / \max(x) = 0.25$  and  $x / \max(x) = 0.4$ . At the same time the reactants diffuse towards the reaction zone. This initiates the chemical reactions in the fresh gas and sustains the combustion process [140].

## 2.2 Combustion Instabilities

The most significant difference between the combustion of hydrocarbon fuels and hydrogen combustion is in the manifestation of combustion instabilities. There are generally three types of instabilities that lead to the wrinkling of an initially planar flame front, which is subject to small perturbations: The Rayleigh-Taylor instability, the Darrieus-Landau instability and thermal-

diffusive instabilities [115, 147]. While the Rayleigh-Taylor instability and the Darrieus-Landau instability can occur with every fuel, thermal-diffusive instabilities primarily have a destabilizing effect on hydrogen flames.

### 2.2.1 Rayleigh-Taylor Instability

The Rayleigh-Taylor instability occurs at the interface of two fluid layers of different densities which are subjected to an acceleration perpendicular to the interface [136]. This condition is reached for example during combustion under the influence of gravitational acceleration. When the low-density burnt gas is located beneath the high-density unburnt gas in an upward propagating or burner stabilized flame, the flame front may become buoyantly unstable. The opposite configuration, where the burnt gas is located above the unburnt gas, is stabilized by buoyancy [147].

Because of the small magnitude of buoyant forces, the Rayleigh-Taylor instability is generally only relevant at very low flame speeds [147]. It is thus only relevant at the flammability limit of flames [115]. The wavelength of the Rayleigh-Taylor instability can furthermore be estimated to a few centimeters [147], which limits the direct effect on flame wrinkling in small experimental setups. The stabilizing effect of buoyancy can however suppress the occurrence of other instabilities such as thermal-diffusive instabilities when a flame is near the stability limit. Numerical simulations of Patnaik and Kailasanath [115] for example showed that gravity suppresses the occurrence of thermal-diffusive instabilities of hydrogen-air flames at a molar hydrogen content of 10%. At a molar hydrogen content of 12% however there was already no significant gravitational influence on the flame structure. In the configurations investigated in the present work, the gas mixtures are not close to the flammability limit and the molar hydrogen content is generally higher than 12%. Furthermore, the flames will be subjected to turbulent velocity fluctuations, which will increase the flame propagation speed and enforce the occurrence of thermal-diffusive instabilities by corrugating the flame front. The influence of the Rayleigh-Taylor instability and buoyancy effects are therefore expected to be negligible.

### 2.2.2 Darrieus-Landau Instability

Another instability mechanism arises when a flame, which represents a discontinuity in density, propagates towards the fresh gas of high density [93]. This hydrodynamic instability is well described by Williams [147] with Figure 2.2. In the upper part of Figure 2.2, a steadily propagating flame with propagation speed  $u_\infty$  is convexly perturbed towards the high-density fresh gas. The local gas velocity component normal to the flame front increases from  $u_{n,u}$  to  $u_{n,b}$  due to the density drop from  $\rho_u$  to  $\rho_b$  across the flame front. The tangential velocity  $u_{t,u}$  on the other hand is unchanged by the flame. This leads to streamline deflection towards the local flame normal. The perturbations in the velocity field will subside far upstream and far downstream of the flame. The stream tube areas  $A_\infty$  far upstream and far downstream of the flame thus have to be equal. Due to the streamline deflection at the flame front, the stream tube area  $A_f$  at the flame front is larger than the initial area  $A_\infty$ . From the incompressible continuity equation of a stream tube in the unburnt gas,  $A_\infty u_\infty = A_f u_f$ , it is evident that the local gas velocity at the flame front  $u_f$  is lower than the flame propagation velocity  $u_\infty$ . The flame front in the upper half of Figure 2.2 moves upstream and the initial perturbation is enhanced. In the lower half of Figure 2.2 the flame front is concave towards the fresh gas. Following the same argumentation as for the convex flame shape, the fresh gas velocity at the flame front is increased at the concave flame front and the initial perturbation is enhanced. The flame front is thus intrinsically unstable.

It can be shown that the growth rate of the Darrieus-Landau instability is high for small wavelengths of the initial perturbation [147]. For very small wavelengths, the flame can however not be regarded as a discontinuity anymore and flame propagation is dominated by thermal-diffusive effects [107, 147].

### 2.2.3 Thermal-diffusive Instabilities

Thermal-diffusive instabilities are described in detail by Williams [147]. When a flame front is initially perturbed as in Figure 2.3 (a), hot flame bulges convex to the unburnt gas act as a local sink for reactants. This means that reactants

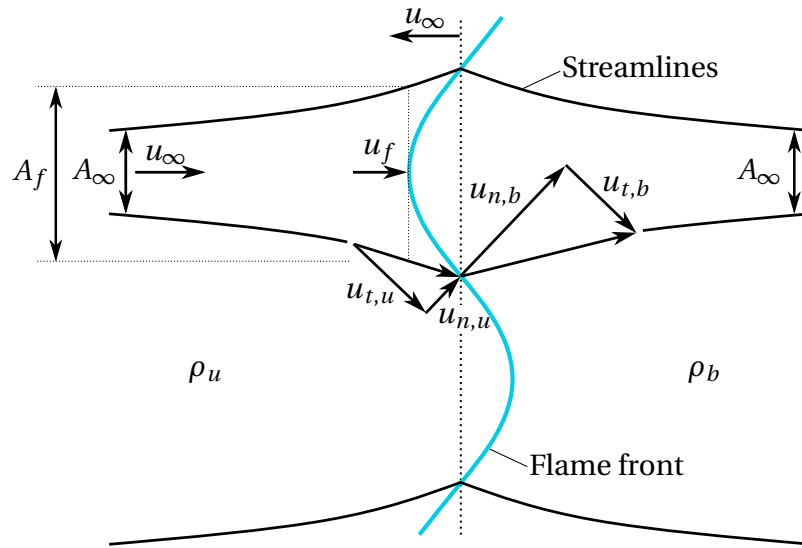


**Figure 2.2:** Darrieus-Landau instability [147].

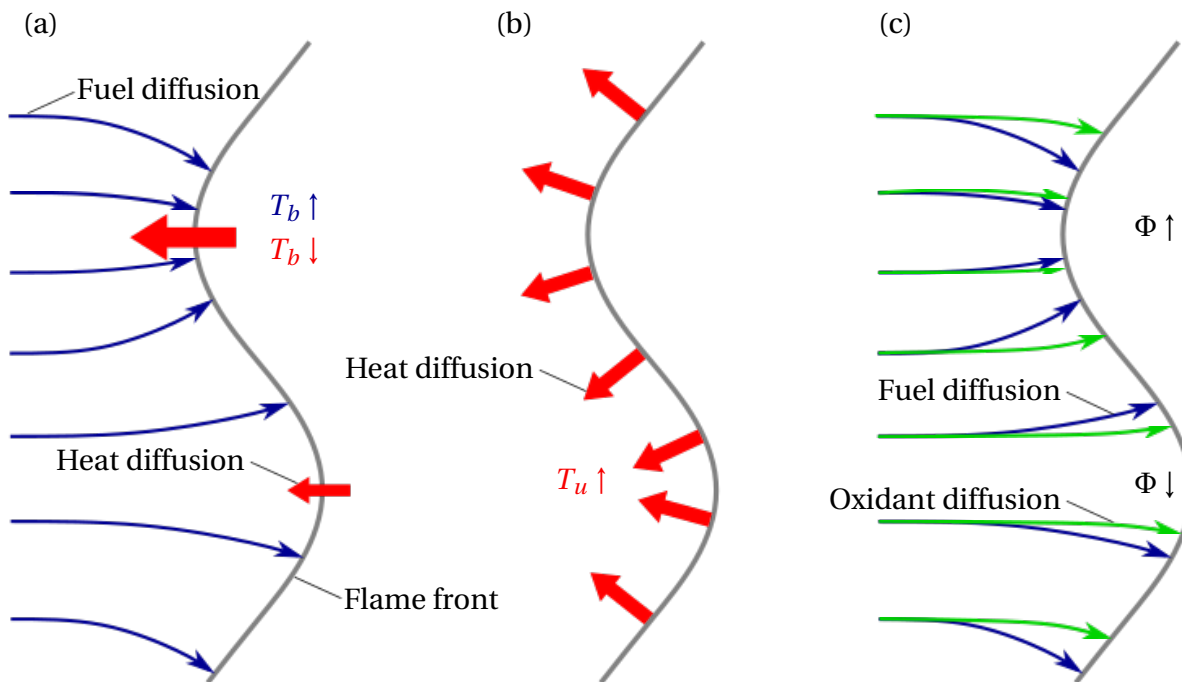


**Figure 2.3:** Thermal-diffusive instabilities. (a) non-equi Lewis number instability, (b) stabilizing effect of heat diffusion and (c) differential diffusion.

above and beneath the convex flame bulge diffuse towards the convex flame bulge. Reactant diffusion thus increases in convex flame bulges while it decreases in concave flame bulges. This increases the local flame temperature at convex flame bulges. A convex flame bulge however also acts as a local heat source. Heat flux away from a convex bulge increases when the flame temperature is increased due to enhanced reactant diffusion. Heat flux away from a convex flame bulge thus reduces the local flame temperature.

A mixture Lewis number  $Le$  can be defined in order to quantify the overall influence of species diffusion and thermal diffusion on flame propagation. The Lewis number  $Le_k$  of a species is defined as the ratio of the thermal diffusivity  $\alpha$  of the mixture to the species diffusivity  $D_k$  of species  $k$ .

$$Le_k = \frac{\alpha}{D_k} \quad (2.2)$$

The mixture Lewis number  $Le$  can be approximated by a combination of the Lewis numbers of all reactants. Bechtold and Matalon for example proposed calculating the mixture Lewis number as a mixture-dependent weighted average of the fuel and the oxidant [6]. If the mixture Lewis number is unity, the effects of reactant diffusion and heat diffusion on the flame temperature are balanced. The flame temperature and flame speed of a convex flame bulge increase if  $Le < 1$  while the flame speed of a concave flame bulge decrease. Initial perturbation are thus enhanced when  $Le < 1$ . This is the so called non-equi Lewis number instability. If  $Le > 1$ , the opposite effect is observed and the flame is stabilized by thermal-diffusive effects.

In addition to the combined effect of species diffusion and heat diffusion on the local flame temperature, heat diffusion alone has a stabilizing effect on the flame front. This is depicted in Figure 2.3 (b). At a flame bulge which is concave towards the fresh gas, preheating of the fresh gas increases due to the surrounding hot burnt gas. This increases the reaction rate and the flame speed at a concave flame bulge. Convex flame bulges however are surrounded by cold fresh gas. The preheat temperature and the local flame speed is therefore lower than at a concave flame bulge. This prevents instabilities at mixtures with a Lewis number of  $Le = 1$ . Non-equi Lewis number instabilities are thus only observed at Lewis numbers smaller than unity.

Another instability mechanism can be observed if the diffusivities  $D_k$  of the reactants differ significantly. This so called differential diffusion is depicted in Figure 2.3 (c). Reactants with higher diffusivities diffuse more strongly towards convex flame bulges than reactants with lower diffusivities. The equivalence ratio is increased at a convex flame bulge if the fuel is the stronger diffusing reactant compared to the oxidant. This leads to higher local flame speeds and flame temperatures at convex flame bulges and to lower local flame speeds and flame temperatures at concave flame bulges. The initial flame perturbation is enhanced by the diffusion processes and the flame front becomes unstable.

## 2.3 Cellular Flames in Lean Premixed Hydrogen Combustion

Hydrogen has a very high species diffusivity compared to the thermal diffusivity of hydrogen-air mixtures and compared to the species diffusivity of oxygen. According to Bechtold and Matalon [6] hydrogen-air mixtures have a thermal diffusivity of  $\alpha = 2.25 \times 10^{-4} \text{ m}^2 \text{ s}^{-1}$ , while hydrogen and oxygen have diffusivities of  $D_{H_2} = 7.29 \times 10^{-4} \text{ m}^2 \text{ s}^{-1}$  and  $D_{O_2} = 1.88 \times 10^{-4} \text{ m}^2 \text{ s}^{-1}$ , respectively. The mixture Lewis number of lean to stoichiometric hydrogen-air mixtures can be approximated by

$$\text{Le} = \frac{\alpha}{D} = 1 + \frac{(\text{Le}_{O_2} - 1) + (\text{Le}_{H_2} - 1) \xi}{1 + \xi}, \quad (2.3)$$

where  $D$  is the global mixture diffusivity,  $\xi$  is a mixture dependent weight function,

$$\xi = 1 + \text{Ze} \left( \frac{1}{\Phi} - 1 \right), \quad (2.4)$$

$\Phi$  is the equivalence ratio and  $\text{Ze}$  is the Zeldovich number [6]. When describing the combustion process with a global stoichiometric reaction [119]



the equivalence ratio is defined as the mass ratio of fuel  $F$  to oxidant  $O$  normalized by the stoichiometric fuel-oxidant ratio [94, 119].

$$\Phi = \frac{(Y_F/Y_O)}{(Y_F/Y_O)_{st}} = \frac{(Y_F/Y_O)}{(\nu'_F W_F) / (\nu'_O W_O)} \quad (2.6)$$

Here  $\nu'_F$ ,  $\nu'_O$ ,  $W_F$  and  $W_O$  are the forward stoichiometric coefficients and the molecular weights of the fuel and oxidant, respectively. The Zeldovich number is defined by the activation energy  $E$  of a global reaction, the adiabatic flame temperature  $T_{ad}$ , the unburnt gas temperature  $T_u$  and the universal gas constant  $R$ .

$$Ze = \frac{E(T_{ad} - T_u)}{R(T_{ad})^2} \quad (2.7)$$

Bechtold and Matalon used a constant activation energy of approximately  $E = 20 \text{ kcal/mol} = 8.368 \times 10^4 \text{ kJ kmol}^{-1}$  for hydrogen-air flames. For an equivalence ratio of  $\Phi = 0.33$  and an unburnt gas temperature of 293.15 K for example, the adiabatic flame temperature from Cantera equilibrium calculations [53] is 1257.22 K. This results in a mixture Lewis number of  $Le \approx 0.32$ . Thermal-diffusive instabilities are thus very likely to occur during the combustion of lean premixed hydrogen-air flames.

According to Markstein [107], Coward and Brinsley [21] were the first to observe that thermal-diffusive instabilities of lean premixed hydrogen-air flames may lead to a cellular flame structure with local extinction at concave zones towards the unburnt gas [55]. Grcar [55] identified this cellular flame structure as the third type of stable laminar flames besides planar flames and flame balls. Compared to planar laminar flames, the flame structure is significantly modified by thermal-diffusive instabilities. This leads to discrepancies between experimental results of laminar hydrogen-air flames and one-dimensional flame simulations. The laminar flame speed of lean hydrogen-air flames is for example significantly underestimated by numerical simulations [56]. The discrepancies between measured and predicted laminar flame speed can not be explained by uncertainties in the chemical kinetics but only by the difference in flame structure [148]. Differential diffusion also leads to lower flammability limits than in one-dimensional flames. Higher local equivalence ratios at convex flame bulges lead to higher flame temperatures than in one-dimensional flames [55, 56, 148]. When the flame temperature is increased above the crossover temperature, at which the chain branching reactions dominate the chain termination reactions, the otherwise non-ignitable laminar flame may be ignited [148].

Another physical phenomenon which is usually neglected in combustion

modelling is species diffusion due to temperature gradients, the so called Soret diffusion [119]. Even for hydrogen combustion, some authors assume the Soret effect to be negligible at ambient pressure and without preheating [17, 147, 151]. However, Grcar, Bell and Day [56] found that the Soret effect is important in lean premixed hydrogen-air combustion as it affects the formation of cellular structures. Higher diffusion velocities of hydrogen due to temperature gradients lead to even higher local equivalence ratios at convex bulges. This leads to altered flame dynamics and smaller cell structures. Grcar, Bell and Day observed an increase in local flame speed by 170% and an increase in global flame speed by 20% when including Soret diffusion in cellular flames at an equivalence ratio of 0.37. This contradicts the findings of Bongers and de Goey [11] and Ern and Giovangigli [40] who observed a reduction in flame speed of planar and conical flames due to the reduced diffusion velocity of radicals into the cold gas when including Soret diffusion [56].

At last, lean premixed hydrogen-air flames show a non-linear relation between flame stretch and the local flame speed. The flame speed of hydrogen-air flames can therefore not be approximated by a linear Markstein relation. This effect is aggravated by the Soret effect [56]. The Soret effect thus affects the flame structure and the response to flame stretch and has to be accounted for when modelling lean premixed hydrogen combustion. Heat diffusion due to species gradients, the so called Dufour effect, on the other hand can be neglected in premixed flames. The reactant and product species mass fraction gradients are opposed in premixed flames. Their effect on heat diffusion will therefore balance out [11, 56, 147].

## **2.4 Implications for Numerical Models of Boundary Layer Flashback**

Lean premixed hydrogen combustion is characterized by the occurrence of thermal-diffusive instabilities and by a cellular flame shape. The Soret effect, differential diffusion and non-equidiffusion have to be accounted for. Combustion in boundary layer flashback takes place in the direct presence of the wall. Heat loss to the wall leads to reduced near-wall flame velocities and to

flame quenching at higher heat loss rates. Heat loss will thus strongly influence the combustion process during boundary layer flashback and has to be accounted for in the numerical model as well.

In order to get a detailed insight into the flashback process, LES are applied. The large turbulent scales, the energy containing integral scales and the larger eddies of the inertial subrange of the turbulent kinetic energy spectrum in Figure 2.4 are resolved in LES. Small turbulent eddies of the inertial subrange and the viscous subrange have to be accounted for by a subgrid scale (SGS) model [119]. Large scale wrinkling of the flame front and the cellular flame structure of lean premixed hydrogen flames is resolved by resolving the larger turbulent motions. The computational effort is however still low compared to DNS, where all turbulent scales and the whole turbulent kinetic energy spectrum have to be resolved.

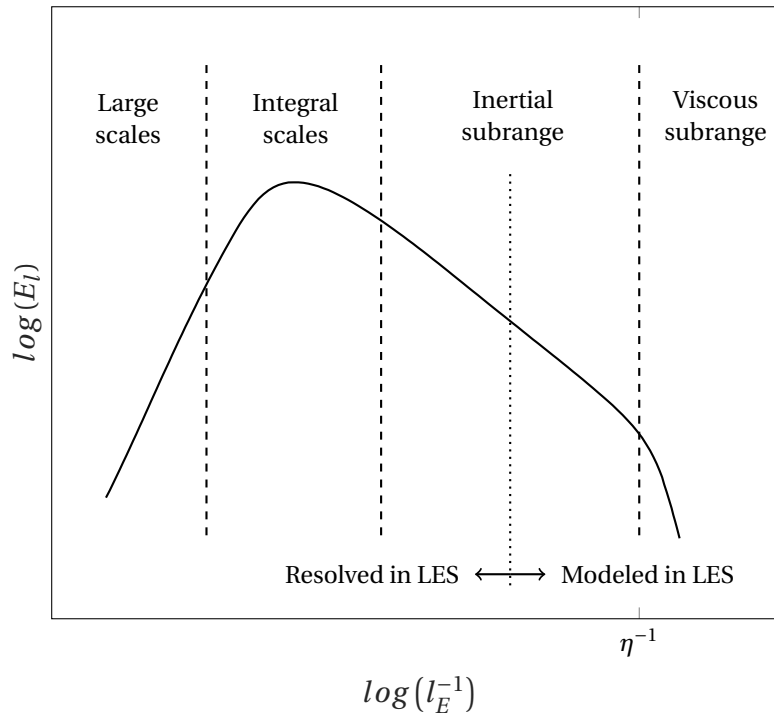


**Figure 2.4:** Spectrum of turbulent kinetic energy density  $E_l$  as a function of the inverse eddy size  $l_E$ . Adapted from Peters [117].

In LES, premixed combustion is commonly modelled by a transport equation for the reaction progress variable  $c$  with corresponding SGS models and

chemical source terms [33, 117]. Quenching effects can easily be accounted for in these combustion models [18]. Differential diffusion effects have also been included in the  $c$ -transport equation for simulations of hydrogen-methane flames without heat loss effects [25, 26]. The complex combination of flame quenching, differential diffusion, non-equidiffusion and Soret diffusion has however not yet been successfully simulated with the combustion models based on the reaction progress variable. The flashback velocity of hydrogen-methane flames has also not been successfully predicted with these combustion models. A different approach for modelling the combustion process is therefore chosen in the current study. The transport equations for the mass fraction of each involved chemical species are solved instead of solving only one transport equation for the reaction progress variable. The chemical source terms of the species are then obtained from the reaction rates of a detailed chemical reaction mechanism. This approach is much more computationally costly compared to the progress variable approach. However, it inherently accounts for heat loss effects and detailed diffusion processes can easily be modelled for each species individually. This approach will be presented in detail in the next chapter.



## 3 Numerical Model for Boundary Layer Flashback

The numerical investigation of boundary layer flashback is conducted with the open source computational fluid dynamics software OpenFOAM [145]. In order to accurately model hydrogen combustion, a new combustion solver is created on the basis of the standard OpenFOAM solver reactingFoam. The governing equations for the reactive and inert calculations are presented in the following.

### 3.1 Governing Equations for Reactive LES

The compressible Navier-Stokes equations are implemented in reactingFoam together with the continuity equation, the enthalpy equation and the species mass fraction transport equations. Favre filtered governing equations are solved in LES with non-constant density. A Favre filtered field  $\tilde{\phi}$  is obtained by applying the density weighted spatial filtering operation

$$\tilde{\phi} = \frac{\overline{\rho\phi}}{\bar{\rho}} \quad (3.1)$$

to an arbitrary field variable  $\phi$  [119]. Here, Favre filtered quantities are denoted by the tilde symbol and spatially filtered quantities are denoted by the bar symbol. Favre filtering leads to the decomposition of a field  $\phi$  into the filtered part  $\tilde{\phi}$  and the fluctuating part  $\phi'$  in the subgrid scales. No explicit filtering operation is applied to the field variables in OpenFOAM. Instead, the fields are only filtered implicitly by the spatial discretization of the computational domain and by the low-pass characteristics of the discrete differential operators [105]. The turbulence statistics of a turbulent channel has shown better grid convergence towards DNS results with implicit filtering than with explicit

filtering [105]. Implicit filtering can however lead to high numerical errors in the smallest turbulent scales [62, 105]. Furthermore, implicit filtering entails that the exact filter shape and filter width are unknown [62]. The filter width is for example relevant for the LES subgrid scale turbulence models. It therefore has to be estimated from grid size quantities. The filter width  $\Delta$  in the current simulations is assumed to be equal to the cube root of the local cell volume.

With the Boussinesq approximation for the SGS viscous stress tensor  $\tau_{ij,SGS}$  [119],

$$\tau_{ij,SGS} = -\bar{\rho} (\overline{u_i u_j} - \tilde{u}_i \tilde{u}_j) \approx \mu_{SGS} \left( \frac{\partial \tilde{u}_i}{\partial x_j} + \frac{\partial \tilde{u}_j}{\partial x_i} \right) - \frac{2}{3} \mu_{SGS} \frac{\partial \tilde{u}_k}{\partial x_k}, \quad (3.2)$$

Favre filtering of the compressible momentum equation and the neglect of gravitational forces leads to the filtered Navier-Stokes equations [51]

$$\begin{aligned} \frac{\partial (\bar{\rho} \tilde{u}_i)}{\partial t} + \frac{\partial (\bar{\rho} \tilde{u}_i \tilde{u}_j)}{\partial x_j} - \frac{\partial}{\partial x_j} \left( (\mu + \mu_{SGS}) \left( \frac{\partial \tilde{u}_i}{\partial x_j} + \frac{\partial \tilde{u}_j}{\partial x_i} \right) \right) \\ + \frac{\partial}{\partial x_j} \left( \frac{2}{3} (\mu + \mu_{SGS}) \frac{\partial \tilde{u}_k}{\partial x_k} \right) = -\frac{\partial \bar{p}}{\partial x_i}. \end{aligned} \quad (3.3)$$

Here,  $\tilde{u}_i$  is the filtered velocity component in the spatial direction  $x_i$  of the cartesian grid,  $t$  is the time and  $p$  is the pressure.  $\mu$  denotes the molecular dynamic viscosity and  $\mu_{SGS}$  is the SGS dynamic viscosity, which accounts for the SGS viscous stress. The SGS dynamic viscosity has to be modelled with an LES turbulence model. The Einstein sum convention is applied in all equations.

The gas composition is obtained by solving the Favre filtered transport equations for the mass fraction  $Y_k$  of each species  $k$  involved in the chemical reaction mechanism [51].

$$\frac{\partial (\bar{\rho} \tilde{Y}_k)}{\partial t} + \frac{\partial (\bar{\rho} \tilde{u}_i \tilde{Y}_k)}{\partial x_i} + \frac{\partial \bar{j}_{k,i}}{\partial x_i} - \frac{\partial}{\partial x_i} \left( \bar{\rho} \frac{\nu_{SGS}}{Sc_{SGS}} \frac{\partial \tilde{Y}_k}{\partial x_i} \right) = \bar{\dot{\omega}}_k \quad (3.4)$$

The last term on the left hand side of equation (3.4) results from the gradient assumption for the filtered turbulent scalar flux,

$$\overline{u_i Y_k} - \tilde{u}_i \tilde{Y}_k = -D_{SGS} \frac{\partial \tilde{Y}_k}{\partial x_i} = -\frac{\nu_{SGS}}{Sc_{SGS}} \frac{\partial \tilde{Y}_k}{\partial x_i}, \quad (3.5)$$

where  $D_{SGS}$  is the SGS diffusivity. The SGS diffusivity is in turn modeled by the SGS kinematic viscosity  $\nu_{SGS} = \mu_{SGS}/\bar{\rho}$  and the SGS Schmidt number  $Sc_{SGS} = \nu_{SGS}/D_{SGS}$  [119]. The formulation of the filtered diffusion mass flux  $\overline{j_{k,i}}$  is presented in Section 3.6. The filtered chemical reaction rate  $\overline{\dot{\omega}_k}$  needs additional closure. This is covered in Section 3.5.

With the mixture averaged isobaric specific heat capacity  $c_p$ , the filtered gas temperature  $\tilde{T}$  is obtained from the specific sensible enthalpy  $\tilde{h}_s$ ,

$$\tilde{h}_s = \int_{T_0}^{\tilde{T}} c_p dT, \quad (3.6)$$

of the gas mixture [119]. The transport equation for the Favre filtered sensible enthalpy  $h_s$ ,

$$\frac{\partial \bar{\rho} \tilde{h}_s}{\partial t} + \frac{\partial \bar{\rho} \tilde{u}_i \tilde{h}_s}{\partial x_i} - \frac{\partial}{\partial x_i} \left( \left( \frac{\lambda}{c_p} + \frac{\mu_{SGS}}{Pr_{SGS}} \right) \frac{\partial \tilde{h}_s}{\partial x_i} \right) = \frac{\partial \bar{p}}{\partial t} - \frac{\partial \bar{\rho} \tilde{k}}{\partial t} - \frac{\partial \bar{\rho} \tilde{u}_i \tilde{k}}{\partial x_i} - h_{f,k}^0 \overline{\dot{\omega}_k}, \quad (3.7)$$

therefore has to be solved [119]. Here,  $k = 0.5 u_i u_i$  and  $\tilde{k} = 0.5 \tilde{u}_i \tilde{u}_i$  are the total kinetic energy and the filtered total kinetic energy, respectively. The last term on the left hand side of equation (3.7) comprises the energy flux  $\overline{q_i}$ , which is approximated by the gradient of the sensible enthalpy [51],

$$\overline{q_i} = -\lambda \frac{\partial \overline{T}}{\partial x_i} \approx -\frac{\lambda}{c_p} \frac{\partial \tilde{h}_s}{\partial x_i}, \quad (3.8)$$

and the filtered subgrid scalar fluxes approximated by the gradient assumption

$$\bar{\rho} \left( \overline{u_i h_s} - \tilde{u}_i \tilde{h}_s \right) \approx -\frac{\mu_{SGS}}{Pr_{SGS}} \frac{\partial \tilde{h}_s}{\partial x_i} \quad (3.9)$$

and the SGS Prandtl number  $Pr_{SGS} = \nu_{SGS}/\alpha_{SGS}$ . The thermal conductivity  $\lambda$  is defined by

$$\lambda = \frac{\alpha}{\rho c_p}. \quad (3.10)$$

The Dufour effect, viscous heat, gravity and the unresolved kinetic energy flux  $\bar{\rho} \left( \overline{u_i k} - \tilde{u}_i \tilde{k} \right)$  are neglected in equation (3.7) [145]. The last term on the right hand side is heat release due to combustion. The heat release rate is the sum

of all filtered reaction rates of all species  $k$  multiplied by the specific enthalpy of formation  $h_{f,k}^0$  at the reference temperature  $T_0$ .

Inserting the discretized Navier-Stokes equations (3.3) into the discretized continuity equation [51]

$$\frac{\partial \bar{\rho}}{\partial t} + \frac{\partial (\bar{\rho} \tilde{u}_i)}{\partial x_i} = 0 \quad (3.11)$$

leads to a pressure correction equation which takes the pressure-velocity coupling into account [76]. The pressure correction equation and the species mass fraction transport equations (3.4) are solved together with the enthalpy equation (3.7) in a segregated manner by applying the merged PISO-SIMPLE (PIMPLE) algorithm [41, 64, 73, 76, 145]. The gas mixture is assumed to behave like a perfect gas, for which the state equation

$$\bar{\rho} = \frac{W \bar{p}}{R \tilde{T}} \quad (3.12)$$

holds. Here,  $W$  is the mixture averaged molar mass, which is calculated from the molar mass  $W_s$  of all  $N_s$  species and the species mass fractions [119].

$$\frac{1}{W} = \sum_{s=1}^{N_s} \frac{\tilde{Y}_s}{W_s} \quad (3.13)$$

### 3.2 Low Mach Number Approximation for Reactive LES

The previously described compressible governing equations (3.3), (3.4) and (3.7) can be simplified for flows at low Mach numbers. Pressure oscillations generated by the turbulent flow decrease significantly at low fluid velocities [120]. Pressure oscillations thus only have a limited effect on the thermodynamic properties of a gas at low velocities. This motivates the decoupling of a thermodynamic pressure variable  $p_0$  from the fluid dynamic pressure  $p_d$ . The thermodynamic pressure is used for thermodynamic gas properties and in the equation of state. The fluid dynamic pressure on the other hand is linked to the velocity field.

The Navier-Stokes equations (3.3) and the pressure correction equation are solved for the fluid dynamic pressure  $p_d$ . The thermodynamic pressure  $p_0$  is

assumed to be constant [32, 121]. This implies that density is a sole function of temperature and gas composition,

$$\bar{\rho} = \frac{W p_0}{R \bar{T}}, \quad (3.14)$$

which prevents acoustic oscillations. This approach is similar to the approach of Duwig et al. [32] in their OpenFOAM combustion solver reactingLMFoam.

When introducing a constant thermodynamic pressure for all thermodynamic properties, the time derivative of pressure in the enthalpy transport equation (3.7) is zero. The kinetic energy in the enthalpy transport equation can also be neglected at low Mach numbers. As the kinetic energy at low gas velocities is low compared to the thermal energy, changes in kinetic energy only have a limited influence on the gas temperature [32, 120]. This results in the transport equation for sensible energy,

$$\frac{\partial \bar{\rho} \widetilde{h}_s}{\partial t} + \frac{\partial \bar{\rho} \widetilde{u}_i \widetilde{h}_s}{\partial x_i} - \frac{\partial}{\partial x_i} \left( \left( \frac{\lambda}{c_p} + \frac{\mu_{SGS}}{\text{Pr}_{SGS}} \right) \frac{\partial \widetilde{h}_s}{\partial x_i} \right) = -h_{f,k}^0 \overline{\dot{\omega}_k}, \quad (3.15)$$

for flows at low Mach numbers.

### 3.3 Governing Equations for Inert LES

Accurate modelling of the inert base flow is decisive for obtaining reliable results from the combustion simulations. The inert channel flow is therefore first simulated with the incompressible OpenFOAM solver pimpleFoam. Assuming a constant density  $\bar{\rho}$  for incompressible flows leads to the incompressible continuity equation

$$\frac{\partial \widetilde{u}_i}{\partial x_i} = 0 \quad (3.16)$$

and the incompressible Navier-Stokes equations

$$\frac{\partial \widetilde{u}_i}{\partial t} + \frac{\partial (\widetilde{u}_i \widetilde{u}_j)}{\partial x_j} - \frac{\partial}{\partial x_j} \left( (\nu + \nu_{SGS}) \left( \frac{\partial \widetilde{u}_i}{\partial x_j} + \frac{\partial \widetilde{u}_j}{\partial x_i} \right) \right) = -\frac{1}{\bar{\rho}} \frac{\partial \bar{p}}{\partial x_i}. \quad (3.17)$$

Here, the kinematic viscosity  $\nu$  is the dynamic viscosity  $\mu$  divided by the filtered density,  $\nu = \mu/\bar{\rho}$ . The incompressible continuity and Navier-Stokes

equations are solved in `pimpleFoam` in a segregated manner by applying the PIMPLE solution algorithm [76].

### 3.4 LES Turbulence Models

In the presented governing equations, the SGS viscosity  $\nu_{SGS}$  was introduced in order to model the influence of the SGS viscous stress on the filtered velocity field. This artificial viscosity can be modeled with various LES turbulence models. The Smagorinsky model, the dynamic one-equation model and implicit turbulence modelling are used in the present work.

#### 3.4.1 The Smagorinsky Turbulence Model

The first SGS Model for LES was proposed by Smagorinsky [130] for meteorological simulations. The Smagorinsky model was derived for incompressible fluids by assuming an equilibrium of the mean turbulent kinetic energy production  $\langle P \rangle$  and dissipation  $\epsilon$ . This assumption is valid in the inertial subrange of the turbulent energy spectrum of high Reynolds number flows. The cells of the computational mesh thus have to be small enough to lie within this range of the spectrum. The following deduction of the Smagorinsky model is based on the descriptions by Lilly [103] and Pope [122].

The SGS turbulent kinetic energy production  $P$  is given by

$$P_{inc} = -\tau_{ij,SGS,inc} \widetilde{S}_{ij}, \quad (3.18)$$

where  $\tau_{ij,SGS,inc} = \tau_{ij,SGS} / \bar{\rho}$  is the incompressible viscous stress tensor and

$$\widetilde{S}_{ij} = \frac{1}{2} \left( \frac{\partial \widetilde{u}_i}{\partial x_j} + \frac{\partial \widetilde{u}_j}{\partial x_i} \right) \quad (3.19)$$

is the filtered strain rate tensor. The incompressible dissipation rate  $\epsilon_{inc}$  deduced from the Kolmogorov spectrum is dependent on the mean square of the filtered strain rate,  $\widetilde{S} = \sqrt{2\widetilde{S}_{ij}\widetilde{S}_{ij}}$ , the filter width  $\Delta$ , the Kolmogorov constant  $c_K = 1.5$  and the filter dependent constant  $a_f$ :

$$\epsilon_{inc} = \langle \widetilde{S}^2 \rangle^{\frac{3}{2}} (a_f c_K)^{\frac{-3}{2}} \Delta^2. \quad (3.20)$$

When applying the Boussinesq approximation for incompressible fluids

$$\tau_{ij,SGS,inc} = -2\nu_{SGS}\widetilde{S}_{ij} \quad (3.21)$$

and the mixing length hypothesis

$$\nu_{SGS} = l_S^2 \widetilde{S} \quad (3.22)$$

with the Smagorinsky length scale  $l_S$ , the equilibrium of the mean turbulent kinetic energy production and dissipation is given by

$$\epsilon_{inc} = \langle P_{inc} \rangle = l_S^2 \langle \widetilde{S}^3 \rangle. \quad (3.23)$$

With equation (3.20) and the approximation  $\langle \widetilde{S}^2 \rangle^{\frac{3}{2}} \approx \langle \widetilde{S}^3 \rangle$ , this results in the Smagorinsky length scale

$$l_S = (a_f c)^{\frac{-3}{4}} \Delta. \quad (3.24)$$

Racasting the constant Factor  $(a_f c_K)^{\frac{-3}{4}}$  as the Smagorinsky constant  $c_S$  gives the equation for the turbulent viscosity in the Smagorinsky model,

$$\nu_{SGS} = (c_S \Delta)^2 \widetilde{S}. \quad (3.25)$$

When assuming a sharp spectral filter, the filter dependent constant is approximately  $a_f \approx 6.9$ . This results in the Smagorinsky constant of  $c_S = 0.17$  proposed by Lilly [103]. Depending on the application, the Smagorinsky constant however varies between 0.01 and 0.3 in order to obtain good simulation results [117].

### 3.4.2 The Smagorinsky Turbulence Model in OpenFOAM

In OpenFOAM, the Smagorinsky model is implemented in a different manner [145]. The SGS turbulent viscosity  $\nu_{SGS}$  is obtained from the SGS turbulent kinetic energy  $k_{SGS} = \frac{1}{2} \widetilde{u_i u_i} - \frac{1}{2} \widetilde{u_i} \widetilde{u_i}$ , the model constant  $c_k$  and the LES filter-width  $\Delta$ .

$$\nu_{SGS} = c_k \sqrt{k_{SGS}} \Delta \quad (3.26)$$

This is the common approach for one-equation models with a transport equation for the SGS turbulent kinetic energy [27, 49, 111]. The dissipation rate

is furthermore not obtained from the Kolmogorov spectrum. A dimensional analysis instead results in the dissipation rate

$$\epsilon = c_e \bar{\rho} (k_{SGS})^{\frac{3}{2}} \Delta^{-1} \quad (3.27)$$

as a function of the SGS turbulent kinetic energy, where  $c_e$  is a model constant. When assuming that the normal SGS viscous stress is isotropic and that the deviatoric part of the SGS viscous stress is aligned with the deviatoric strain rate tensor  $(\widetilde{S}_{ij})_{dev}$  [49], the Boussinesq approximation of the SGS viscous stress tensor (3.2) can be reformulated to

$$\tau_{ij,SGS} = \frac{2}{3} \bar{\rho} \delta_{ij} k_{SGS} - 2 \bar{\rho} \nu_{SGS} (\widetilde{S}_{ij})_{dev}. \quad (3.28)$$

It is again assumed that a local equilibrium prevails between the SGS turbulent kinetic energy production  $P$ ,

$$P = -\tau_{ij,SGS} \widetilde{S}_{ij} = -\frac{2}{3} \bar{\rho} \delta_{ij} k_{SGS} \widetilde{S}_{ij} + 2 \bar{\rho} c_k \sqrt{k_{SGS}} \Delta (\widetilde{S}_{ij})_{dev} \widetilde{S}_{ij}, \quad (3.29)$$

and the dissipation  $\epsilon$ . This leads to the following equation for the SGS turbulent kinetic energy:

$$k_{SGS} = \left( \frac{-\frac{2}{3} \delta_{ij} \widetilde{S}_{ij} + \sqrt{\left(\frac{2}{3} \delta_{ij} \widetilde{S}_{ij}\right)^2 + 8 c_e c_k (\widetilde{S}_{ij})_{dev} \widetilde{S}_{ij}}}{2 c_e \Delta^{-1}} \right)^2. \quad (3.30)$$

In the case of incompressible flows, the trace of the strain rate tensor vanishes according to equation (3.16). The SGS turbulent kinetic energy equation (3.30) can thereby be simplified to

$$k_{SGS} = \frac{c_k}{c_e} \Delta^2 \widetilde{S}^2 \quad (3.31)$$

and the SGS turbulent viscosity is given by

$$\nu_{SGS} = c_k \sqrt{\frac{c_k}{c_e}} \Delta^2 \widetilde{S}. \quad (3.32)$$

By comparing this equation for the SGS turbulent viscosity with equation (3.25), it becomes apparent that the standard incompressible Smagorinsky

model can be recovered from the OpenFOAM formulation [114], when

$$c_S = \sqrt{c_k \sqrt{\frac{c_k}{c_\epsilon}}}. \quad (3.33)$$

The Smagorinsky model is only valid in the inertial subrange of high Reynolds number flows. Low Reynolds number effects and turbulence anisotropies however occur near walls. Van Driest damping is applied in order to use the Smagorinsky model also in near-wall regions. The filter width is then defined as the cube root of the cell volume multiplied by the van Driest damping function [109, 141, 145]

$$f(y) = \frac{\kappa}{C_\Delta} \left(1 - e^{-y^+/A^+} y\right). \quad (3.34)$$

This also ensures that the SGS turbulent viscosity vanishes directly at the wall. Here,  $y^+$  is the non-dimensional wall distance and  $\kappa = 0.41$  is the von Karman constant. The constants  $C_\Delta$  and  $A^+$  are model constants. The wall-normal distance  $y$  is non-dimensionalized by the kinematic viscosity  $\nu$ , the SGS turbulent viscosity  $\nu_{SGS}$  and the wall-normal velocity gradient  $\left.\frac{\partial \bar{u}}{\partial y}\right|_w$  at the wall [122, 145].

$$y^+ = y \frac{(\nu + \nu_{SGS})^{0.5}}{\nu} \left(\left.\frac{\partial \bar{u}}{\partial y}\right|_w\right)^{0.5} \quad (3.35)$$

The SGS turbulent viscosity can be neglected in Equation (3.35) as it vanishes at walls when applying van Driest damping.

### 3.4.3 The Dynamic One-Equation Model

One drawback of the Smagorinsky turbulence model is the assumption of local equilibrium between turbulent kinetic energy production and dissipation. Non-local and history effects of turbulence are thereby neglected [88, 122]. Models where a transport equation is solved [27] for the SGS turbulent kinetic energy avoid this issue [88, 122]. However, the problem prevails that the fixed model constants are only valid for one flow regime. Kim and Menon [88] therefore developed a one-equation model with dynamic model constants on the

basis of the dynamic procedure of Germano et al. [52] and the transport equation for the SGS turbulent kinetic energy [150],

$$\frac{\partial k_{SGS}}{\partial t} + \tilde{u}_i \frac{\partial k_{SGS}}{\partial x_i} = -\tau_{ij} \frac{\partial \tilde{u}_i}{\partial x_j} - \epsilon + \frac{\partial}{\partial x_i} \left( \nu_{SGS} \frac{\partial k_{SGS}}{\partial x_i} \right). \quad (3.36)$$

In the inertial subrange of high Reynolds turbulence it can be assumed that the statistical structure of small resolved scales is identical to the statistical structure of large unresolved scales [125]. The turbulence model constants are then independent of the filter width [122]. This fact can be exploited for locally determining the model constants. A relation between the sub test filter (STF) stress tensors and dissipation rates at test filter level can be obtained by explicitly filtering the implicitly filtered velocity field with a test filter. A new STF stress tensor [88]

$$\tau_{ij,STF} = \widehat{\tilde{u}_i \tilde{u}_j} - \widehat{\tilde{u}_i} \widehat{\tilde{u}_j} \quad (3.37)$$

and a new STF dissipation rate [88, 122, 145]

$$\epsilon_{STF} = \frac{1}{2} \nu \left( \widehat{\tilde{S}_{ij} \tilde{S}_{ij}} - \widehat{\tilde{u}_i} \widehat{\tilde{u}_i} \right) \quad (3.38)$$

at test filter level are therefore defined for incompressible flows. Test filtered fields are denoted by the hat symbol. The STF stress tensor can be modelled in the same manner as the SGS viscous stress tensor (3.28) at grid scale level,

$$\tau_{ij,STF} = \frac{2}{3} \delta_{ij} k_{STF} - 2\nu_{STF} \left( \widehat{\tilde{S}_{ij}} \right)_{dev}. \quad (3.39)$$

In accordance with Equation (3.26), the STF viscosity  $\nu_{STF}$  can be approximated by the model constant  $c_k$ , the STF turbulent kinetic energy  $k_{STF} = \frac{1}{2} \widehat{\tilde{u}_i \tilde{u}_i} - \frac{1}{2} \widehat{\tilde{u}_i} \widehat{\tilde{u}_i}$  and the test filter width  $\widehat{\Delta}$  [88]:

$$\nu_{STF} = c_k \sqrt{k_{STF}} \widehat{\Delta}. \quad (3.40)$$

The STF dissipation rate can be modelled as

$$\epsilon_{STF} = c_\epsilon (k_{STF})^{\frac{3}{2}} \widehat{\Delta}^{-1}, \quad (3.41)$$

which is similar to Equation (3.27).

Combining Equations (3.37) to (3.41) allows for the calculation of the model constants from the test filtered velocity field,

$$c_k = \frac{1}{2} \frac{\widehat{\tilde{u}_i \tilde{u}_j} - \widehat{\tilde{u}_i} \widehat{\tilde{u}_j} - \frac{2}{3} \delta_{ij} k_{STF}}{-2 \sqrt{k_{STF}} \left( \widehat{S_{ij}} \right)_{dev} \widehat{\Delta}} \quad (3.42)$$

and

$$c_e = \frac{\frac{1}{2} \nu \left( \widehat{S_{ij} S_{ij}} - \widehat{S_{ij}} \widehat{S_{ij}} \right)}{\left( k_{STF} \right)^{\frac{3}{2}} \widehat{\Delta}^{-1}}. \quad (3.43)$$

These dynamic model constants allow for modelling the SGS turbulent kinetic viscosity and dissipation rate in the transport equation (3.36) of  $k_{SGS}$  in a similar manner to the Smagorinsky turbulence model in Equations (3.26) and (3.27).

In OpenFOAM, the velocity field is test filtered by a top-hat filter with a larger filter width than the filter width of the implicit LES filter. The implementation of the dynamic model in OpenFOAM however slightly differs from the previously derived equations. In the implementation of the dynamic model constants calculation (3.42) and (3.43), the filter width  $\widehat{\Delta}$  is inconsistently set to the grid filter width  $\Delta$ . Furthermore, the kinematic viscosity  $\nu$  in Equation (3.43) is replaced by the effective viscosity  $(\nu + \nu_{SGS})$  from the previous timestep and the calculated values of  $c_k$  and  $c_e$  are limited to positive values [145].

#### 3.4.4 Implicit Turbulence Modelling

A completely different approach to accounting for the influence of SGS turbulent velocity fluctuations in the governing equations is to omit the explicit turbulence model. The truncation error of the applied discretization schemes, often referred to as numerical diffusion, can be exploited as a SGS turbulence model instead. This approach is called implicit turbulence modelling [67].

The choice of numerical discretization schemes is crucial for the quality of the predicted velocity fields when using implicit turbulence modelling. Excessive numerical damping introduced by the schemes for example can cause a high

Reynolds turbulent flow to exhibit a low Reynolds behaviour [50]. Appropriate discretization schemes therefore have to be selected.

Channel flow will be simulated at different Reynolds numbers in the present work. As the Smagorinsky turbulence model has been developed for high Reynolds number flows, this model might fail at low Reynolds numbers. The implicit turbulence model might be an alternative to the much more costly dynamic one-equation model when simulating low Reynolds number flows. This approach is particularly interesting in reactive simulations, where the strong heat release can interfere with the performance of explicit turbulence models which were developed for isothermal flows [125]. The implicit turbulence model with standard discretization schemes is therefore applied in the current work in simulations at very low Reynolds numbers.

### 3.5 Turbulent Combustion Modelling

The filtered chemical reaction rate  $\overline{\dot{\omega}}_k$  is still an unclosed term in the filtered transport equations (3.4) and (3.7) for species mass fractions and sensible enthalpy. Following Kee et al. [83], a reaction  $r$  can generally be described in the following form by the forward and backward stoichiometric coefficients  $v'_{k,r}$  and  $v''_{k,r}$  of all  $N_s$  species involved in the reaction mechanism.



Here,  $\Xi_s$  is the chemical symbol of species  $s$ . The reaction rate of species  $k$  is given by the difference of forward and backward reaction rate of all  $N_r$  reactions,

$$\dot{\omega}_k = W_k \sum_{r=1}^{N_r} \left( (v'_{k,r} - v''_{k,r}) \left( k_r^f \prod_{s=1}^{N_s} \left( \frac{\rho Y_s}{W_s} \right)^{v'_{s,r}} - k_r^b \prod_{s=1}^{N_s} \left( \frac{\rho Y_s}{W_s} \right)^{v''_{s,r}} \right) \left( \sum_{s=1}^{N_s} \gamma_{s,r} \frac{\rho Y_s}{W_s} \right) \right). \quad (3.45)$$

$k_r^f$  and  $k_r^b$  are the forward and backward reaction rate constants of reaction  $r$ ,  $\gamma_{s,r}$  is the third body efficiency of species  $s$  in reaction  $r$  and  $W_s$  is the molar

mass of species  $s$ . The forward rate constant is assumed to have an Arrhenius temperature dependence,

$$k_r^f = A_r T^{\beta_r} \exp \frac{-E_r}{RT}, \quad (3.46)$$

with the pre-exponential factor  $A_r$ , the temperature exponent  $\beta_r$  and the activation energy  $E_r$ . The backward reaction rate constant  $k_r^b$  can be obtained from the equilibrium constant

$$K_r = \frac{k_r^f}{k_r^b} \quad (3.47)$$

of the reaction [83, 145]. The Arrhenius coefficients for the forward reaction rate constants are specified in detailed chemical reaction mechanisms. In the present work, the hydrogen-air reaction mechanism with 9 species and 23 reactions developed by Burke et al. [15] is applied. This mechanism improves the detailed mechanism of Li et al. [98] by accounting for newer experimental data at high pressure and with dilution [15].

It can be seen from Equations (3.45) and (3.46) that the chemical reaction rate is generally a function of temperature and local gas composition  $Y$ . The reaction rates of some reactions are also pressure dependent. This has to be accounted for in the Arrhenius approach (3.46) for example by blending a high-pressure and a low-pressure Arrhenius rate constant with the nonlinear Troe blending function [83]. The rate constants are highly non-linear. The influence of the SGS turbulent fluctuations of temperature, species mass fractions and pressure on the filtered chemical reaction rates therefore can not be neglected. The filtered reaction rate  $\dot{\omega}_k(T, Y, p)$  is thus generally not equal to the reaction rate calculated from the filtered quantities,  $\dot{\omega}_k(\tilde{T}, \tilde{Y}, \bar{p})$ . Several different approaches for accounting for the influence of the SGS fluctuations on the filtered source term have been developed. Some models only take account of the limiting influence of insufficient micro-mixing on the reaction rate (partially stirred reactor [48]) or artificially modify the flame structure in order to allow for flame resolution on coarse grids (thickened flame model [19, 48, 96]). Other models take account of the SGS fluctuation influence with a probability density function [12, 48, 51, 77, 78, 113]. A different promising approach, which was recently applied to the study of differential diffusion effects with LES, is the linear eddy model [99].

All previously mentioned combustion models require additional modelling and thereby induce additional uncertainties. The combustion model applied in the current work avoids this disadvantage by neglecting the turbulence-chemistry interaction in the subgrid scales, thus assuming

$$\overline{\dot{\omega}_k(T, Y, p)} = \dot{\omega}_k(\tilde{T}, \tilde{Y}, \bar{p}). \quad (3.48)$$

This combustion model is referred to as the quasi-laminar combustion model or as the implicit LES combustion model.

The assumption (3.48) is fulfilled either when the mixing time scale of the SGS velocity fluctuations is much smaller than the time scale of the chemical reactions [32] or when the flame structure inside the filter width is quasi laminar. Pitsch and Duchamp de Lageneste [118] developed a SGS combustion regime diagram on the basis of Peters' regime diagram for turbulent combustion [116]. The SGS regime diagram allows to evaluate the character of the SGS flame structure. The characteristic dimensionless parameters are therefore based on SGS quantities. The Karlovitz number  $Ka$  relates the laminar flame time scale  $t_f$  to the time scale of the Kolmogorov eddies  $t_\eta$ . The laminar flame time scale is in turn calculated from the laminar flame length scale  $l_f = D/s_{l,0}$ , the laminar flame speed  $s_{l,0}$  and the global mixture diffusion coefficient  $D$  [116]. The global mixture diffusion coefficient can be estimated from the mixture Lewis number according to Equation (2.3) and the mixture thermal diffusivity  $\alpha$ . The Kolmogorov time scale is defined by the Kolmogorov length scale  $\eta = (v^3/\epsilon_{inc})^{0.25}$  and the molecular viscosity.

$$Ka = \frac{t_f}{t_\eta} = \frac{l_f^2/D}{\eta^2/\nu} = \frac{\left(\frac{D}{s_{l,0}}\right)^2/D}{\left(\frac{v^3}{\epsilon_{inc}}\right)^{\frac{1}{2}}/\nu} \quad (3.49)$$

The Karlovitz number is thus independent of the LES filter width. The Karlovitz number can be reformulated in terms of LES quantities,

$$Ka = \sqrt{\frac{c_\epsilon k_{SGS}^{\frac{3}{2}} D^2}{\Delta s_{l,0}^4 \nu}}, \quad (3.50)$$

when the incompressible scalar dissipation rate  $\epsilon_{inc} = \epsilon/\rho$  is calculated as in Equation (3.27) from the SGS velocity and the filter width.

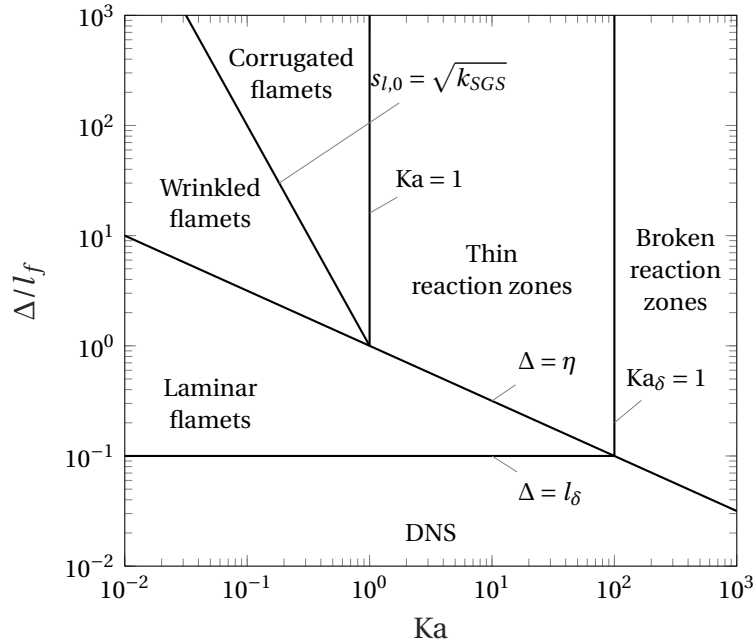


**Figure 3.1:** Combustion regime diagram for LES [118].

The LES combustion regimes depend on the Karlovitz number and the ratio of the filter width  $\Delta$  to the laminar flame length scale  $l_f$ . The regimes are shown in Figure 3.1 for  $c_c = 1$  and  $D = \nu$ . In the DNS regime, the filter width is smaller than the Kolmogorov length scale and the reaction zone thickness or inner flame length scale  $l_\delta \approx 0.1l_f$  is resolved by the filter width. When the Kolmogorov length scales are fully resolved but the filter width is larger than the inner flame length scale, the SGS flame is in the laminar flamelet regime. As there is no unresolved turbulence below the filter width, the SGS flame structure remains laminar and no SGS combustion model is needed. When the filter width is further increased above the Kolmogorov length scale, the LES regime depends on the Karlovitz number. The Kolmogorov eddies are able to penetrate and perturb the reaction zone when the Karlovitz number  $Ka_\delta$  formed by the inner flame length scale  $l_\delta$  is larger than 1 ( $Ka > 100$ ). This can cause local extinction due to enhanced heat loss to the preheat zone [117]. This regime is the broken reaction zones regime. When the regular Karlovitz number  $Ka$  is larger than 1 but  $Ka_\delta < 1$ , the SGS turbulent eddies are small enough to penetrate the flame preheat zone given by  $l_f$  but not the reaction zone given by  $l_\delta$ . This leads to enhanced scalar mixing in the preheat zone

[117] in the thin reaction zones regime. The flame is corrugated by the smallest turbulent eddies when the Kolmogorov eddies are larger than the flame length scale. The resolved and the unresolved part of the flame is corrugated if in this case the SGS turbulent velocity fluctuation  $\sqrt{k_{SGS}}$  is larger than the laminar flame speed. This is the corrugated flamelet regime. If the SGS turbulent velocity fluctuation is however smaller than the laminar flame speed, the unresolved part of the flame will be dominated by laminar flame propagation and the unresolved flame structure will approximately remain laminar. The length scale defined by the equality of laminar flame speed and SGS velocity fluctuation is the Gibson length scale.

For Figure 3.1, it was assumed that  $D = \nu$  and  $c_e = 1$ . Inserting these assumptions and the condition for the Gibson length scale,  $s_{l,0} = \sqrt{k_{SGS}}$ , into Equation (3.50) leads to a constant relation between the Karlovitz number and  $\Delta/l_f$ ,

$$\frac{\Delta}{l_f} = \text{Ka}^{-2}. \quad (3.51)$$

For hydrogen however, the species diffusivity is usually not equal to the viscosity. The first assumption is therefore not valid for hydrogen combustion. The condition for the Gibson length scale and  $D \neq \nu$  leads to the relation

$$\frac{\Delta}{l_f} = \text{Ka}^{-2} \frac{D}{\nu}. \quad (3.52)$$

As  $D/\nu$  varies depending on mixture, pressure and temperature, the separation between the wrinkled flamelet and the corrugated flamelet regime in the combustion regime diagram is also mixture, pressure and temperature dependent.

From the analysis of SGS combustion regimes by Pitsch and Duchamp de Lageneste [118] it can be concluded that the unresolved part of the flame will retain its laminar character in the wrinkled flamelet, the laminar flamelet and the DNS regimes. The assumption (3.48) that a SGS combustion model is unnecessary is approximately fulfilled in these regimes. The filter width thus has to be small enough so that either the Kolmogorov eddies are fully resolved, or that the SGS velocity fluctuations are negligible compared to the laminar flame speed.

## 3.6 Transport Properties

A detailed species diffusion and thermal diffusion model is essential in order to accurately model hydrogen combustion with all relevant combustion instability mechanisms. The implemented detailed species diffusion model based on kinetic gas theory and empirical correlations are presented in the following. Furthermore, the calculation of the thermal conductivity and the molecular viscosity is described.

### 3.6.1 Species Diffusion Model

On the basis of the kinetic theory of gases, Dixon-Lewis [28] developed equations for the calculation of multicomponent species diffusivities, Soret diffusivities and thermal diffusivities from the collision integrals of species pairs. As the calculation of the multicomponent diffusion fluxes is computationally expensive [51], the multicomponent system is usually approximated by the following mixture averaged approach based on Fick's empirical diffusion model [42].

The filtered diffusion mass flux  $\overline{j_{k,i}}$  of species  $k$  introduced in the transport equations for the species mass fractions (3.4) consists of the diffusion mass flux  $\overline{j_{k,i}^Y}$  due to species mass fraction gradients and the Soret diffusion mass flux  $\overline{j_{k,i}^T}$  due to temperature gradients.

$$\overline{j_{k,i}} = \overline{j_{k,i}^Y} + \overline{j_{k,i}^T} \quad (3.53)$$

Fick's diffusion model relates the unfiltered diffusion mass flux  $j_{k,i}^Y$  to the molar concentration gradient multiplied by a mixture averaged diffusion constant of the species. Fick's model was originally developed for isothermal and isobaric systems [146]. The adaption of this model,

$$j_{k,i}^Y = -\rho D_k \frac{\partial Y_k}{\partial x_i}, \quad (3.54)$$

is not restricted to isothermal and isobaric systems. The diffusion mass flux is related to the species mass fraction gradient multiplied by the diffusion coefficient  $D_k$  of species  $k$  and the mixture density  $\rho$  [146]. Soret diffusion can

be modeled accordingly with the Soret diffusion coefficient  $D_k^T$ , the inverse temperature and the temperature gradient [82].

$$j_{k,i}^T = -D_k^T \frac{1}{T} \frac{\partial T}{\partial x_i} \quad (3.55)$$

The influence of SGS fluctuations on the diffusion mass flux is commonly neglected [119]. The filtered diffusion mass flux and the diffusion coefficients are simply calculated from the filtered field data. For convenience, the bar symbol is neglected in the equations of this section.

The mixture diffusion coefficients can be approximated from the binary diffusion coefficients  $D_{s,k}$  of species  $s$  towards species  $k$  [66] and the species molar or mass fraction distribution.

$$D_k = \frac{1 - X_k}{\sum_{s \neq k} \frac{X_s}{D_{s,k}}} = \frac{\sum_{s \neq k} \frac{Y_s}{W_s}}{\sum_{s \neq k} \frac{Y_s}{W_s D_{s,k}}} \quad (3.56)$$

The species mole fraction  $X_k$  can be obtained from the species mass fraction according to

$$X_k = \frac{W}{W_k} Y_k. \quad (3.57)$$

On the basis of the kinetic theory of gases, Hirschfelder, Bird and Spotz [68] developed an empirical approximation of the binary diffusion coefficients  $D_{j,k}$  in  $\text{m}^2 \text{s}^{-1}$  [146].

$$D_{s,k} = 10.1325 \frac{0.001858 T^{\frac{3}{2}} \left( \frac{1}{W_k} + \frac{1}{W_s} \right)}{p \left( \frac{\sigma_k + \sigma_s}{2} \right)^2 \Omega} \quad (3.58)$$

Here,  $\sigma_k$  is the collision diameter of species  $k$  and  $\Omega$  is the collision integral of the species pair  $(s, k)$ . The dimensionless collision integral can be obtained from the polynomial

$$\Omega = \frac{1.06036}{(T^*)^{0.15610}} + \frac{0.193}{e^{0.47635 T^*}} + \frac{1.03587}{e^{1.52996 T^*}} + \frac{1.76474}{e^{3.98411 T^*}} \quad (3.59)$$

depending on the dimensionless temperature  $T^*$  [14, 146]. The dimensionless temperature  $T^*$  is in turn calculated from the Boltzmann constant  $k_B$  and the characteristic Lennard-Jones energies  $\epsilon_s$  and  $\epsilon_k$  of species  $s$  and  $k$ .

$$T^* = \frac{k_B T}{\sqrt{\epsilon_s \epsilon_k}} \quad (3.60)$$

The Soret diffusion coefficients can also be derived from the kinetic theory of gases [28, 82]. However, Kuo and Acharya [91] presented a less complex empirical correlation for the Soret diffusion coefficients in  $\text{m}^2\text{s}^{-1}$ , which is also used in the commercial computational fluid dynamics software ANSYS Fluent [1].

$$D_k^T = 2.59 \times 10^{-7} T^{0.659} \left( \frac{W_k^{0.511} X_k}{\sum_{s=1}^{N_s} (W_s^{0.511} X_s)} - Y_k \right) \left( \frac{\sum_{s=1}^{N_s} (W_s^{0.511} X_s)}{\sum_{s=1}^{N_s} (W_s^{0.489} X_s)} \right) \quad (3.61)$$

### 3.6.2 Thermal Diffusivity Calculation

The thermal diffusivity of a species can also be obtained from the kinetic theory of gases [28]. This process is very time consuming during the simulation. The species thermal diffusivities are therefore usually calculated from a logarithmic temperature-dependent polynomial function [82].

$$\ln \alpha_k = \sum_{p=1}^{N_p} b_{p,k} (\ln T)^{p-1} \quad (3.62)$$

The  $N_p$  polynomial coefficients  $b_{p,k}$  of species  $k$  are determined beforehand by applying a least squares fit to the multicomponent thermal diffusivities according to Dixon-Lewis [28] calculated with Cantera [53]. This approach results in the polynomial coefficients in Table 3.1. The thermal diffusivity of the gas mixture  $\alpha$  is obtained from the species thermal diffusivities weighted by the respective molar fractions.

$$\alpha = \frac{1}{2} \left( \sum_{k=1}^{N_s} X_k \alpha_k + \frac{1}{\sum_{k=1}^{N_s} \frac{X_k}{\alpha_k}} \right) \quad (3.63)$$

### 3.6.3 Molecular Viscosity Calculation

Sutherland [134] developed a formula which correlates the molecular kinematic viscosity of a gas to the gas temperature and density.

$$\nu = \frac{1}{\rho} \frac{A_S T^{0.5}}{1 + \frac{T_S}{T}} \quad (3.64)$$

Species $k$	$b_{1,k}$	$b_{2,k}$	$b_{3,k}$	$b_{4,k}$
H	$-1.2641 \times 10^1$	3.7577	$-4.1121 \times 10^{-1}$	$1.8107 \times 10^{-2}$
H2	-3.9811	$1.8182 \times 10^{-1}$	$3.5016 \times 10^{-2}$	$6.5714 \times 10^{-4}$
O	-8.2918	1.3985	$-1.1468 \times 10^{-1}$	$5.7450 \times 10^{-3}$
OH	1.4017	-2.7769	$4.7742 \times 10^{-1}$	$-2.1145 \times 10^{-2}$
H2O	5.8774	-6.4774	1.1849	$-6.0185 \times 10^{-2}$
O2	$-1.1321 \times 10^1$	2.0295	$-1.5585 \times 10^{-1}$	$6.4087 \times 10^{-3}$
HO2	$-1.2187 \times 10^1$	2.1337	$-1.3225 \times 10^{-1}$	$4.2292 \times 10^{-3}$
H2O2	$-1.0996 \times 10^1$	1.4844	$-3.9149 \times 10^{-3}$	$-3.4662 \times 10^{-3}$
N2	1.5736	-3.5464	$6.4102 \times 10^{-1}$	$-3.1417 \times 10^{-2}$

**Table 3.1:** Polynomial coefficients for species thermal diffusivities  $\alpha_k$ .

Here,  $A_s$  and  $T_s$  are the Sutherland coefficient and the Sutherland temperature. In OpenFOAM [145], the standard Sutherland parameters are  $A_s = 1.67212 \text{ kg m}^{-1} \text{ s}^{-1} \text{ K}^{-0.5}$  and  $T_s = 170.672 \text{ K}$ . For hydrogen-air flames, the Sutherland law approximates the gas viscosity obtained from kinetic theory equations [28, 53, 82] reasonably well.

## 4 Inert LES of Turbulent Duct Flow

In the reference experiments of confined BLF, the flame is stabilized inside a rectangular premixing channel [34, 36]. In the reference experiments for unconfined BLF, the flame is stabilized at the exit of a premixing tube [30]. Turbulent flow prevails in the premixing channel and in the premixing tube. The flame is thus exposed to the turbulent velocity fluctuations of the inert channel and tube flow. The approaching turbulent flow strongly influences the boundary layer separation characteristics and turbulent flame wrinkling. The accurate prediction of the inert base flow is therefore decisive for the accurate prediction of the boundary layer flashback behaviour.

The numerical simulations of boundary layer flashback are divided into two parts. First the turbulent channel flow is calculated with inert LES. The time-dependent velocity profile at the outlet of the channel domain is then sampled and mapped to the inlet of the reactive LES of BLF. The numerical setup and the results of the inert simulations are presented in the following sections.

### 4.1 Numerical Setup for Inert LES

The inert flow in the premixing channel was investigated by Eichler prior to the confined flashback experiments. It was shown that the channel flow has the self-similar structure of a fully developed turbulent boundary layer [35] and that the wall-shear stresses are similar to a fully developed turbulent channel flow [34, 35]. For the unconfined reference case of Duan et al. [30], the fully developed character of the turbulent pipe flow was not proven. The fully developed character of the pipe flow was nevertheless assumed for the calculation of the critical velocity gradients [30]. In a different burner configuration, the velocity gradients at the wall of a not fully developed turbulent

pipe flow only showed a deviation of 4 % from the velocity gradient of a fully developed velocity profile [5]. The goal of the inert numerical simulations is therefore to reproduce a fully developed channel and pipe flow as accurately as possible.

#### 4.1.1 Discretization Schemes

The governing equations in OpenFOAM are solved by applying a finite volume discretization of the computational domain. The governing equations are integrated over finite volumes and the volume integrals are approximated by surface integrals according to Gauss' theorem [75]. This requires the calculation of surface fluxes and an interpolation of the cell centred field variables to the face centres. The second order accurate central differencing scheme [75] and the flux limited central differencing scheme [75, 135] are used for this interpolation. Time derivatives are discretized by the second order accurate quadratic backward differencing scheme [41, 75]. The time step size is dynamically adapted during runtime in order to ensure that the non-acoustic cell Courant number is kept below 0.8.

#### 4.1.2 Computational Grid for Channel Simulations

A fully developed channel flow is obtained at large distances from the channel inlet [120]. A long channel domain would imply large cell numbers and large computational resources. A fully developed boundary layer is therefore usually achieved by simulating a short channel and mapping the outlet velocity profile to the inlet of the domain in each timestep. Following the LES studies of Mukha and Liefvendahl [111], the channel is modeled by a cuboid domain as depicted in Figure 4.1. The initial channel domain has a half height of  $\delta = 8.75$  mm, a length of  $L = 6\delta$  and a width of  $W = 3\delta$ . Mapping of the velocity field from the channel outlet to the inlet is achieved by applying cyclic boundary conditions to the inlet and outlet. The quasi two-dimensional character of an infinitely wide channel is obtained by also applying cyclic boundary conditions to the front and back patches of the channel. The aspired channel bulk velocity is sustained by an average driving pressure gradient over the channel

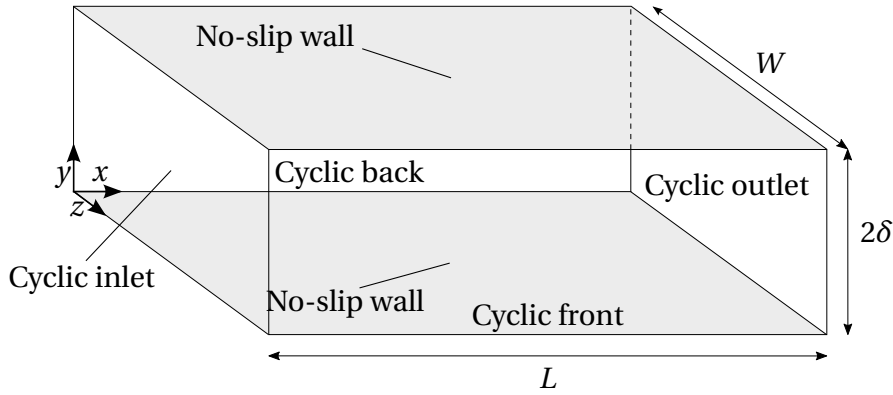


**Figure 4.1:** Computational domain for inert channel simulations.

length. The average pressure gradient is calculated in each iteration from the difference of the targeted bulk velocity and the average velocity resulting from the solution of the momentum equation.

The relevant combustion and flow phenomena take place very close to the wall in boundary layer flashback. The boundary layer has to be fully resolved by the computational grid for an accurate representation of boundary layer separation and of flame quenching at walls. The walls are therefore modelled as no-slip walls. The velocity of the first cell adjacent to the wall is not approximated by a wall model but directly obtained from the solution of the governing equations. This requires small wall-normal ( $y$ ) cell sizes near walls. The non-dimensional distance  $y_W^+$  of the cell center adjacent to a wall is kept significantly below  $y_W^+ = 1$ , as seen in Table 4.1. The wall-normal cell size linearly increases in wall normal direction. The wall-normal height of the largest cell at the channel center is ten times the cell height at the wall. The cells are uniformly spaced in streamwise ( $x$ ) and spanwise ( $z$ ) direction. The non-dimensional cell sizes  $\Delta x^+$ ,  $\Delta y^+$  and  $\Delta z^+$  are listed in Table 4.1 together with the resulting cell counts  $N_x$ ,  $N_y$  and  $N_z$ . All cell sizes are non-dimensionalized by the kinematic viscosity  $\nu$  and the friction velocity  $u_{\tau, Pope}$  estimated from the empirical correlation

$$u_{\tau, Pope} = 0.09 \frac{\nu}{\delta} \text{Re}^{0.88}. \quad (4.1)$$

The friction velocity  $u_{\tau, Pope}$  was fitted by Pope [122, p. 279] to experimental channel flow data. The Reynolds number  $\text{Re}$  is calculated from the channel

$U_b$	Re	$u_{\tau,Pope}$ in $\text{ms}^{-1}$	$\text{Re}_{\tau,Pope}$	$y_W^+$	$\Delta x^+$	$\Delta y^+$	$\Delta z^+$	$N_x \times N_y \times N_z$
$6\text{ms}^{-1}$	5833	0.382	185.4	0.60	13.73	12.35	8.97	$81 \times 38 \times 62$
$10\text{ms}^{-1}$	9722	0.598	290.7	0.63	13.42	12.52	8.90	$130 \times 118 \times 98$
$20\text{ms}^{-1}$	19444	1.101	535.2	0.66	13.72	13.11	9.02	$234 \times 208 \times 178$
$30\text{ms}^{-1}$	29167	1.573	764.4	0.79	18.35	16.24	12.07	$250 \times 240 \times 190$

**Table 4.1:** Initial simulation parameters for the inert channel simulations.

height  $2\delta$  and the bulk velocity  $U_b$ .

$$\text{Re} = \frac{2\delta U_b}{\nu} \quad (4.2)$$

The Reynolds number calculated from the friction velocity is the friction Reynolds number  $\text{Re}_{\tau}$ ,

$$\text{Re}_{\tau} = \frac{\delta u_{\tau}}{\nu}. \quad (4.3)$$

The kinematic viscosity is set to  $\nu = 1.8 \times 10^{-5} \text{m}^2 \text{s}^{-1}$ . This is a good approximation to the kinematic viscosities of the fresh gas mixture. The actual viscosities at atmospheric pressure vary between  $\nu = 1.71 \times 10^{-5} \text{m}^2 \text{s}^{-1}$  at  $\Phi = 0.33$  and  $\nu = 1.94 \times 10^{-5} \text{m}^2 \text{s}^{-1}$  at  $\Phi = 0.75$ . The Reynolds numbers, the predicted friction velocities  $u_{\tau,Pope}$  and the friction Reynolds numbers  $\text{Re}_{\tau,Pope}$  calculated with the predicted friction velocity  $u_{\tau,Pope}$  are also listed in Table 4.1 for the different bulk velocities.

### 4.1.3 Computational Grid for Pipe Simulations

The numerical unconfined flashback limits are compared to experimental flashback limits of a tube burner with a diameter of  $d = 21.16 \text{mm}$ . The bulk velocity in the tube is  $9 \text{ms}^{-1}$ . The computational domain for the inert pipe simulations is depicted in Figure 4.2 (a). It consists of cyclic inlet and outlet patches and the no-slip pipe walls. The pipe is discretized by an o-grid in order to ensure a good mesh quality. A quarter of the inlet mesh is depicted in Figure 4.2 (b). The rectangular core grid has an edge length of  $15.87 \text{mm}$  and is discretized by 57 cells in each direction. The outer circular part of the grid consists of 228 cells in circumferential direction and 47 cells in radial direction

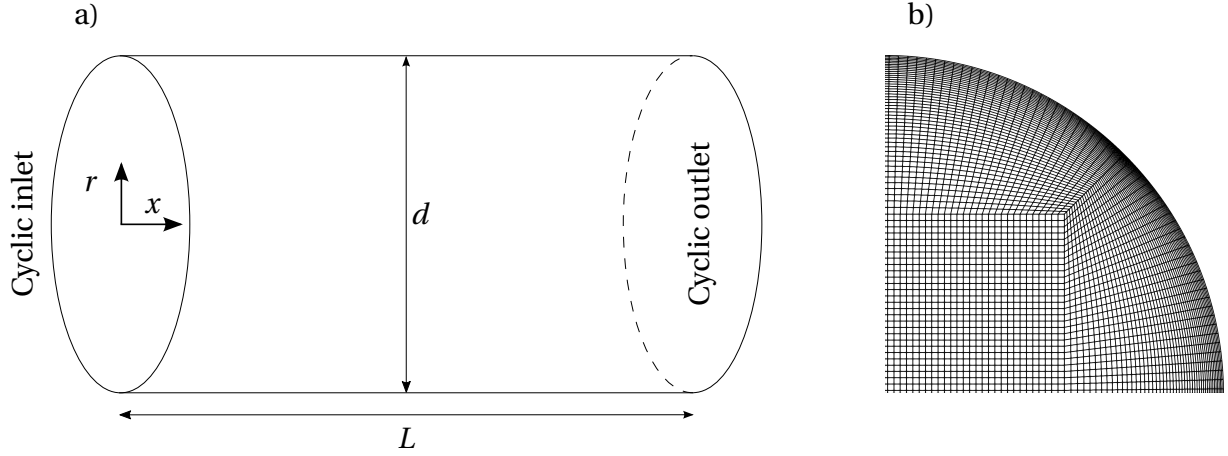


**Figure 4.2:** Computational domain for inert pipe simulations (a) and spatial discretization of the inlet (b).

$r$ . The pipe length of  $L = 6d$  is discretized by 283 cells. The pipe friction factor  $f = 8u_\tau^2/U_b^2$  [127] can be well approximated by the correlation of Blasius [7],

$$f = 0.3164\text{Re}^{-0.25}. \quad (4.4)$$

This leads to the friction velocity for fully developed pipe flow  $u_{\tau,Blasius}$ :

$$u_{\tau,Blasius} = 0.03955^{0.5}\text{Re}^{-0.125}U_b. \quad (4.5)$$

The pipe Reynolds number  $\text{Re}$  is defined as

$$\text{Re} = \frac{U_b d}{\nu}. \quad (4.6)$$

The Reynolds number at a bulk velocity of  $9\text{ m s}^{-1}$  and a viscosity of  $\nu = 1.8 \times 10^{-5}\text{ m}^2\text{ s}^{-1}$  is  $\text{Re} = 10580$  and the friction velocity is  $u_{\tau,Blasius} = 0.562\text{ m s}^{-1}$ . This results in non-dimensional cell sizes of  $\Delta x^+ = 14.01$  in streamwise direction,  $\Delta r_W^+ = 1.32$  in radial direction and  $\Delta(r\varphi)_W^+ = 9.10$  in circumferential direction at the wall. The cell size in the rectangular mesh in the center of the pipe is  $\Delta y^+ = \Delta z^+ = 6.15$ .

#### 4.1.4 Turbulence Model Parameters

The model constants for the Smagorinsky model in Equation (3.32) are set to  $c_k = 0.094$  and  $c_\epsilon = 1.048$ . These are the standard model constants for the

Smagorinsky model in OpenFOAM [145]. The model constants are equivalent to a Smagorinsky constant of  $c_S = 0.168$  according to Equation (3.33). This is close to the Smagorinsky constant of  $c_S = 0.17$  originally proposed by Lilly [103]. The standard OpenFOAM values  $C_\Delta = 0.158$  and  $A^+ = 26$  are chosen for the van Driest damping constants in Equation (3.34) [109, 145].

## 4.2 Results of Inert LES

Boundary layer flashback is strongly influenced by the velocity field in the premixing duct ahead of the flame. The velocity gradient at the wall is particularly important for confined BLF as confined BLF is initiated by boundary layer separation [34]. Turbulent velocity fluctuations also affect the BLF limits as they influence flame wrinkling and the turbulent flame speed. It is thus essential to ensure that the average velocity profile, the average velocity gradient at the wall and the average turbulent velocity fluctuations are well represented by the inert numerical simulations. This is ensured by comparing the LES results with DNS results from literature.

### 4.2.1 Inert Duct Flow with the Smagorinsky Turbulence Model

The inert channel and pipe flow obtained with the Smagorinsky turbulence model are investigated first. This investigation refines the analysis of the inert channel flow by Endres and Sattelmayer [38].

#### 4.2.1.1 Inert Channel Flow

The DNS results of Moser et al. [110] are chosen as reference results for the inert channel flow. The averaging intervals for the LES fields are given in Table 4.2 in channel flow-through times. These averaging intervals are sufficient to obtain statistical convergence of the second order moments. Wall normal velocity and turbulence profiles are obtained from subsequent averaging in streamwise and spanwise direction. No wall model is used. The LES friction velocity  $u_{\tau,LES}$  can therefore be directly obtained from the average wall-

$U_b$	Averaging Interval	$u_{\tau,LES}$ in $\text{ms}^{-1}$	$\left  \frac{u_{\tau,LES} - u_{\tau,Pope}}{u_{\tau,Pope}} \right $	$\text{Re}_{\tau}$	Peak value of total TKE
$6 \text{ms}^{-1}$	123	0.369	3.4%	179.5	$k_{tot}/u_{\tau}^2 = 4.55$ at $y/\delta = 0.126$
$10 \text{ms}^{-1}$	255	0.585	2.2%	284.5	$k_{tot}/u_{\tau}^2 = 4.42$ at $y/\delta = 0.070$
$20 \text{ms}^{-1}$	128	1.076	2.3%	522.8	$k_{tot}/u_{\tau}^2 = 4.62$ at $y/\delta = 0.039$
$30 \text{ms}^{-1}$	25	1.533	2.5%	745.4	$k_{tot}/u_{\tau}^2 = 4.67$ at $y/\delta = 0.027$

**Table 4.2:** Channel flow results of LES with the Smagorinsky turbulence model.

normal gradient of the streamwise velocity component  $u_x$  at the wall.

$$u_{\tau,LES} = \left( \nu \left. \frac{\partial \bar{u}_x}{\partial y} \right|_W \right)^{0.5} \quad (4.7)$$

The LES friction velocities are given in Table 4.2 together with the deviation from the friction velocity  $u_{\tau,Pope}$ . The deviation of the LES friction velocity from the empirical correlation value is 3.4% for  $U_b = 6 \text{ms}^{-1}$  and not higher than 2.5% for higher velocities. The deviation is notably higher at  $U_b = 6 \text{ms}^{-1}$  than at higher velocities. The predicted LES friction velocities however match the values from the empirical correlation (4.1) sufficiently well at all bulk velocities. The numerical accuracy is higher than the 4% accuracy of friction velocity measured by Baumgartner [5] for flashback experiments.

The average velocity profiles from the LES are compared to DNS results of Moser et al. [110] in Figure 4.3. The friction Reynolds numbers of the LES results are calculated according to equation (4.3) with the LES friction velocity  $u_{\tau,LES}$ . The friction velocity  $u_{\tau,LES}$  and the viscosity are used for non-dimensionalizing the profiles. The LES reproduce the self-similar DNS profiles in the viscous sublayer ( $y^+ < 5$ ) very well. The velocity is however slightly underestimated in the buffer layer at approximately  $7 < y^+ < 30$  by the LES at all Reynolds numbers. For friction Reynolds numbers  $\text{Re}_{\tau} = 284.5$ ,  $\text{Re}_{\tau} = 522.8$  and  $\text{Re}_{\tau} = 745.4$ , the DNS profiles at higher wall distances ( $y^+ > 30$ ) are well reproduced by the LES. Here, the velocity is only slightly overestimated in the LES. The  $\text{Re}_{\tau} = 179.5$  simulation however shows a large deviation from the DNS reference profile at  $\text{Re}_{\tau} = 180$ . The LES profile does not show a distinct logarithmic region with a constant slope but a more rounded shape at higher

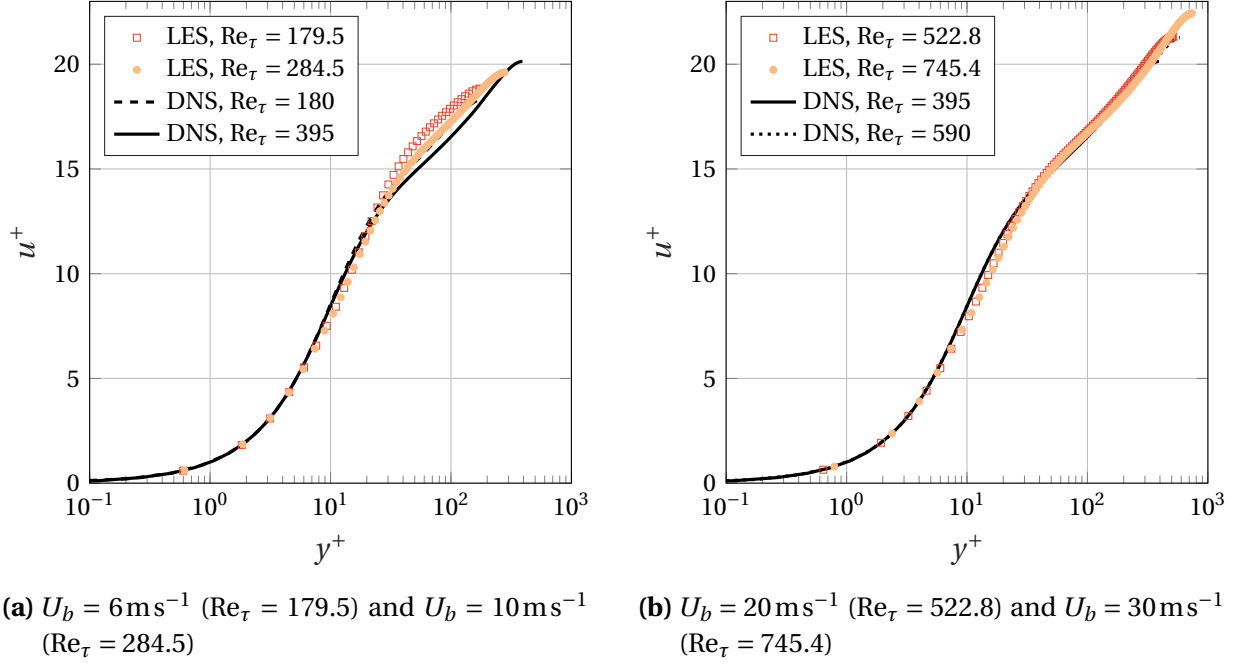


**Figure 4.3:** Average velocity profiles of the turbulent channel flow compared to DNS results of Moser et al. [110].

wall distances. Except for the simulation at  $U_b = 6 \text{ ms}^{-1}$ , the average velocity profiles are thus well reproduced by the LES.

A similar conclusion can be drawn from the turbulent kinetic energy (TKE) profiles in Figure 4.4. Here, the LES profiles are again compared to DNS results of Moser et al. [110]. Similar to the TKE of DNS, the resolved TKE  $k_{res}$  of LES is obtained by subsequently averaging the time averaged velocity fluctuations in streamwise and spanwise direction.

$$k_{res} = k_{DNS} = 0.5 \left( \overline{u'_i u'_i} \right) \quad (4.8)$$

The total TKE of LES  $k_{tot}$  is the sum of the resolved TKE  $k_{res}$  and the SGS TKE  $k_{SGS}$ . As expected, the peak total TKE for  $\text{Re}_\tau = 284.5$  lies between the DNS values of  $k_{DNS}/u_\tau^2 = 4.10$  at  $y/\delta = 0.086$  for  $\text{Re}_\tau = 180$  and  $k_{DNS}/u_\tau^2 = 4.57$  at  $y/\delta = 0.043$  for  $\text{Re}_\tau = 395$ . The peak total TKE for  $\text{Re}_\tau = 522.8$  also lies between the DNS peak at  $\text{Re}_\tau = 395$  and the peak value of  $k_{DNS}/u_\tau^2 = 4.75$  at  $y/\delta = 0.03$  for  $\text{Re}_\tau = 590$ . As expected for  $\text{Re}_\tau = 745.4$ , the peak total TKE lies at lower relative wall distances than the DNS peak for  $\text{Re}_\tau = 590$ . The peak value of

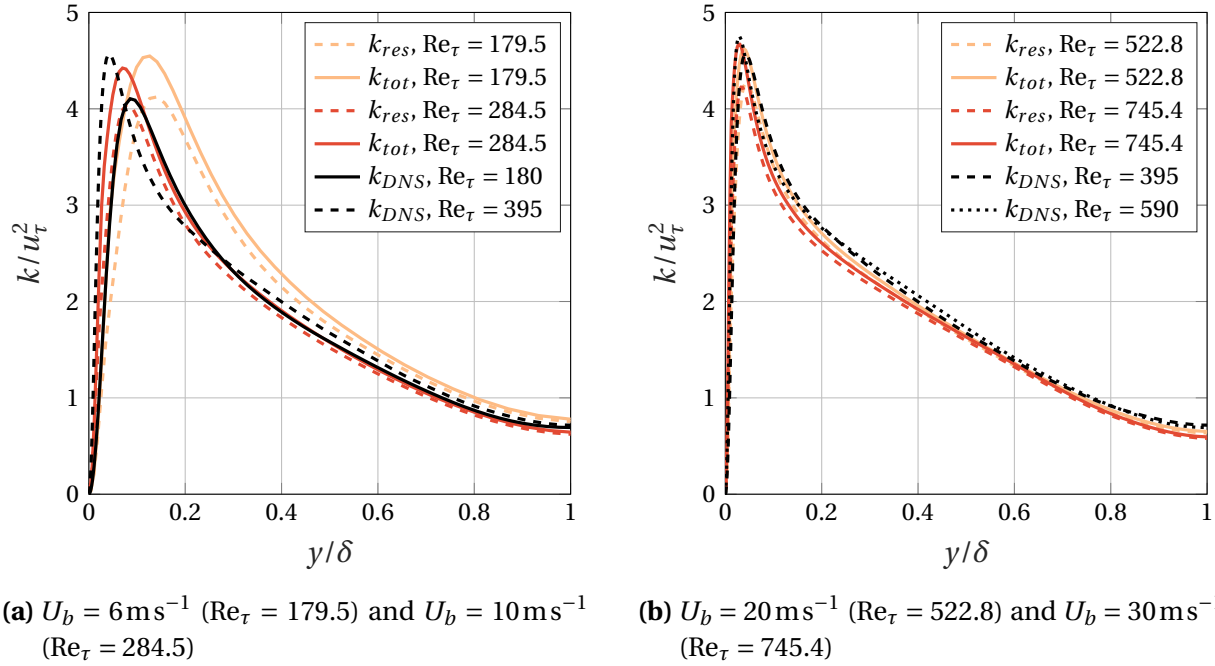


**Figure 4.4:** Turbulent kinetic energy profiles of the turbulent channel flow compared to DNS results of Moser et al. [110].

$k_{tot}$  is however underestimated as it is expected to be higher than the peak value for  $\text{Re}_\tau = 590$ . The overall prediction of the LES TKE profiles for bulk velocities of  $10 \text{ ms}^{-1}$ ,  $20 \text{ ms}^{-1}$  and  $30 \text{ ms}^{-1}$  are very accurate. The peak of TKE of the  $6 \text{ ms}^{-1}$  case on the contrary does not reproduce the expected peak of the DNS profile at  $\text{Re}_\tau = 180$ . The relative wall distance of the peak total TKE is overestimated by 10.9% and the wall distance of the peak is 46.5% higher than the expected location. The resolved TKE profile shows that the overall TKE overestimation is not solely caused by the SGS velocity fluctuations, but also by the non-dimensional resolved velocity fluctuations. This is partly caused by scaling the results with the underestimated LES friction velocity.

In summary, the overall trend of the velocity profiles and velocity fluctuation profiles for bulk velocities of  $10 \text{ ms}^{-1}$ ,  $20 \text{ ms}^{-1}$  and  $30 \text{ ms}^{-1}$  is captured by LES with the Smagorinsky turbulence model [38]. For  $U_b = 6 \text{ ms}^{-1}$  however, the current configuration fails to reproduce DNS results. The reason for this failure will be investigated in sections 4.2.2 and 4.2.3.

#### 4.2.1.2 Inert Pipe Flow

The inert pipe flow is also analyzed in regard to the prediction of DNS profiles of average velocity and TKE. The fields are therefore averaged in time over 10.3 pipe flow-through times. The time averaged fields are sampled on a longitudinal cutting plane. Average profiles of streamwise velocity and total TKE are obtained by subsequently averaging the fields in streamwise direction. The LES friction velocity from the average velocity profile at  $U_b = 9 \text{ m s}^{-1}$  is  $u_{\tau,LES} = 0.544 \text{ m s}^{-1}$  according to Equation (4.7). The LES friction velocity is thus 3.2% lower than the expected Blasius friction velocity  $u_{\tau,Blasius} = 0.562 \text{ m s}^{-1}$  according to Equation (4.5). The pipe friction Reynolds number is

$$\text{Re}_\tau = \frac{du_\tau}{2\nu}. \quad (4.9)$$

The friction Reynolds number calculated from the LES friction velocity is  $\text{Re}_\tau = 319.8$ .

The LES results are compared to the reference DNS data of El Khoury et al. [37] at a Reynolds number of  $\text{Re} = 11700$  and a friction Reynolds number of  $\text{Re}_\tau = 360$ . The order of magnitude of the DNS Reynolds numbers is similar to the LES Reynolds numbers. They are however not identical. DNS profiles at  $\text{Re}_\tau = 180$  are therefore additionally included in the comparison. Figure 4.5 shows the non-dimensional average streamwise velocity profile and the average TKE profiles from LES compared to DNS profiles. It is evident that the LES velocity profile follows the DNS profiles very well up to  $r^+ \approx 30$ . Although the DNS profile at  $\text{Re}_\tau = 360$  should be reproduced by the LES profile, the logarithmic region of the LES profile has a higher inclination at higher wall distances and represents the DNS profile at  $\text{Re}_\tau = 180$  better than the  $\text{Re}_\tau = 360$  profile. The non-dimensional velocity is thus overestimated compared to the  $\text{Re}_\tau = 360$  DNS case. This was already observed for the channel flow at low velocities. The shape of the velocity profile however represents the shape of the DNS profile very well. The deviation from the expected profile can therefore be traced back to the underestimation of the friction velocity which influences the inclination of the non-dimensional profile.

Similar to the channel TKE profiles at low velocities, the pipe simulation over-

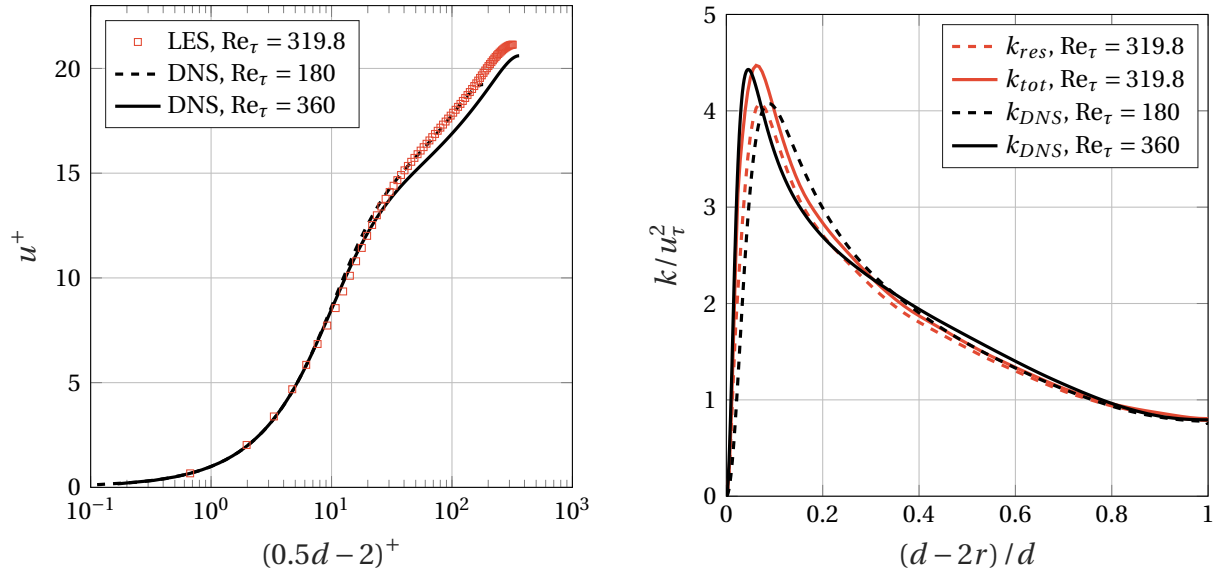


**Figure 4.5:** Average velocity profile and turbulent kinetic energy profiles of the turbulent pipe flow compared to DNS results of El Khoury et al. [37].

estimates the turbulent velocity fluctuation peak. The peak of the DNS data at  $Re_\tau = 360$  is  $k_{DNS}/u_\tau^2 = 4.43$  at  $(d - 2r)/d = 0.046$ . The peak of the LES TKE profile in Figure 4.5 is  $k_{tot}/u_\tau^2 = 4.47$  at  $(d - 2r)/d = 0.062$ . The location of the LES turbulence peak is correctly predicted at higher wall distances than the DNS profile at  $Re_\tau = 360$ . The maximum value of TKE is however expected to be lower than the DNS value. The shape of the LES profile nevertheless matches the shape of the DNS profile reasonably well. The overestimation of the non-dimensional turbulence peak can again be explained by the underestimation of the friction velocity.

#### 4.2.2 Duct Length Influence

Chin et al. [16] investigated the duct length influence on DNS results of turbulent pipe flow. They observed an overestimation in peak turbulence intensity for pipes of insufficient length. They recommended a non-dimensional minimum pipe length of  $L^+ = 2100$  and  $L^+ = 3100$  for friction Reynolds numbers of  $Re_\tau = 170$  and  $Re_\tau = 500$ . These minimum pipe lengths ensure that the

turbulence intensity profiles are independent of the computational domain size. In the present LES, the non-dimensional channel length is  $L^+ = 1076$ ,  $L^+ = 1706$ ,  $L^+ = 3138$  and  $L^+ = 4471$  for friction Reynolds numbers  $Re_\tau = 179.5$ ,  $Re_\tau = 284.5$ ,  $Re_\tau = 522.8$  and  $Re_\tau = 745.4$ , respectively. The non-dimensional pipe length is  $L^+ = 3837$  at a friction Reynolds number  $Re_\tau = 319.8$ . The channel cases with lower bulk velocities  $U_b = 6 \text{ ms}^{-1}$  and  $U_b = 10 \text{ ms}^{-1}$  thus do not fulfill the duct length criterion of Chin et al. [16]. The turbulence intensity is not overestimated at a bulk velocity of  $U_b = 10 \text{ ms}^{-1}$  in the current LES. An overestimation of turbulence intensity is however observed at a bulk velocity of  $U_b = 6 \text{ ms}^{-1}$ . The influence of the duct length on the profiles are therefore analyzed. For this purpose, the  $6 \text{ ms}^{-1}$  and  $10 \text{ ms}^{-1}$  channel simulations are repeated with longer channel domains of  $L = 12\delta$  and  $L = 25.2\delta$  with corresponding channel widths of  $W = 6\delta$  and  $W = 12.6\delta$ .

The total TKE profiles of the longer channel cases are compared to the shorter channel results in Figure 4.6. The corresponding friction velocities, friction Reynolds numbers and peak values of total TKE resulting from the total TKE profiles are listed in Table 4.3. The peak total TKE at  $U_b = 6 \text{ ms}^{-1}$  decreases by 4.3% when increasing the channel length to  $L = 12\delta$ . The peak TKE value is however still higher than the DNS value and the turbulence peak position is not improved. By further increasing the channel length and width, the TKE peak is slightly reduced by 2.8%. Although the peak is now only 0.5% higher than the DNS value, it is still located at significantly higher wall distances than the DNS peak. The whole LES profile in Figure 4.6 is shifted to higher wall distances compared to the DNS profile. The channel length is consequently a reason for the overestimation of the turbulence level but not for the shift to higher wall distances. For  $U_b = 10 \text{ ms}^{-1}$ , the  $L = 25.2\delta$  channel reduces the turbulence peak by 1.6% without changing the wall distance of the turbulence peak. It can thus be concluded that the shorter channel with  $L = 6\delta$  is of sufficient length to reproduce the  $10 \text{ ms}^{-1}$  turbulence profile. For  $U_b = 6 \text{ ms}^{-1}$  however, a longer channel is necessary. The  $L = 12\delta$  channel will therefore be used for the following investigation of the inert flow at  $U_b = 6 \text{ ms}^{-1}$ .

Chin et al. [16] concluded that even when the duct length may be sufficient for providing accurate turbulence profiles, it may still be insufficient to pre-

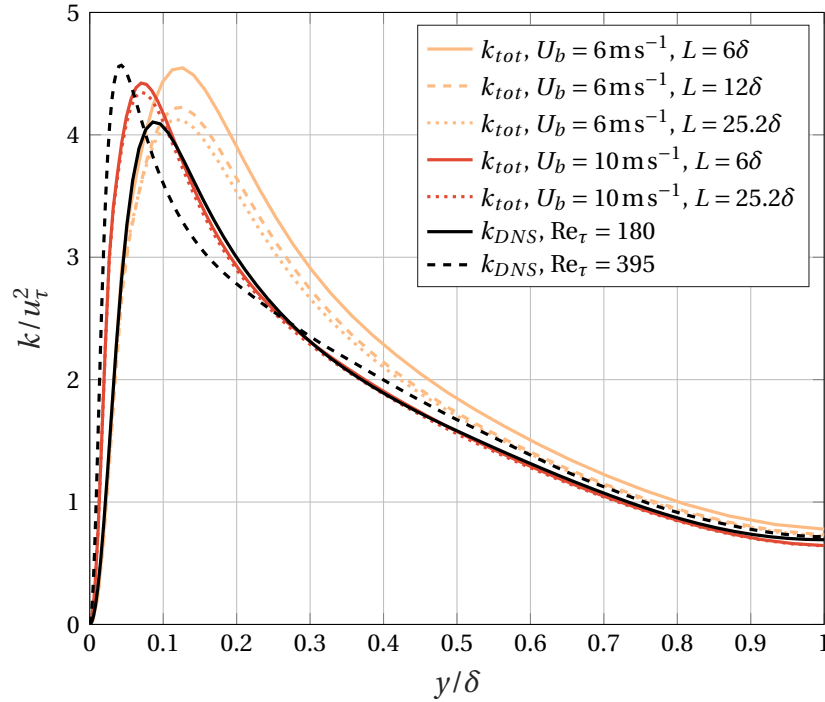


**Figure 4.6:** Duct length influence on turbulent kinetic energy profiles of the turbulent channel flow at  $U_b = 6 \text{ m s}^{-1}$  and  $U_b = 10 \text{ m s}^{-1}$  compared to DNS results of Moser et al. [110].

$U_b$	$L$	$u_{\tau,LES}$ in $\text{m s}^{-1}$	$\left  \frac{u_{\tau,LES} - u_{\tau,Pope}}{u_{\tau,Pope}} \right $	$Re_{\tau}$	Peak value of total TKE
$6 \text{ m s}^{-1}$	$6\delta$	0.369	3.4%	179.5	$k_{tot}/u_{\tau}^2 = 4.55$ at $y/\delta = 0.126$
$6 \text{ m s}^{-1}$	$12\delta$	0.366	4.2%	177.9	$k_{tot}/u_{\tau}^2 = 4.23$ at $y/\delta = 0.126$
$6 \text{ m s}^{-1}$	$25.2\delta$	0.368	3.7%	187.9	$k_{tot}/u_{\tau}^2 = 4.12$ at $y/\delta = 0.112$
$10 \text{ m s}^{-1}$	$6\delta$	0.585	2.2%	284.5	$k_{tot}/u_{\tau}^2 = 4.67$ at $y/\delta = 0.070$
$10 \text{ m s}^{-1}$	$25.2\delta$	0.585	2.2%	284.6	$k_{tot}/u_{\tau}^2 = 4.35$ at $y/\delta = 0.070$

**Table 4.3:** Channel length influence on inert LES results with the Smagorinsky turbulence model.

vent a correlation between the unsteady inlet and outlet velocity profiles. This can lead to artificial lengthening of the turbulence structures. Duct lengths over  $8\pi\delta$  prevent this artificial lengthening of turbulence structures according to Chin et al. [16]. For the reactive simulations at  $U_b = 6 \text{ m s}^{-1}$ , the time-dependent velocity profiles are therefore sampled from the  $L = 25.2\delta$  channel to ensure the best results possible. For higher velocities, it still has to be shown

that the short channel length does not affect the flashback behaviour.

### 4.2.3 Turbulence Model Influence on Low Reynolds Number Flow

The Smagorinsky turbulence model is not capable of accurately reproducing the DNS velocity and turbulence profiles at the lowest velocity under investigation. Significant low Reynolds effects are observed in the reference DNS results for a friction Reynolds number of  $Re_\tau = 180$ . The velocity profile does not agree with the higher Reynolds number cases beyond  $y^+ = 10$ . The logarithmic layer is shorter and has a larger intercept than in higher Reynolds number cases [110]. Formally, both the Smagorinsky model and the dynamic one-equation model are only valid for high Reynolds number flows. In addition, the constant model parameters of the Smagorinsky turbulence model are not optimized for simulating low Reynolds number flows. The model parameters of the dynamic one-equation model dynamically adapt to local flow characteristics. The dynamic one-equation model is therefore expected to deliver better results when applied to low Reynolds simulations. This is investigated in this section together with implicit turbulence modelling in OpenFOAM and its capability to reproduce the low Reynolds number effects at  $U_b = 6 \text{ m s}^{-1}$ .

Figure 4.7 shows the average velocity and turbulent kinetic energy profiles obtained with the Smagorinsky model, the dynamic one-equation model and the implicit turbulence model at  $U_b = 6 \text{ m s}^{-1}$ . The dynamic one-equation model and the implicit turbulence model reproduce the DNS velocity profile for  $Re_\tau = 180$  better than the Smagorinsky model. The logarithmic region is well recognizable and the slope is closer to the DNS profile than with the Smagorinsky model. A deviation from the DNS profile in the buffer layer is not detectable. The comparison between the dynamic one-equation model and the implicit turbulence model shows that the slope of the logarithmic layer is closer to the DNS results with the implicit turbulence model than with the dynamic one-equation model. This is underlined by the friction velocities which are  $u_{\tau,LES} = 0.371$  with implicit turbulence modelling and  $u_{\tau,LES} = 0.367$  with the dynamic one-equation turbulence model. The LES friction velocity obtained with the Smagorinsky model has a deviation of 3.4% from the empirical

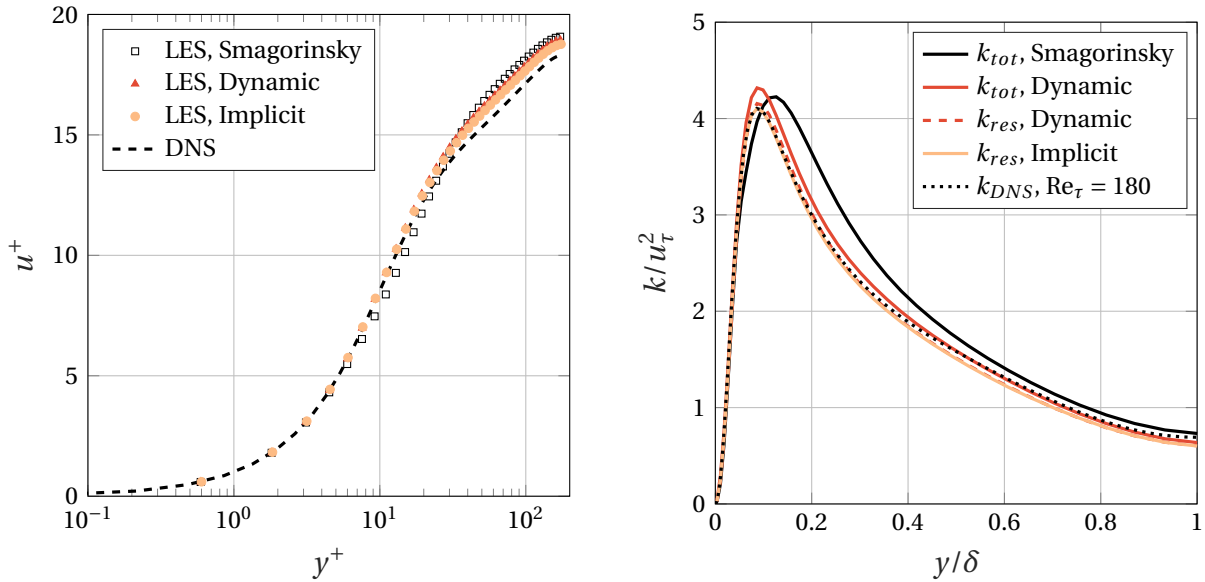


**Figure 4.7:** Turbulence model influence on average velocity and turbulent kinetic energy profiles of the turbulent channel flow at  $U_b = 6 \text{ m s}^{-1}$  compared to DNS results of Moser et al. [110] at  $Re_\tau = 180$ .

value  $u_{\tau, \text{Pope}}$ . The friction velocity error decreases to 2.8% with implicit turbulence modelling while it increases to 3.7% with the dynamic one-equation model.

The resolved TKE profiles in Figure 4.7 resemble the DNS profile very well. Both the dynamic one-equation model and the implicit turbulence model lead to a resolved turbulence peak at the same relative wall distance as the DNS profile. The maximum resolved non-dimensional TKE with the implicit turbulence model is also identical to the maximum non-dimensional TKE obtained with DNS. The resolved non-dimensional TKE peak of  $k/u_\tau^2 = 4.15$  with the dynamic one-equation model is only 1.2% higher than the DNS peak. The one-equation model however introduces SGS turbulence in addition to the resolved TKE, which leads to an overestimation of the total TKE compared to the DNS profile. This shows that no turbulence model is needed at  $U_b = 6 \text{ m s}^{-1}$  in addition to the numerical diffusion of the discretization schemes. Moreover, the numerical diffusion is small enough to achieve good results with the LES. The implicit turbulence model is therefore chosen for the inert simulations at  $U_b = 6 \text{ m s}^{-1}$ .

The dynamic one-equation model shows better performance than the Smagorinsky model at predicting the low Reynolds flow. This result can however not be transferred to higher Reynolds numbers. Additional simulations at higher Reynolds numbers show that the friction velocity has a larger deviation from  $u_{\tau, Pope}$ , that the non-dimensional velocity at high wall distances is overestimated and that turbulence at higher wall distances is underestimated with the dynamic one-equation model. The DNS velocity profile in the buffer layer and the turbulence peak on the other hand are reproduced more accurately with the dynamic one-equation model. The one-equation model thus has no clear advantage over the Smagorinsky model. As the numerical effort is larger with the one-equation model due to the additional transport equation, the Smagorinsky model is preferred for the higher Reynolds cases.

#### 4.2.4 Summary of Inert LES Results

In summary, the chosen numerical setup with the Smagorinsky model is capable of accurately representing DNS profiles of average streamwise velocity and average TKE at most simulated bulk velocities. The Smagorinsky model only fails to reproduce the DNS profiles at a bulk velocity of  $U_b = 6 \text{ ms}^{-1}$ . At this bulk velocity, the implicit turbulence model delivers very accurate results. The numerically more expensive dynamic one-equation model is not superior to the Smagorinsky model at high Reynolds numbers or to the implicit turbulence model at low Reynolds numbers. The implicit turbulence model is therefore chosen for the reactive simulations at  $U_b = 6 \text{ ms}^{-1}$ , while the Smagorinsky model is used for reactive simulations at higher bulk velocities. It is further shown that the chosen duct length of  $L = 6\delta$  is sufficient for reproducing the profiles at bulk velocities of  $10 \text{ ms}^{-1}$  and higher. For  $U_b = 6 \text{ ms}^{-1}$  a longer channel is necessary in order to obtain reasonable results. For the short channel it remains to be assessed whether the chosen channel length affects the predicted flashback limits.

## 5 Reactive LES of Confined Boundary Layer Flashback

The unsteady velocity field from the inert simulations is used as the base flow for the reactive simulations of BLF. The objective is to accurately reproduce experimental flashback limits, obtain flashback results at new operating conditions and to get a more detailed insight into the combustion parameters during upstream flame propagation at different operating conditions. This is achieved by performing flashback simulations at bulk velocities of  $6 \text{ ms}^{-1}$ ,  $10 \text{ ms}^{-1}$ ,  $20 \text{ ms}^{-1}$  and  $30 \text{ ms}^{-1}$  and at thermodynamic pressures of 0.5 bar, 1 bar, 2 bar and 3 bar.

The numerical setup for the confined BLF simulations is presented hereafter. This is followed by the results of the confined BLF simulations at different bulk velocities and pressures.

### 5.1 Numerical Setup for Confined Flashback Simulations

The numerical model presented in Section 3 is used for the numerical simulations of confined BLF. The low Mach number approximation is applied in order to prevent artificial pressure fluctuations. The governing equations are discretized with the same discretization schemes as in the inert calculations (see Chapter 4.1.1). The non-acoustic Courant number is again kept below 0.8. The SGS Schmidt and Prandtl numbers are set to one. In accordance with the inert results, the Smagorinsky model with van Driest damping is used for bulk velocities of  $10 \text{ ms}^{-1}$  and higher, while implicit turbulence modelling is applied at a bulk velocity of  $6 \text{ ms}^{-1}$ . The turbulence model parameters are not changed compared to the inert simulations (see Chapter 4.1.4).

Combustion is modelled with the quasi-laminar combustion model and the detailed chemical reaction mechanism of Burke et al. [15]. The Seulex ordinary differential equations solver [63] is applied for solving the chemical kinetics system. In-situ adaptive tabulation [20, 123] is applied in order to avoid the computationally costly process of solving the chemical kinetics system at each time step for every cell. Here, the results from the direct solution of the chemical kinetics system are stored in a look-up table during runtime. The look-up table can then be used for mapping the gas composition, pressure and temperature from previous solver iterations to the current iteration. The mapping process is approximated by a linear mapping gradient matrix. The maximum error of the linear mapping is set to  $10^{-4}$ .

### 5.1.1 Computational Grid and Boundary Conditions

Confined BLF was investigated experimentally by Eichler et al. [34]. They studied flame flashback in a rectangular channel burner at atmospheric pressure. The stainless steel walls of the quasi-2D channel were cooled by air jets impinging on the wall. This allowed for a maximum temperature rise of  $40^{\circ}\text{C}$ . A part of the lower channel wall was replaced by a ceramic tile. The ceramic tile was followed by a backward facing step, which leads to the combustion chamber. The flame was first stabilized at the backward facing step downstream of the ceramic tile. When increasing the equivalence ratio, the low thermal conductivity of the ceramic tile allows for upstream flame propagation up to the upstream edge of the ceramic tile. After flame stabilization at the upstream edge of the ceramic tile, the equivalence ratio was increased until flame propagation on the cold steel wall was initiated. Upstream flame propagation was considered flashback when the flame reached the inlet of the measurement section or at least did not reattach to the ceramic tile.

The computational domain of the confined simulations is depicted in Figure 5.1. This domain resembles the rectangular channel from the experiments of Eichler et al. [34]. The channel half height  $\delta = 8.75\text{ mm}$  is similar to the experimental channel half height. For bulk velocities up to  $10\text{ m s}^{-1}$ , the channel width is  $3\delta$ . For a bulk velocity of  $20\text{ m s}^{-1}$ , the channel width is reduced to

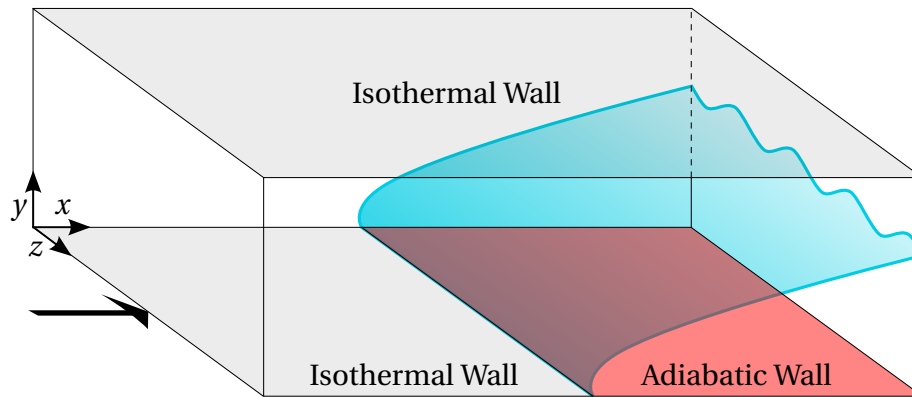


**Figure 5.1:** Computational domain and expected confined stable flame shape. The black arrow indicates the flow direction. The expected stable flame is outlined in blue.

$2.29\delta$  in order to reduce computational costs.

The quasi-2D character of the experimental channel flow is represented by applying cyclic boundary conditions at the  $z$ -normal front and back patches. The lower channel wall is an isothermal wall up to  $x \leq 3\delta$  and an adiabatic wall for  $x > 3\delta$ . This represents the cooled stainless steel wall and the ceramic tile of the experimental setup. The inlet gas temperature and the isothermal wall temperature is set to 293.15 K. An unsteady velocity field is prescribed at the inlet. The unsteady velocity field is sampled at the outlet of the inert simulations and mapped to the inlet of the reactive simulations. The equivalence ratio of the gas mixture is adjusted by prescribing the species mass fractions of hydrogen, oxygen and nitrogen at the inlet. Air is assumed to have a molar composition of 79 % nitrogen and 21 % oxygen. A zero gradient boundary condition is prescribed for velocity, temperature and species mass fractions at the outlet. The fluid dynamic pressure has a Dirichlet boundary condition at the outlet and a zero gradient boundary condition at the inlet.

The base resolution of the computational domain is at first not changed compared to the inert simulations. The inert computational grid is however too coarse to resolve the flame front. Adaptive mesh refinement is therefore incorporated in the reactive solver. The adaptive mesh refinement algorithm is native to OpenFOAM. It splits the edges of a hexahedral cell in half. One cell split

thus creates eight smaller hexahedral cells. Here, cells are refined when they are located within the flame. The consumption of hydrogen in a cell is used as an indicator whether the cell is located within the flame. A cell is marked for refinement when 10% of the unburnt hydrogen mass fraction is consumed in the cell. The hydrogen consumption  $\Delta H_2$  in a cell is calculated from the gradient of hydrogen mass fraction and the cube root of the cell volume,

$$\Delta H_2 = |\nabla Y_{H_2}| V_c^{1/3}. \quad (5.1)$$

The number of applied cell splits depends on the base grid of the simulation and on the flame thickness. For each case, the number of cell splits is adapted so that the flame front is sufficiently resolved. Due to limited computational resources, a full mesh study is not feasible. The resolution of the flame front is therefore assessed a posteriori by means of the SGS combustion regime and resolution criteria from literature.

### 5.1.2 Procedure for Confined Flashback Simulations

The flashback simulations are started at equivalence ratios for which no flashback is expected to occur. For each bulk velocity, the simulations are initialized with a constant velocity. Combustion is initiated in the adiabatic section by a rectangular zone of burnt gas with a height of 1 mm. Here, hydrogen, oxygen and water mass fractions as well as temperature are set to equilibrium values. The equilibrium values are obtained from Cantera simulations [53]. In the beginning of each simulation, the flame is wrinkled by thermal-diffusive and hydrodynamic instabilities. Flame wrinkling is enhanced as soon as the unsteady velocity fluctuation prescribed at the inlet reaches the flame front. After full development of flame wrinkling, the flame front is stabilized at the upstream edge of the adiabatic lower wall. The equivalence ratio is then increased by small steps of 0.02 to 0.05. This procedure is repeated until the flame propagates into the isothermal channel section and can no longer be washed out. The corresponding equivalence ratio is defined as the flashback equivalence ratio  $\Phi_{FB}$ .

## 5.2 Confined Flashback at Atmospheric Pressure

Flashback at atmospheric pressure is investigated at all bulk velocities from  $6 \text{ ms}^{-1}$  to  $30 \text{ ms}^{-1}$ . As the inert base mesh is very coarse at  $U_b = 6 \text{ ms}^{-1}$ , the inert mesh is refined in x-direction by increasing the cell count  $N_x$  by a factor of 1.5. In addition, two adaptive cell splits are applied at  $U_b = 6 \text{ ms}^{-1}$ . At  $U_b = 10 \text{ ms}^{-1}$ , only one cell split is applied by adaptive mesh refinement. At higher bulk velocities, higher flashback equivalence ratios are expected. This is accompanied by lower flame thicknesses. At  $U_b = 20 \text{ ms}^{-1}$  and  $U_b = 30 \text{ ms}^{-1}$ , two cell splits are therefore applied.

### 5.2.1 Confined Boundary Layer Flashback Process

At a bulk velocity of  $6 \text{ ms}^{-1}$ , the flame is stable up to an equivalence ratio of 0.33. The stable flame front at this equivalence ratio is depicted in Figure 5.2 (a). The flame front is wrinkled due to intrinsic instabilities and the velocity fluctuations of the turbulent channel flow. Flame bulges are formed but the flame front is still stabilized at the upstream edge of the adiabatic wall section. Eichler and Sattelmayer [35] observed that the flame backpressure even causes boundary layer separation at stable equivalence ratios. This can also be seen in Figure 5.2 (a) for confined turbulent flames. Although backflow regions are already present at  $\Phi = 0.33$ , flame quenching at the isothermal wall prevents upstream flame propagation. Propagating flame tongues are thus not formed at  $U_b = 6 \text{ ms}^{-1}$  and  $\Phi = 0.33$ . When increasing the equivalence ratio to 0.36, the reactivity of the gas mixture is increased and the flame is capable of propagating on the isothermal channel wall. The flame is not washed out of the isothermal channel section and flashback occurs. This propagating flame front at  $\Phi = 0.36$  is depicted in Figure 5.2 (b).

At  $U_b = 10 \text{ ms}^{-1}$ , the flashback process is similar to the flashback process at  $U_b = 6 \text{ ms}^{-1}$ . The flame is fully stable up to an equivalence ratio of 0.38 and flashback is first observed at  $\Phi = 0.4$ . At a bulk velocity of  $20 \text{ ms}^{-1}$ , a stable flame is observed up to  $\Phi = 0.55$ . The temporal evolution of the flame front at  $U_b = 20 \text{ ms}^{-1}$  and  $\Phi = 0.55$  is depicted in Figure 5.3 together with the axial

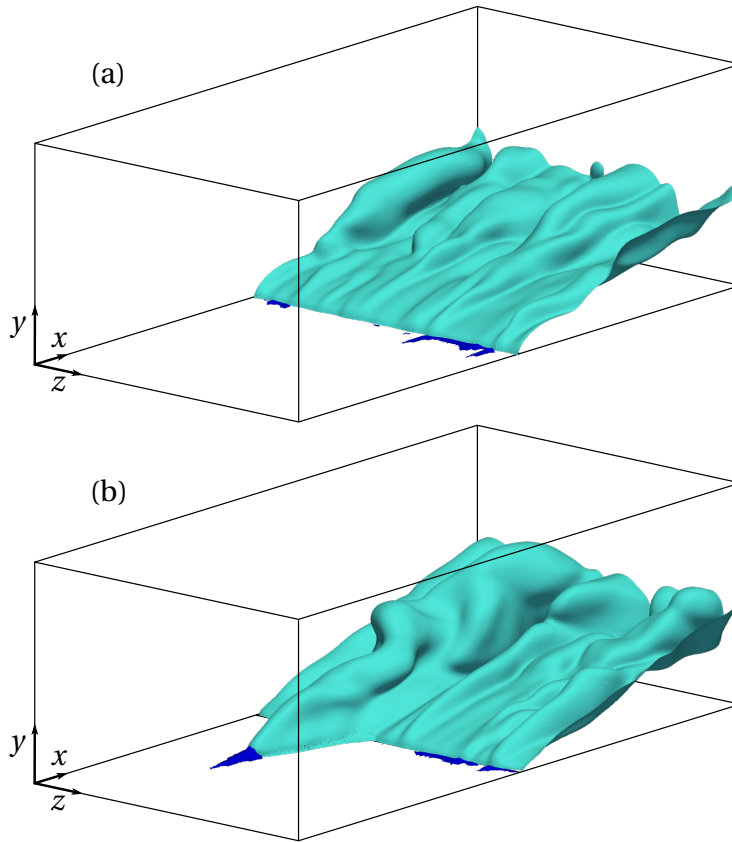


**Figure 5.2:** Stable flame front and flashback at  $U_b = 6 \text{ m s}^{-1}$ . The flame front is depicted by the light blue  $c = 0.5$  isosurface for (a) the stable flame at  $\Phi = 0.33$  and (b) flashback at  $\Phi = 0.36$ . The dark blue isosurface at  $u_x = 0$  shows the separation zone.

velocity field and the separation zones ahead of the flame. In contrast to the flames at  $U_b = 6 \text{ m s}^{-1}$  and  $U_b = 10 \text{ m s}^{-1}$ , formation and propagation of flame tongues already occurs at this stable equivalence ratio. At  $t = 0 \text{ ms}$ , the flame is stabilized at the upstream edge of the adiabatic lower wall section. Local flow separation zones at flame bulges are already present over the whole channel width. A large flow separation zone is formed in the low velocity streak at the center of the channel. This separation zone facilitates the formation of a propagating flame tongue. The subsequent images show that this separation zone and the foremost flame cusp both propagate upstream along a streak of low axial velocity. At  $t = 2.0 \text{ ms}$ , the axial velocity ahead of the flow separation zone increases. As soon as the high axial velocity reaches the separation zone

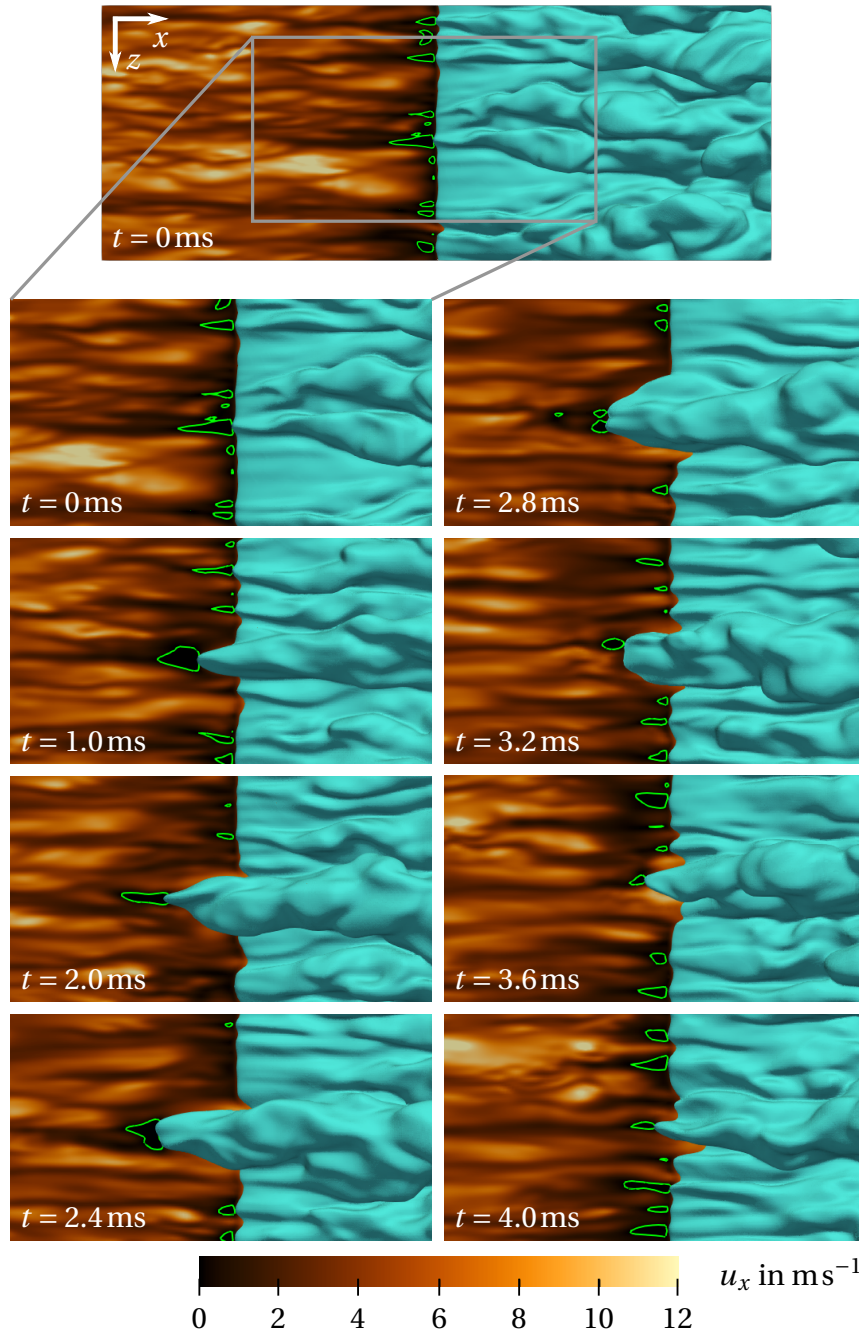


**Figure 5.3:** Top view of upstream flame propagation at  $U_b = 20 \text{ ms}^{-1}$  and  $\Phi = 0.55$ . The flame front is shown by the blue  $c = 0.5$  isosurface. The streamwise velocity  $u_x$  is plotted on a  $y$ -normal plane with a wall distance of  $0.1 \text{ mm}$ . The green isolines at  $u_x = 0$  represent the back-flow regions on the same plane.

at  $t = 2.4$  ms, the separation zone and the flame cusp are widened. This is followed by a significant reduction of the separation zone size and to the initiation of flame washout at  $t = 2.8$  ms. When the axial velocity ahead of the flame tongue is further increased at  $t = 3.2$  ms, the flame tongue is pushed further downstream while a part of the widened flame tongue still causes boundary layer separation in a thin low velocity turbulence streak. Despite a persisting separation zone ahead of the flame tongue, the flame is washed out in the following time steps and no flashback occurs.

At  $U_b = 20 \text{ ms}^{-1}$ , flashback is first observed at  $\Phi = 0.6$ . The temporal evolution of the flame front at  $\Phi = 0.6$  is depicted in Figure 5.4. The initiation of flame propagation at  $\Phi = 0.6$  is similar to the lower equivalence ratio case in Figure 5.3. The flame continuously propagates upstream up to  $t = 2.4$  ms. The higher equivalence ratio however leads to a higher flame speed and a lower quenching thickness. This allows the flame to propagate further upstream than at  $\Phi = 0.55$ . Starting from  $t = 2.4$  ms, the flame tongue is pushed downstream by a zone of high axial velocity. The higher reactivity of the gas mixture however prevents full washout of the flame tongue. At  $t = 4.0$  ms, the flame is still located in the isothermal channel section. The separation zone ahead of the flame tongue has reappeared and upstream flame propagation is reinitiated.

The comparison of the propagation behaviour of flames in Figures 5.3 and 5.4 confirms some findings of Eichler [36]. It is apparent that flame flashback is initiated by the occurrence of a separation zone ahead of the flame front. Flame propagation does however not occur in every separation zone. The smaller separation zones at  $t = 0$  ms do not lead to the formation of a propagating flame tongue. Instead, only the separation zone in the center of the channel is large enough to promote flame propagation. Furthermore, it is evident that flame flashback at  $U_b = 20 \text{ ms}^{-1}$  is characterized by alternating periods of upstream flame propagation and flame washout. Whether or not flashback occurs is determined by the propagation velocity of the flame tongue. BLF occurs if the propagation distance during upstream flame propagation is larger than the negative propagation distance during flame washout. Eichler furthermore observed that flame flashback is accompanied by the formation of new flame cusps. This can also be seen in Figure 5.4. While the fore-

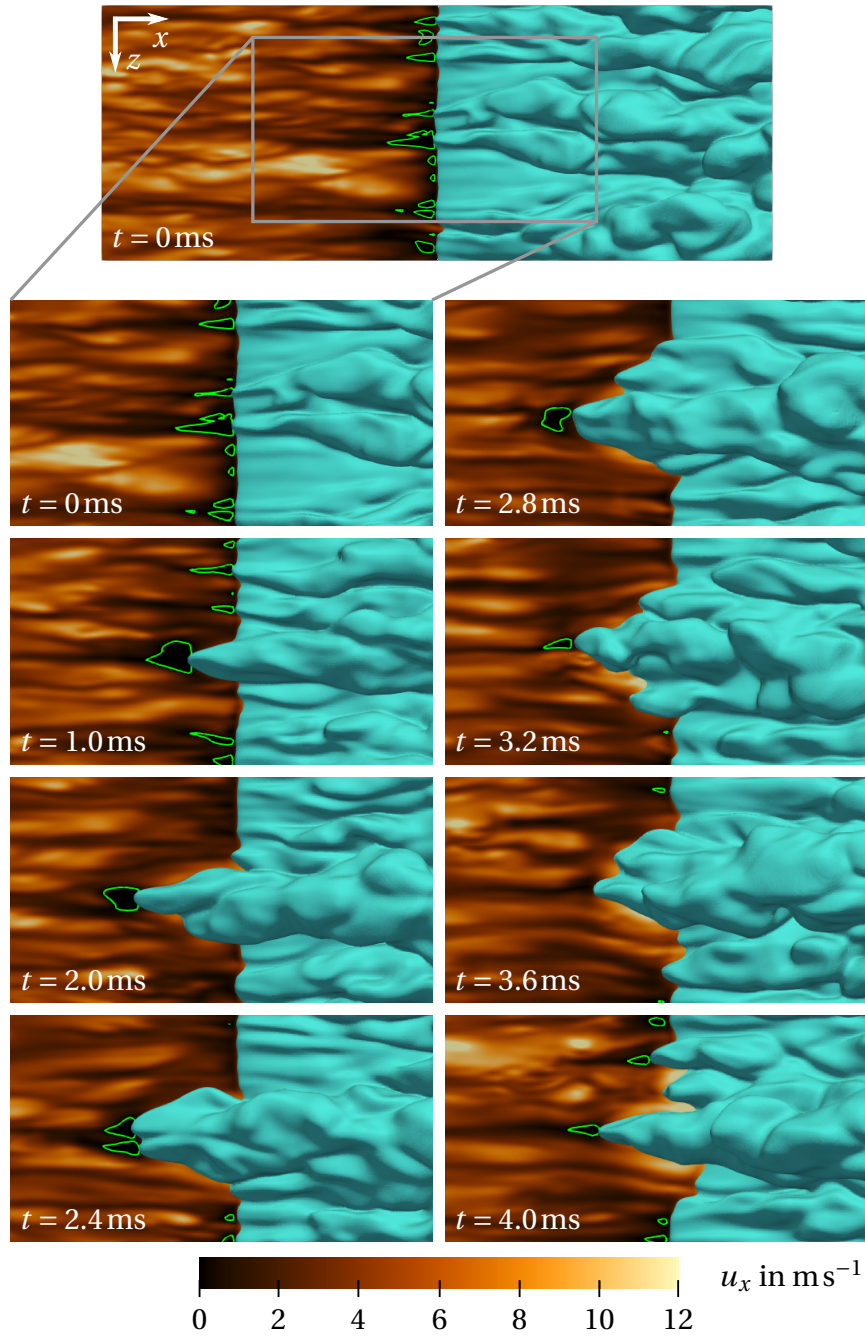


**Figure 5.4:** Top view of upstream flame propagation at  $U_b = 20 \text{ ms}^{-1}$  and  $\Phi = 0.60$ . Similar to Figure 5.3.

most cusp is pushed downstream by high axial velocities, low axial velocity streaks and intrinsic combustion instabilities induce new cusps at the lateral edges of the flame tongue. At  $t = 4.0$  ms one of the newly formed cusps induces boundary layer separation. This shows the potential of newly formed cusps to contribute to the net upstream flame propagation as observed by Eichler [36].

The formation of one single flame tongue at the beginning of flame propagation observed in the present work is different to the onset of flashback in previous simulations of Gruber et al. [57] or Lietz et al. [100]. In their simulations, flashback was initiated by the formation and propagation of alternating convex and concave flame bulges along the whole flame front. The isothermal boundary condition in the present work prevents the propagation of these flame bulges. Instead, flame propagation is initiated locally when a low axial velocity streak increases the local separation zone size so that a flame tongue can form and propagate upstream.

### 5.2.2 Confined Boundary Layer Flashback Limits at Atmospheric Pressure

As indicated in the previous section, confined BLF is first observed at equivalence ratios of 0.36, 0.4 and 0.6 at bulk velocities of  $6 \text{ ms}^{-1}$ ,  $10 \text{ ms}^{-1}$  and  $20 \text{ ms}^{-1}$ , respectively. The flames are stable up to equivalence ratios of 0.33, 0.38 and 0.55 at bulk velocities of  $6 \text{ ms}^{-1}$ ,  $10 \text{ ms}^{-1}$  and  $20 \text{ ms}^{-1}$ , respectively. At a bulk velocity of  $30 \text{ ms}^{-1}$ , the flame is stable up to an equivalence ratio of 0.7 and flashback is first observed at an equivalence ratio of 0.75. In Figure 5.5, these numerical flashback limits are compared to experimental flashback limits obtained by Eichler [36].

According to the experimental data, flashback is expected to occur approximately at an equivalence ratio of 0.71 for  $U_b = 30 \text{ ms}^{-1}$ . At  $U_b = 20 \text{ ms}^{-1}$ , flashback is expected to occur at an equivalence ratio between 0.52 and 0.55. The experimental flashback limit for  $U_b = 10 \text{ ms}^{-1}$  lies between  $\Phi = 0.33$  and  $\Phi = 0.35$ . At bulk velocities higher than  $U_b = 10 \text{ ms}^{-1}$ , the confined BLF limits are predicted accurately by the numerical simulations. At  $U_b = 6 \text{ ms}^{-1}$ , flashback is however expected at an equivalence ratio of  $\Phi \approx 0.28$ . The flashback tendency at lower bulk velocities and equivalence ratios is thus slightly un-

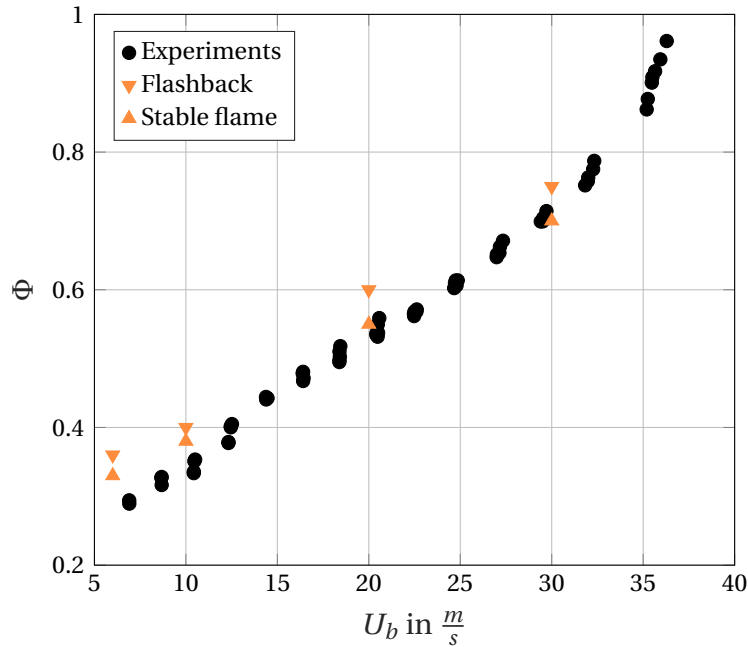


**Figure 5.5:** Confined boundary layer flashback limits at atmospheric pressure compared to experimental flashback limits obtained by Eichler [36].

derestimated by the numerical simulations.

Thermal-diffusive instabilities enhance flame propagation at very low equivalence ratios [148]. It appears that the effect of the thermal-diffusive instabilities is slightly underestimated in the current simulations. Nevertheless, the qualitative trend of the experimental flashback limits is reproduced by the numerical simulations. The model is furthermore capable of approximately reproducing the experimental flashback limits in a quantitative manner. This shows that all physical phenomena, which are relevant for numerically modelling boundary layer flashback, are included in the numerical model.

### 5.2.3 Validity of the Results

The comparison of numerical and experimental flashback limits shows that the numerical model is capable of quantitatively reproducing experimentally obtained flashback limits. The validity of the results can be strengthened by

assuring mesh convergence of the results and the applicability of the quasi-laminar combustion model.

It was established in Chapter 3.5 that the quasi-laminar combustion model is valid when all cells lie within the wrinkled flamelet, laminar flamelet and the DNS combustion regime for LES. Figure 5.6 shows the combustion regimes of all atmospheric cases at flashback conditions. Each data point represents one cell along the y-axis of the base mesh. The Karlovitz number is independent of the LES filter width [118]. The Karlovitz number can therefore be calculated from the turbulent velocity fluctuations and filter width of the inert simulations presented in Chapter 4.2.1.1. The resolution  $\Delta/l_f$  of the flame front on the other hand has to be calculated from the refined LES filter width. The laminar flame speed in  $\text{m s}^{-1}$  is approximated by the correlation

$$\begin{aligned}
 s_{l,0} = & -1.55236 \times 10^{-9} X_{H_2}^6 + 3.49519 \times 10^{-7} X_{H_2}^5 - 2.82975 \times 10^{-5} X_{H_2}^4 \\
 & + 9.35840 \times 10^{-4} X_{H_2}^3 - 9.97510 \times 10^{-3} X_{H_2}^2 + 5.00120 \times 10^{-2} X_{H_2} \\
 & - 8.32830 \times 10^{-2}
 \end{aligned} \quad (5.2)$$

developed by Böck [8]. The mixture diffusivity  $D$  is calculated from the Lewis number definition (2.3) and the mixture thermal diffusivity  $\alpha$  obtained from Cantera. All parameters used for the Karlovitz number and flame length scale calculation are listed in Table 5.1.

**Table 5.1:** Parameters for the atmospheric combustion regime analysis.

$\Phi$	$T_{ad}$ in K	$s_{l,0}$ in $\text{m s}^{-1}$	$\alpha$ in $\text{m}^2 \text{s}^{-1}$	$\nu$ in $\text{m}^2 \text{s}^{-1}$	Le	$D$ in $\text{m}^2 \text{s}^{-1}$
0.36	1329.3	0.26	3.151e-05	1.732e-05	0.380	8.297e-05
0.4	1422.3	0.35	3.248e-05	1.754e-05	0.394	8.246e-05
0.6	1838.6	0.92	3.698e-05	1.864e-05	0.484	7.640e-05
0.75	2096.8	1.40	4.003e-05	1.944e-05	0.572	7.000e-05

It is clear from Figure 5.6 that all data points at bulk velocities up to  $20 \text{ m s}^{-1}$  lie within the laminar flamelet or DNS regimes. The filter width is smaller than the Kolmogorov scale and the SGS flame structure is laminar. Some cells at  $U_b = 30 \text{ m s}^{-1}$  lie within the thin reaction zone regime. The SGS eddies are thus small enough to penetrate the preheat zone and enhance scalar mixing [117].

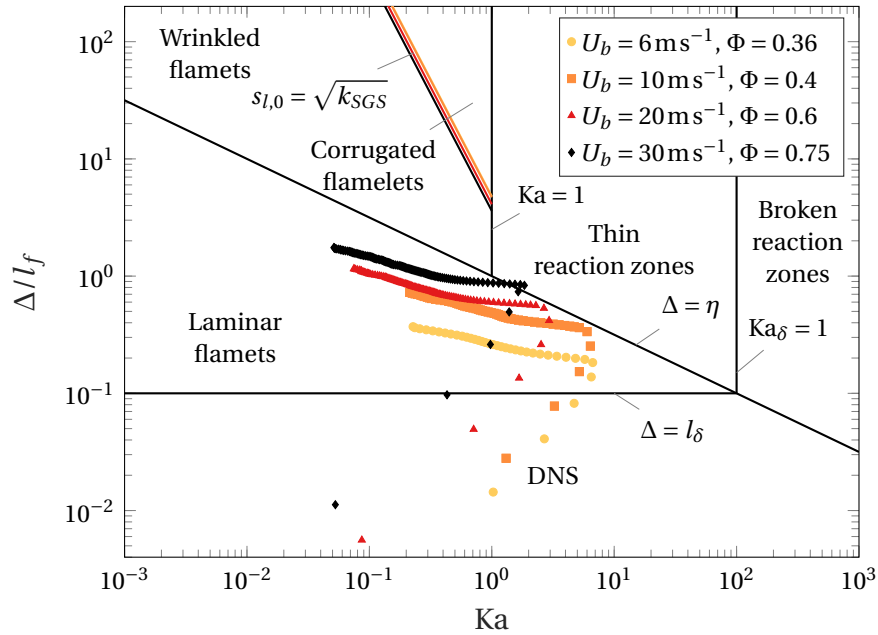


**Figure 5.6:** LES combustion regimes at atmospheric pressure.

Formally, the quasi-laminar combustion model is not valid in this case. However, only four cells lie within the thin reaction zone regime. Neglecting the influence of SGS fluctuations on the mixing processes is therefore expected to only have a minor effect on the overall combustion process. With the current refinement strategy, the quasi-laminar combustion model is therefore expected to deliver accurate results for all confined BLF simulations at atmospheric pressure.

Mesh convergence is commonly studied by refining the computational mesh until the results do not change with further mesh refinement. Unfortunately, the LES presented in this work are too computationally costly to perform an extensive mesh convergence study for every case under investigation. Instead, the mesh convergence shall only be investigated for  $U_b = 10 \text{ m s}^{-1}$ . All other cases have to be assessed by means of flame resolution. Duwig et al. [32] identified that the flame front should be resolved by 3 to 5 cells for obtaining good results with thickened flame combustion models. No flame thickening is thus necessary when the flame front is already resolved by at least three cells. The resolution of the flame front by three cells is therefore presumably also the minimum resolution for LES with the quasi-laminar combustion model.

Thermal-diffusive instabilities, flame quenching and turbulence have an influence on flame thickness. The actual LES flame thickness is therefore not equal to the laminar flame thickness. With the temperature gradient  $\partial T/\partial x_i$ , the LES flame thickness  $\delta_f$  can be obtained from the LES results [119]:

$$\delta_f = \frac{T_{ad} - T_u}{\max\left(\left|\frac{\partial T}{\partial x_i}\right|\right)}. \quad (5.3)$$

This local flame thickness can be used in order to obtain average flame thickness profiles. The temperature gradient is therefore sampled on isosurfaces of the reaction progress variable

$$c = \frac{Y_{H_2,u} - Y_{H_2}}{Y_{H_2,u}}. \quad (5.4)$$

For each case, 19 isosurfaces between  $c = 0.05$  and  $c = 0.95$  are evaluated from at least 27 time steps. A wall-normal flame thickness profile is obtained for each of the 19 isosurfaces by averaging the sampled temperature gradient in spanwise direction and in time. The minimum envelope of all 19 isosurfaces results in the minimum flame thickness profiles relevant for the flame resolution evaluation. These minimum flame thickness profiles at atmospheric flashback conditions are depicted in Figure 5.7. Although the equivalence ratio of the flame thickness profiles varies between 0.36 and 0.75, the order of magnitude of the flame thickness is similar for all atmospheric cases. This underlines the influence of thermal-diffusive effects on flame structure.

A minimum flame resolution can be obtained from the minimum average flame thickness profiles in Figure 5.7. Here, the resolution of the flame front is defined as the minimum average flame thickness divided by the cube root of the cell volume. This results in minimum flame resolution of 4.4, 3.6, 5.1 and 5.4 for the flashback cases at bulk velocities of  $6 \text{ ms}^{-1}$ ,  $10 \text{ ms}^{-1}$ ,  $20 \text{ ms}^{-1}$  and  $30 \text{ ms}^{-1}$ , respectively. All atmospheric cases thus fulfill the resolution criterion of three cells per flame thickness.

The  $10 \text{ ms}^{-1}$  case with one cell split shows the lowest flame resolution of 3.6 cells per flame thickness. This resolution is close to the resolution criterion of three cells per flame thickness. This makes the atmospheric case

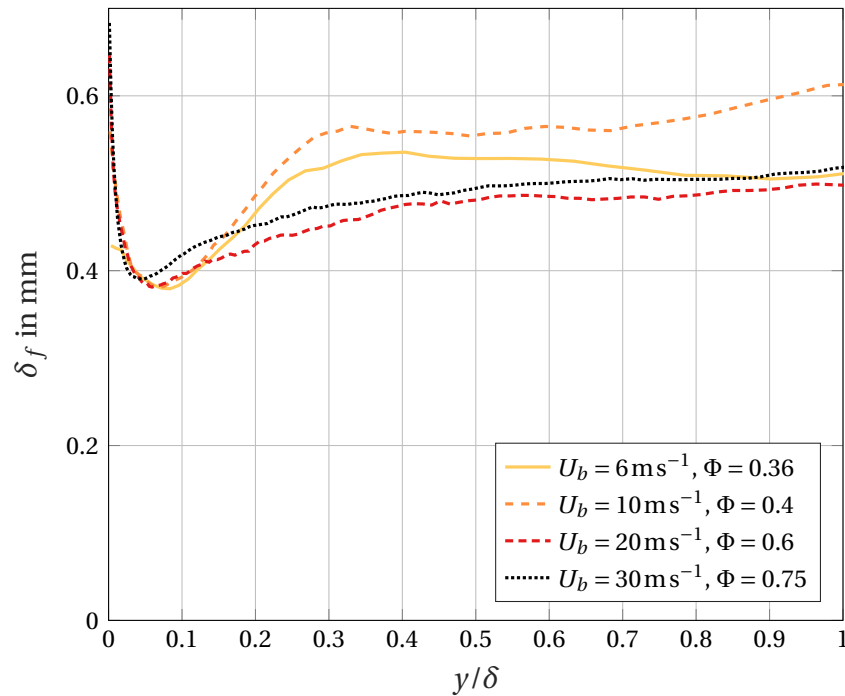


**Figure 5.7:** Atmospheric flame thickness profiles at flashback conditions

at  $U_b = 10 \text{ ms}^{-1}$  ideal for investigating the validity of the resolution criterion. Additional simulations with two cell splits are therefore conducted for  $U_b = 10 \text{ ms}^{-1}$ . Figure 5.8 shows the average flame shape at  $U_b = 10 \text{ ms}^{-1}$  and  $\Phi = 0.38$  with one cell split compared to the same equivalence ratio with two cell splits. The average flame shapes are obtained by averaging the hydrogen mass fraction in time and in spanwise direction. Figure 5.8 shows that the average flame shape is largely unaffected by the additional cell split. The flashback limit also does not change with the additional cell split. This shows that a flame resolution of 3.6 cells per flame thickness is sufficient for predicting the average flame shape and the flashback limit accurately. A minimum flame resolution of approximately 3 cells is thus confirmed as a good resolution limit for the reactive LES.

#### 5.2.4 Influence of Molecular Diffusion on Hydrogen Combustion

It was postulated in Chapter 2.4 that differential diffusion, non-equi diffusion and Soret diffusion are essential for accurately modelling boundary layer

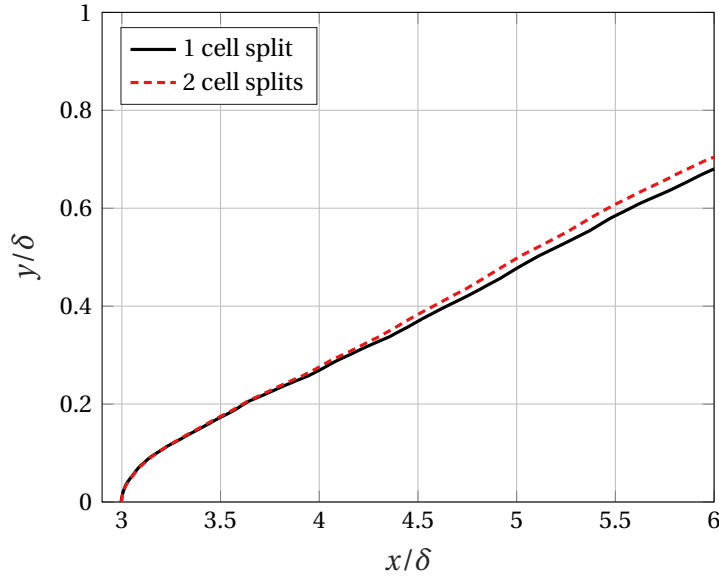


**Figure 5.8:** Average stable flame shape at  $U_b = 10 \text{ ms}^{-1}$  and  $\Phi = 0.38$  with one and two cell splits. The average flame shape is represented by the  $\bar{c} = 0.5$  isoline.

flashback of hydrogen-air flames. The influence of these diffusion effects shall therefore be investigated on the basis of the stable atmospheric flame at  $U_b = 10 \text{ ms}^{-1}$  and  $\Phi = 0.38$ .

Grcar, Bell and Day [56] found that thermal-diffusive effects lead to higher effective equivalence ratios in hydrogen-air flames. This was shown by means of the joint probability density function (JPDF) of the hydrogen molar fraction and temperature in a two-dimensional lean hydrogen-air flame. A similar JPDF of hydrogen mass fraction and temperature is depicted in Figure 5.9. The JPDF is obtained from 100 hydrogen mass fraction probability density functions (PDF) evaluated at 100 temperature windows between the minimum and maximum temperature of one time step. Each PDF is normalized by its maximum value. This approach is similar to the approach in [56]. Figure 5.9 (a) shows the JPDF for the stable atmospheric flame at  $U_b = 10 \text{ ms}^{-1}$  and  $\Phi = 0.38$  when all diffusion terms from Equation (3.53) are incorporated in the solver. This JPDF is compared to the laminar planar flames at  $\Phi = 0.38$  and  $\Phi = 0.5$  obtained from Cantera simulations. It is evident that the local hydrogen mass fraction distribution of the turbulent three dimensional flame

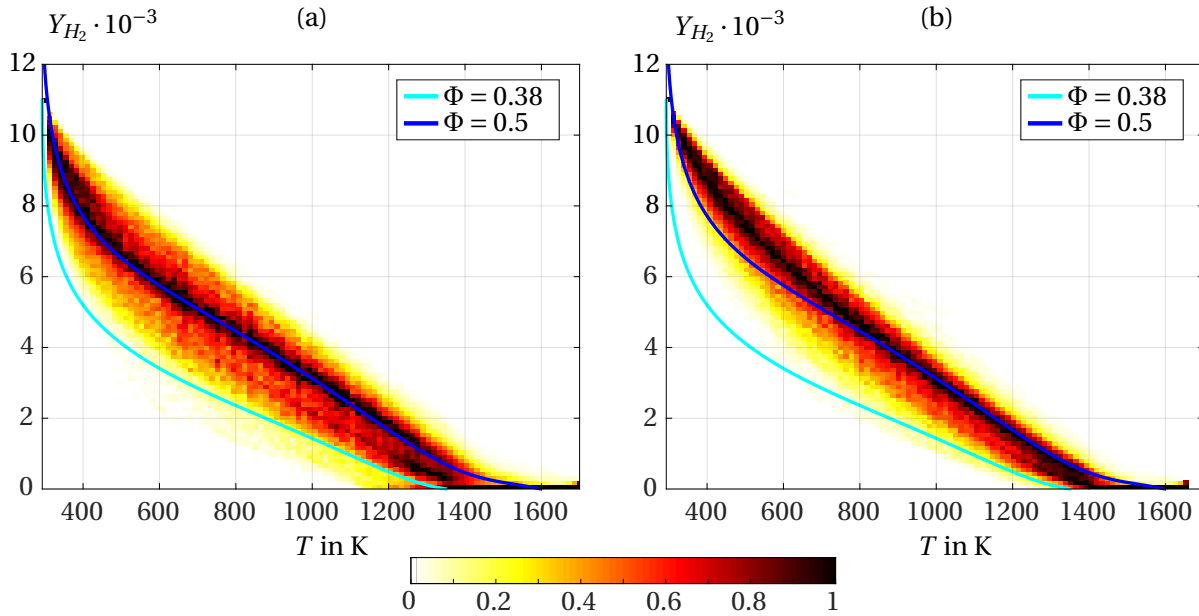


**Figure 5.9:** JPDF of hydrogen mass fraction and temperature at  $U_b = 10 \text{ m s}^{-1}$  and  $\Phi = 0.38$  (a) with Soret effect, (b) without Soret effect. The superimposed lines represent planar laminar flames at  $\Phi = 0.38$  and  $\Phi = 0.5$

at  $\Phi = 0.38$  differs significantly from the laminar hydrogen distribution. The location of the JPDF maximum is very similar to the laminar hydrogen distribution at  $\Phi = 0.5$ . This confirms that thermal-diffusive instabilities lead to an increased effective equivalence ratio  $\Phi_{eff}$  compared to the actual equivalence ratio of  $\Phi = 0.38$ .

The importance of a detailed diffusion model for the flashback simulations is confirmed by a simulation at  $U_b = 10 \text{ m s}^{-1}$  and  $\Phi = 0.38$  without any differential diffusion terms and without non-equi diffusion. Here, Soret diffusion is neglected and the molecular diffusion coefficient is approximated by the effective viscosity ( $\nu + \nu_{SGS}$ ). This is the standard approach implemented in the OpenFOAM combustion solver reactingFoam. This modification of the diffusion model in the combustion solver results in full flame washout. Although the equivalence is very close to flashback conditions, the flame at  $\Phi = 0.38$  is not stabilized by the adiabatic wall.

In addition to the general effect of differential diffusion on lean premixed

hydrogen-air flames, Grcar, Bell and Day [56] investigated the effect of Soret diffusion and of the diffusion model formulation on two-dimensional flames. Therefore, they compared results of a full multicomponent diffusion model including Soret diffusion with results of a mixture averaged diffusion model without Soret diffusion. From this comparison, they concluded that the multicomponent diffusion model and the Soret effect both increase the effective equivalence ratio compared to the mixture averaged model without Soret diffusion. Figure 5.9 (b) shows the JPDF of the current simulation at  $U_b = 10 \text{ m s}^{-1}$  and  $\Phi = 0.38$  when no Soret diffusion is included in the model. In contrast to the work of Grcar, Bell and Day [56], both diffusion models with and without Soret diffusion are mixture averaged diffusion models in the current work. Comparing Figures 5.9 (a) and (b) shows that the effective equivalence ratio drops when Soret diffusion is included in the simulation. The increased effective equivalence ratio observed by Grcar, Bell and Day is thus most likely caused by the multicomponent diffusion model and not by Soret diffusion. The influence of Soret diffusion on the overall combustion characteristics is therefore not clear from the analysis of Grcar, Bell and Day.

Figure 5.10 shows the influence of the Soret effect on the average flame shape and on the turbulent flame speed  $s_t$  at  $U_b = 10 \text{ m s}^{-1}$  and  $\Phi = 0.38$ . When including Soret diffusion in the simulations, the average flame shape is steeper compared to the simulation without Soret diffusion. This indicates that the Soret effect has an influence on the turbulent flame speed. The turbulent flame speed in Figure 5.10 is defined as the average fresh gas velocity component normal to the flame front [117]. In practice, it is not possible to evaluate the fresh gas velocity at a  $\bar{c} = 0$  isoline. The gas velocity at the flame front is therefore evaluated at the  $\bar{c} = 0.05$  isoline of the average flame front. The gas velocity at  $\bar{c} = 0.05$  is corrected by the factor  $T_u/\bar{T}$  in order to take account of the temperature rise from  $T_u$  to the flame temperature  $\bar{T}$  at  $\bar{c} = 0.05$ . The turbulent flame speed obtained with this method strongly depends on the value of  $\bar{c}$  chosen for the evaluation [119, 138]. The turbulent flame speeds in Figure 5.10 are therefore normalized by the maximum turbulent flame speed when including Soret diffusion. Neglecting the Soret effect reduces the maximum turbulent flame speed by 13 % at  $U_b = 10 \text{ m s}^{-1}$  and  $\Phi = 0.38$ . The Soret effect thus significantly increases the turbulent flame speed. This contradicts

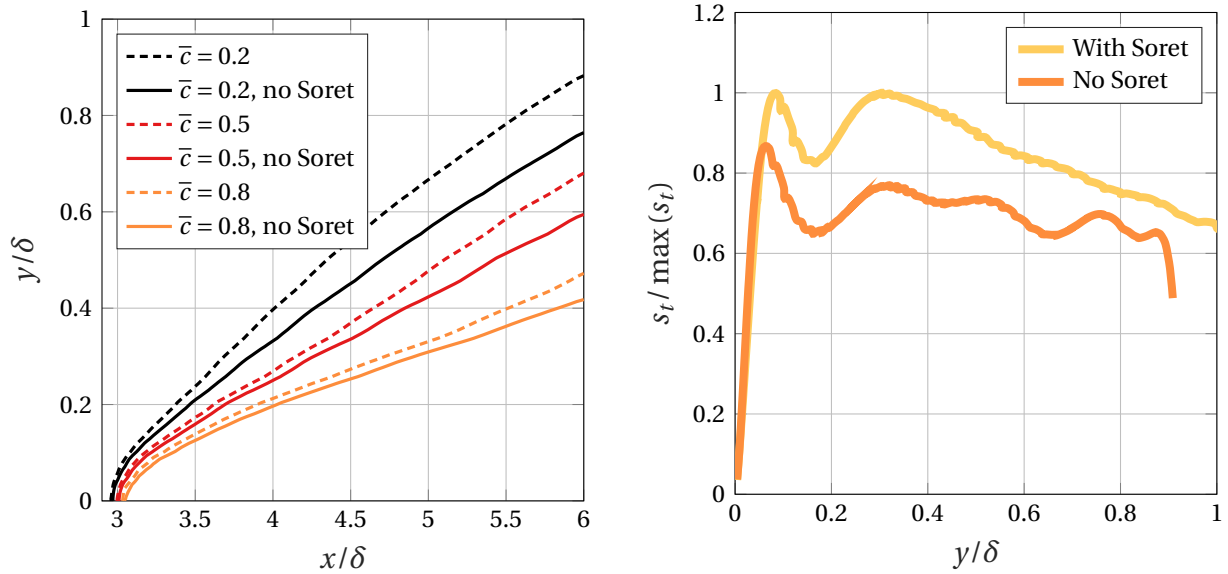


**Figure 5.10:** Influence of Soret diffusion on the average flame shape and turbulent flame speed at  $U_b = 10 \text{ m s}^{-1}$  and  $\Phi = 0.38$ .

the previous observation that the Soret effect decreases the local equivalence ratio, which should decrease the turbulent flame speed.

The Soret effect increases the diffusion of light molecules such as the O, H and OH radicals as well as the  $\text{H}_2$  molecule towards regions of high temperatures [40]. This decreases the hydrogen mass fraction in lower temperature regions, which was observed in Figure 5.9. Furthermore, Ern and Giovangigli [40] observed that the Soret effect decreases the flame speed and radical concentrations in low temperature regions. The medians of the JPDF of hydrogen reaction rate  $\dot{\omega}_{\text{H}_2}$  and temperature  $T$  with and without Soret diffusion are plotted in Figure 5.11. Furthermore, Figure 5.11 shows the medians of the JPDF of the H radical mass fraction  $Y_{\text{H}}$  and temperature  $T$  with and without Soret diffusion. The corresponding JPDFs are obtained with a similar approach as the JPDF in Figure 5.9. The median H radical mass fraction in Figure 5.11 is higher throughout the flame when including Soret diffusion. The Soret effect does not decrease the radical concentrations in low temperature regions, as indicated by Ern and Giovangigli [40]. Instead, higher hydrogen and radical diffusion fluxes towards higher temperatures increase the radical concentrations in low and high temperature regions. This leads to higher fuel consumption

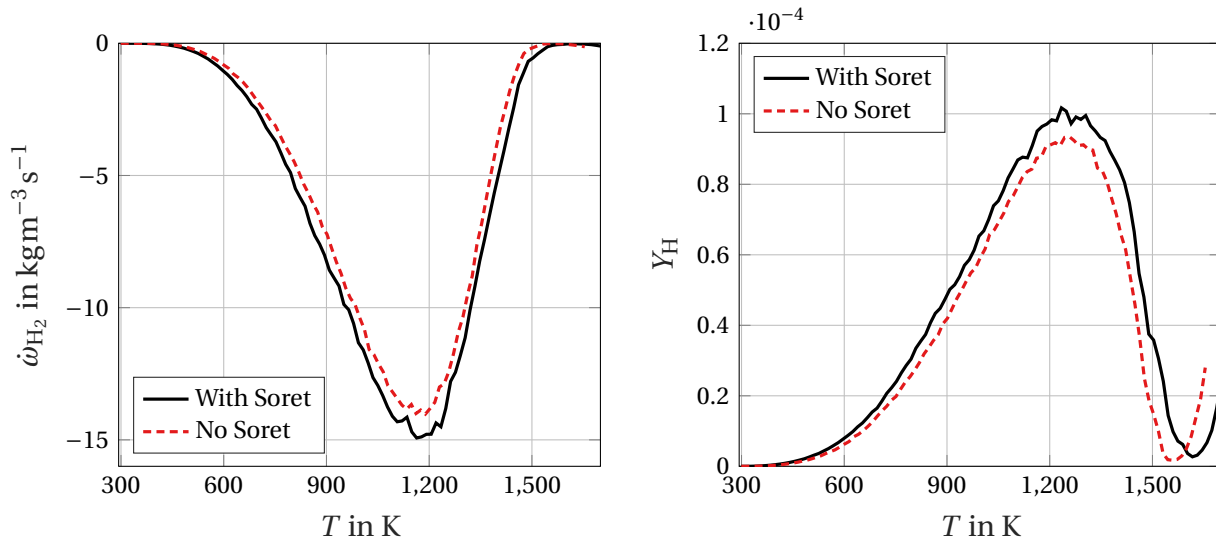


**Figure 5.11:** Median of the JPDFs of hydrogen reaction rate and temperature and of  $Y_H$  and temperature with and without Soret diffusion. For  $U_b = 10 \text{ m s}^{-1}$  and  $\Phi = 0.38$ .

rates as seen in Figure 5.11. Ultimately, the turbulent flame speed is increased by Soret diffusion.

The analysis of stable atmospheric results with different diffusion models shows that differential diffusion, non-equi diffusion and the Soret effect are highly relevant for modelling flashback of lean hydrogen-air flames. Without differential diffusion and non-equi diffusion, the flame speed is underestimated and the flame is washed out by the approaching flow. Including Soret diffusion in the simulations on the other hand modifies the species distribution across the flame front and leads to higher fuel consumption rates and turbulent flame speeds. Furthermore, the comparison with results of Grcar, Bell and Day [56] shows that the full multicomponent diffusion model might lead to higher effective equivalence ratio compared to the mixture averaged diffusion model. This could explain the discrepancy between the numerical flashback limits and the experimental flashback limits at low equivalence ratios observed in Chapter 5.2.2.

### 5.2.5 Inert Channel Size Influence on Flashback Results

It was noted in Chapter 4.2.2, that the inert channel at bulk velocities of  $10 \text{ ms}^{-1}$  and higher is according to Chin et al. [16] not long enough to accommodate the full length of the turbulence structures. This can lead to an artificial elongation of the turbulence structures, which can in turn have an influence on the flashback behaviour. The influence of the inert channel size on the reactive flashback results thus has to be assessed. The reactive simulations at  $U_b = 10 \text{ ms}^{-1}$  are therefore repeated with the inert base flow from the  $L = 25.2\delta$  channel. With this modified inert base flow, flame flashback occurs at an equivalence ratio of 0.42 compared to the original flashback equivalence ratio of 0.4 for the  $L = 6\delta$  channel. The flashback tendency thus drops when applying an inert base flow from a larger channel. This confirms that the inert channel size has an influence on the turbulence structures. However, the influence on the flashback limits is limited as the flashback equivalence ratio only increases by 5.0 %.

The limited influence of the inert velocity profile on the combustion characteristics is confirmed when comparing the turbulent flame speeds obtained with different inert velocity profiles. With the new inert velocity profile from the larger inert channel, the flame is fully stable up to an equivalence ratio of 0.4 compared to the previously observed stable equivalence ratio of 0.38. The higher stable equivalence ratio only increases the turbulent flame speed by 5.0 %. The influence of the inert channel size on the turbulent flame speed at stable conditions is thus significantly lower than the commonly neglected influence of the Soret effect on the turbulent flame speed.

The flashback limit at  $U_b = 10 \text{ ms}^{-1}$  with the inert velocity profile from the small channel is closer to the experimentally observed flashback limit than with the velocity profile from the larger channel. This motivates using the inert base flow from the small channel for flashback simulations at  $U_b = 10 \text{ ms}^{-1}$  and higher. This is supported by the fact that in the experiments, the self-similar structure of the inert velocity profiles was only demonstrated for friction Reynolds number of 310 and higher [36]. In the simulations at  $U_b = 10 \text{ ms}^{-1}$  the friction Reynolds number is however only 290.7. Furthermore,

the turbulence profiles and the shear stress velocities in the experiments also slightly deviated from DNS values and analytical correlations [35, 36]. This justifies using the inert base flow from the smaller inert channel. Using the smaller channel furthermore prevents higher equivalence ratios at flashback conditions, which could require additional mesh refinement and excessive simulation runtimes. For bulk velocities of  $10 \text{ ms}^{-1}$  and higher, the following study of the pressure influence on confined BLF is therefore carried out with the inert base flow from the small channel.

### **5.3 Pressure Influence on Confined Boundary Layer Flashback**

The simulations at atmospheric pressure showed that the chosen numerical model is capable of predicting experimental flashback limits and of reproducing the qualitative flashback process. The model can therefore also be used for the investigation of BLF at operating conditions where no experimental data is available.

Gas turbine burners are commonly operated at elevated pressure. The pressure influence on the BLF flashback process is therefore of high technical relevance for a safe gas turbine operation. However, despite the high technical relevance, the pressure influence on confined turbulent BLF has not been investigated so far. The numerical model is therefore applied to BLF simulations at different pressure levels. Changing the pressure would also have an influence on the molecular viscosity of the gas mixture and thereby on the Reynolds number of the channel flow. The inert velocity profile in the following simulations is nevertheless not changed from the inert velocity profile in the atmospheric simulations. Comparing the simulation results at different pressure levels with unchanged inert base flow allows for an isolated analysis of the pressure influence on global and local combustion parameters. Specifically the pressure influence on average quantities such as the turbulent flame speed and the average velocity field are investigated in the following. The pressure influence on local quantities such as the local quenching distance and the separation zone size during BLF are also investigated. The results are then

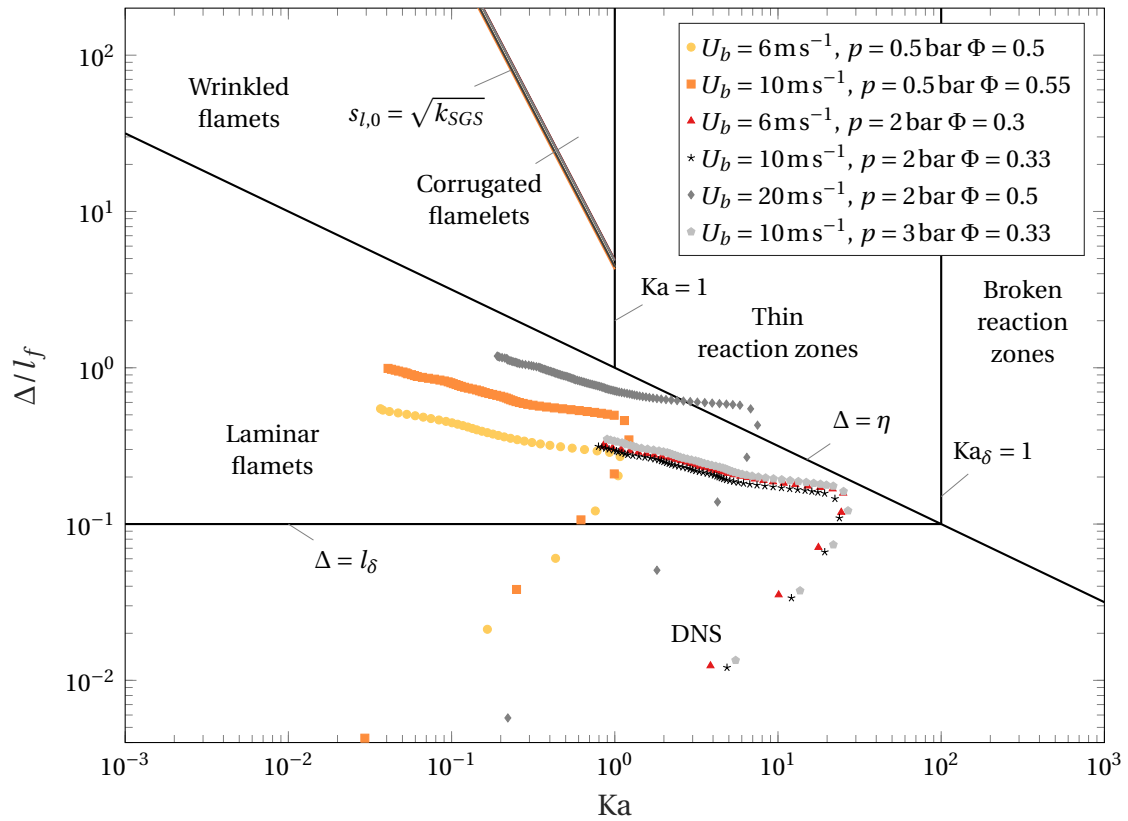
used to improve the basic understanding of the BLF process, especially in regard to flashback prediction with analytical flashback prediction models.

Numerical simulations with bulk velocities ranging from  $6 \text{ m s}^{-1}$  to  $20 \text{ m s}^{-1}$  are carried out at pressures between 0.5 bar and 3 bar. At  $U_b = 6 \text{ m s}^{-1}$  the pressure is varied between 0.5 bar and 2 bar. As the inert base mesh is rather coarse at this bulk velocity, the cell count in x-direction is again increased by a factor of 1.5 for the reactive simulation. A maximum of two cell splits are additionally applied by the adaptive mesh refinement algorithm. As higher pressures than 2 bar would require a costly third cell split, pressure is limited to 2 bar at  $U_b = 6 \text{ m s}^{-1}$ . Pressure at  $U_b = 10 \text{ m s}^{-1}$  is varied between 0.5 bar and 3 bar. At  $p = 0.5 \text{ bar}$ , the inert base mesh is not changed and only one additional cell split is applied by the adaptive mesh refinement. At  $p = 2 \text{ bar}$ , the inert base mesh is also not changed but two adaptive cell splits are applied. At  $p = 3 \text{ bar}$ , the inert base mesh is refined by increasing the cell count in x-direction by a factor of 1.5. Additionally, two adaptive cell splits are applied.

This refinement strategy with the parameters from Table 5.2 results in the LES regime diagram in Figure 5.12 for the highest equivalence ratios under investigation. The regime diagram is created with a similar approach as for the atmospheric simulations described in Section 5.2.3. The laminar flame speed at atmospheric pressure is again obtained from Equation (5.2). The pressure influence on the laminar flame speed is accounted for by the proportionality  $s_{l,0} \propto p^e$ . The pressure exponent  $e$  for each equivalence ratio is obtained from the results of Bradley et al. [13]. The regime diagram shows that except for  $U_b = 20 \text{ m s}^{-1}$  at  $p = 2 \text{ bar}$ , all cases lie within the laminar flamelet and the DNS regimes. The quasi-laminar combustion model is valid in these cases. At  $U_b = 20 \text{ m s}^{-1}$  and  $p = 2 \text{ bar}$  however, some cells clearly lie within the thin reaction zone regime. The quasi-laminar combustion model is not valid in this regime. Accurate quantitative results are therefore not expected here. For a qualitative investigation of the pressure influence on the combustion process at high bulk velocities, this case is nevertheless included in the following.

**Table 5.2:** Parameters for the combustion regime analysis at subatmospheric and elevated pressure.

$p$ in bar	$\Phi$	$T_{ad}$ in K	$s_{l,0} _{p=1\text{bar}}$ in $\text{m s}^{-1}$	$e$	$\alpha$ in $\text{m}^2 \text{s}^{-1}$ $\times 10^{-5}$	$\nu$ in $\text{m}^2 \text{s}^{-1}$ $\times 10^{-5}$	Le	$D$ in $\text{m}^2 \text{s}^{-1}$ $\times 10^{-4}$
0.5	0.5	1640.1	0.61	-0.29	7.051	3.666	0.435	1.621
0.5	0.55	1741.4	0.76	-0.26	7.275	3.722	0.458	1.587
2	0.3	1183.1	0.15	-0.43	1.521	0.8604	0.361	0.4211
2	0.33	1257.2	0.20	-0.40	1.559	0.8689	0.370	0.4212
2	0.5	1640.7	0.61	-0.29	1.763	0.9166	0.435	0.4053
3	0.33	1257.2	0.20	-0.40	1.039	0.5793	0.370	0.2808


**Figure 5.12:** LES combustion regimes at subatmospheric and elevated pressures.

### 5.3.1 Pressure Influence on Confined Flashback Limits

The flashback equivalence ratios obtained from numerical simulations at pressures levels between 0.5 bar and 3 bar are depicted in Figure 5.13. Here, the error bars indicate the equivalence ratio difference between the last stable simulation and the first simulation with full flame flashback. Despite increasing the equivalence ratio up to  $\Phi = 1.7$ , no flashback is observed at  $U_b = 20 \text{ ms}^{-1}$  and  $p = 0.5 \text{ bar}$ . In one-dimensional freely propagating flame simulations with Cantera, the minimum laminar flame thickness at  $p = 0.5 \text{ bar}$  is reached below  $\Phi = 1.7$ . Furthermore, the laminar flame speed decreases beyond  $\Phi = 1.7$ . The turbulent flame speed thus also decreases when increasing the equivalence ratio beyond  $\Phi = 1.7$ . No flashback is therefore expected to occur beyond  $\Phi = 1.7$  and the case at  $U_b = 20 \text{ ms}^{-1}$  and  $p = 0.5 \text{ bar}$  is not included in Figure 5.13.

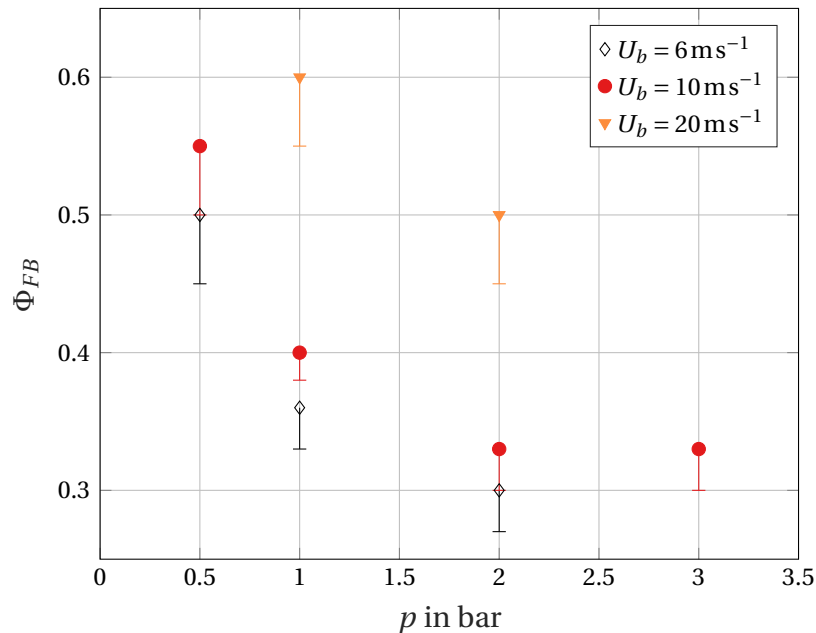


**Figure 5.13:** Pressure influence on numerical confined BLF limits.

Figure 5.13 shows that at pressures up to 2 bar, the flashback equivalence ratio decreases with increasing pressure. This is in accordance with previous studies of the pressure dependence of unconfined BLF limits of hydrogen-air flames. A constant pressure exponent  $n$  for each bulk velocity was iden-

tified by Daniele et al. [24] and Kalantari et al. [80] for the pressure dependency  $\Phi_{FB} \propto p^{-n}$ . The pressure exponent for the unconfined flashback limits was found to lie between  $n = 0.43$  and  $n = 0.49$ . The confined flashback limits in the current simulation do not exhibit a constant pressure exponent. The pressure exponent at  $U_b = 10 \text{ m s}^{-1}$  is  $n = 0.46$  between  $p = 0.5 \text{ bar}$  and  $p = 1 \text{ bar}$ . Between  $p = 1 \text{ bar}$  and  $p = 2 \text{ bar}$ , the pressure exponent is  $n = 0.28$ . These pressure exponents are similar to the pressure exponents at  $U_b = 6 \text{ m s}^{-1}$  and  $U_b = 20 \text{ m s}^{-1}$ . When increasing the pressure from  $p = 2 \text{ bar}$  to  $p = 3 \text{ bar}$  at  $U_b = 10 \text{ m s}^{-1}$ , the flashback equivalence ratio does not change at all and the pressure exponent is  $n = 0$ .

Between  $p = 0.5 \text{ bar}$  and  $p = 1 \text{ bar}$ , the pressure exponent is thus similar to the pressure exponents observed by Daniele et al. [24] and Kalantari et al. [80] for unconfined BLF. The pressure exponent is however not constant and decreases with increasing pressure. The influencing parameters on the pressure dependency of BLF limits are investigated in the following by means of global and local combustion parameters.

### 5.3.2 Macroscopic Flame Structure

The pressure influence on the macroscopic flame structure is demonstrated in Figure 5.14. Here, the propagating flame fronts at  $U_b = 10 \text{ m s}^{-1}$  are depicted at all four investigated pressure levels. The flame front wrinkling increases and the wrinkling length scales decrease with increasing pressure. The radius of the leading flame tip also decreases with decreasing flame front wrinkling size.

The decreasing flame wrinkling length scales and the decreasing flame tip radius with increasing pressure can either be caused by a lower flame thickness or by an increased effect of thermal-diffusive instabilities. Figure 5.15 shows the flame thickness profiles at different bulk velocities and pressure levels. Increasing pressures cause the flame thickness to decrease. The flame thickness at the channel center line at  $U_b = 10 \text{ m s}^{-1}$  decreases from  $0.94 \text{ mm}$  at  $p = 0.5 \text{ bar}$  to  $0.61 \text{ mm}$  at  $p = 1 \text{ bar}$ ,  $0.36 \text{ mm}$  at  $p = 2 \text{ bar}$  and to  $0.29 \text{ mm}$  at  $p = 3 \text{ bar}$ . The pressure dependence of the flame thickness is thus not as strong at high pressures as it is at low pressures. This is in accordance with

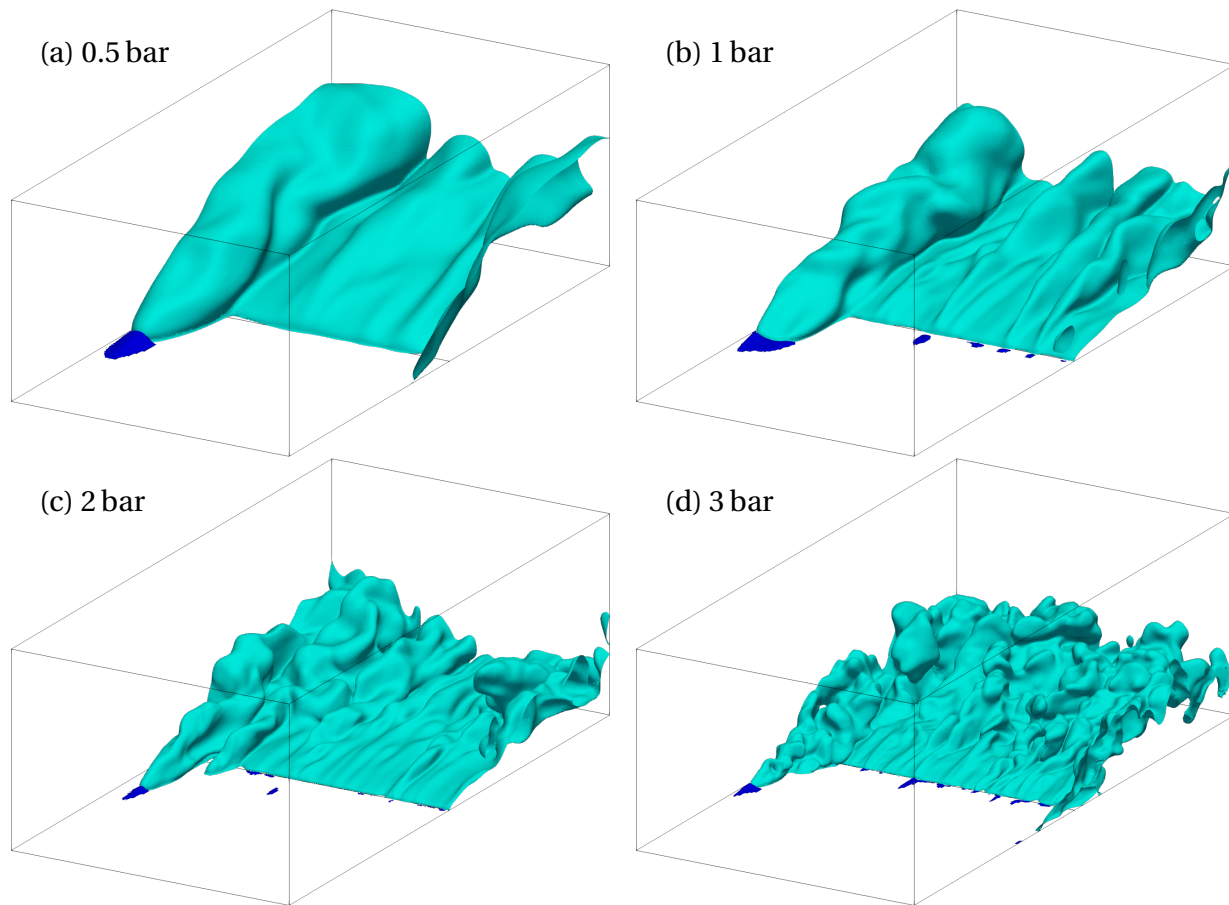


**Figure 5.14:** Instantaneous flame fronts during flashback at different pressure levels. For  $U_b = 10 \text{ ms}^{-1}$ . The light blue isosurface at  $c = 0.5$  represents the flame front and the dark blue isosurface at  $u_x = 0$  represents the separation zone.

the pressure dependence of the flame thickness of laminar freely propagating flames shown in Figure 5.16. The laminar flame thickness at low equivalence ratios and pressure levels decreases with increasing pressure. The laminar flame thickness at low equivalence ratios and higher pressure levels however increases with increasing pressure. At  $\Phi = 0.33$  for example, the laminar flame thickness only decreases up to approximately  $p = 1.6 \text{ bar}$  and starts to increase at higher pressures. At very high pressure levels, the flame thickness of all equivalence ratios decreases again with increasing pressure. At higher equivalence ratios, such as  $\Phi = 0.5$ , the rise of flame thickness is smaller and shifted towards higher pressure levels.

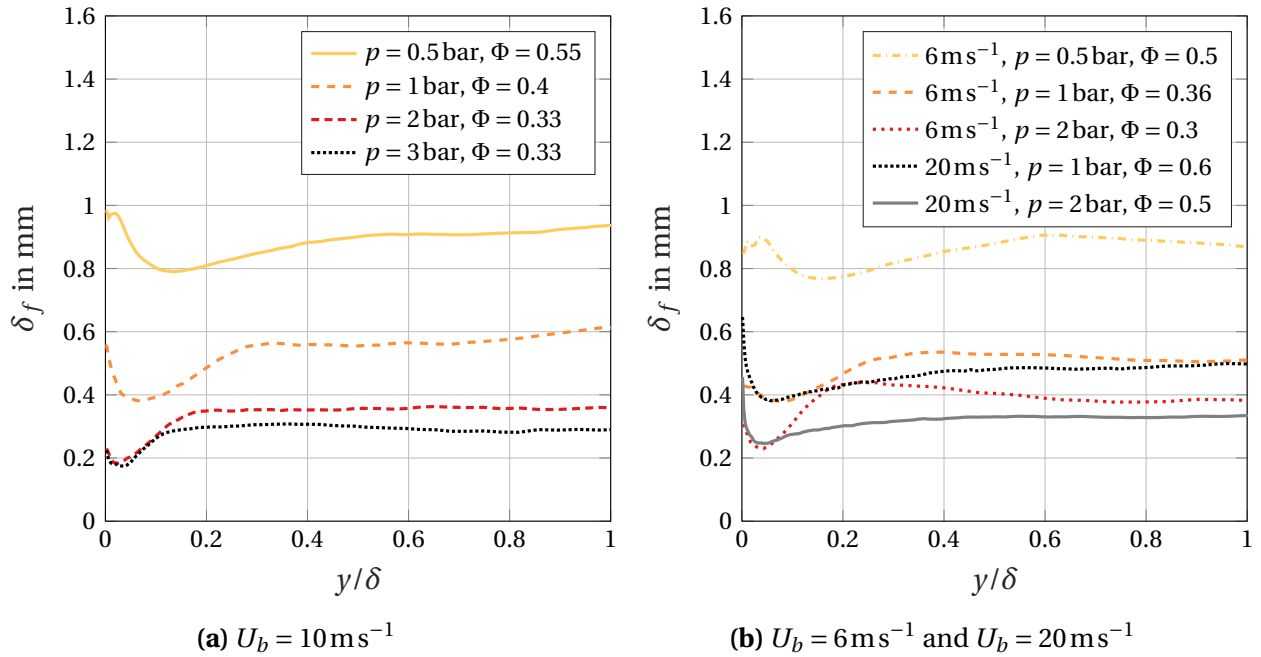


**Figure 5.15:** Flame thickness profiles at flashback conditions for different pressure levels.

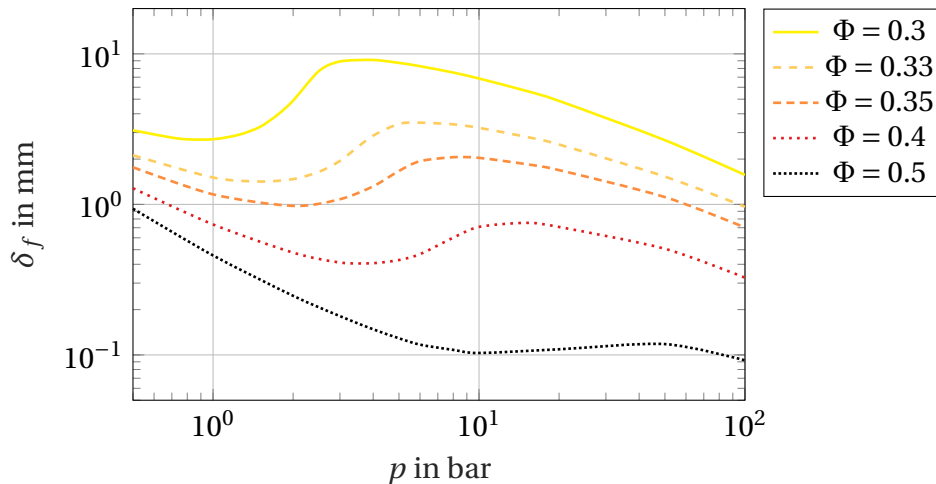


**Figure 5.16:** Pressure influence on the laminar flame thickness. Obtained from one-dimensional freely propagating flame simulations in Cantera [53].

The flame thickness profiles in Figure 5.15 can be used to demonstrate that the minimum flame resolution criterion of three cells per flame thickness is still satisfied. The resulting flame resolution ranges from 7.4 cells per flame thickness for  $U_b = 6 \text{ m s}^{-1}$  at  $p = 0.5 \text{ bar}$  down to 3.0 cells per flame thickness for  $U_b = 10 \text{ m s}^{-1}$  at  $p = 3 \text{ bar}$ . The resolution criterion is thus fulfilled in all simulations.

Pressure is expected to have a limited direct influence on thermal-diffusive instabilities. The adiabatic flame temperature does not change with pressure. According to equation (2.3), the mixture Lewis number thus also does not change with pressure. The effective equivalence ratio of the turbulent flame is therefore also expected to be pressure independent. This is confirmed in Figure 5.17, where the ratio of the effective equivalence ratio  $\Phi_{eff}$  to the actual equivalence ratio is plotted over the global Lewis number. The effective equivalence ratio of all stable cases is obtained with a similar approach as for atmospheric flames in section 5.2.4. The mixture Lewis number is calculated from equation (2.3). The effective equivalence ratio approximately follows the logarithmic fit  $\Phi_{eff}/\Phi = -0.26 \log_{10}(\text{Le} - 0.34) + 0.99$  with a maximum deviation of 6.3 % of the actual equivalence ratio  $\Phi$ . At the investigated operating conditions, pressure thus only has a limited influence on the effective equivalence ratio resulting from thermal-diffusive processes. Flame wrinkling is therefore mainly affected by the pressure influence on the flame thickness.

#### 5.3.3 Average Flame Shape and Turbulent Flame Speed

In the previous section it was found that increasing the pressure decreases the flame thickness and the flame tip radius. The lower flame tip radius at higher pressures allows the tip to propagate inside smaller low speed turbulence streaks and flow separation zones. The smaller flame thickness at higher pressures also increases flame front wrinkling. This has an effect on the average flame shape and the turbulent flame speed. Figure 5.18 shows the average flame shapes of the highest stable equivalence ratio for different pressure levels and bulk velocities. It is evident that the flame angle between the lower channel wall and the average flame front decreases with increasing pressure.

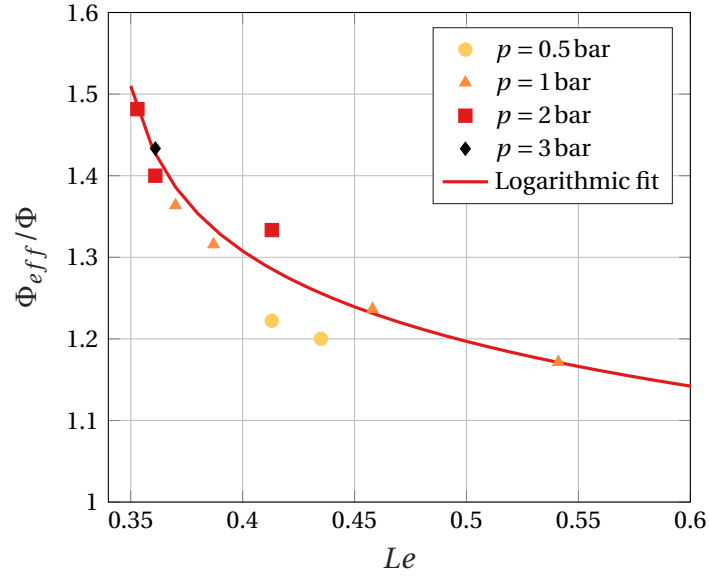


**Figure 5.17:** Effective equivalence ratios at the highest stable equivalence ratios. The red line shows a logarithmic fit through the points at the lowest and highest occurring Lewis numbers.

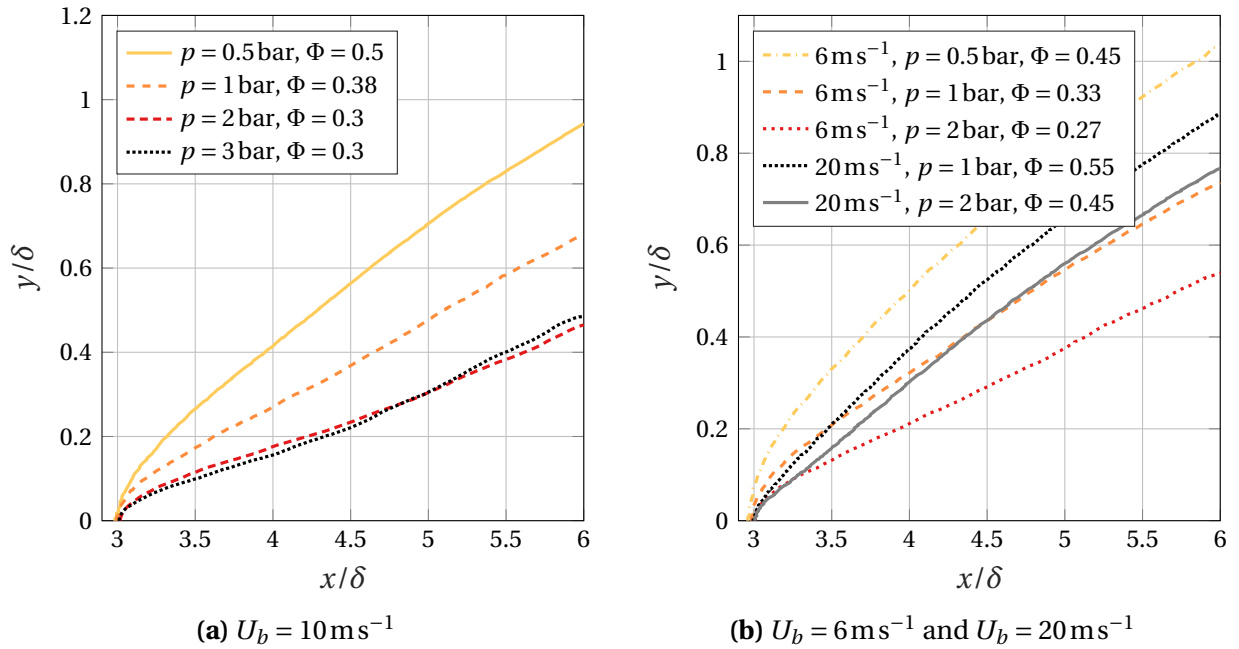


**Figure 5.18:** Stable average flame shapes at different pressure levels. The average flame shape is represented by the  $\bar{c} = 0.5$  isoline.

This indicates that the turbulent flame speed decreases with increasing pressure although the flame front wrinkling increases at higher pressure levels. The stronger flame front wrinkling thus does not compensate the drop of the laminar flame speed with increasing pressure and decreasing equivalence ratio. This leads to different stable flame angles at near-flashback conditions. The average flame angle is thus not an indicator for the flashback propensity of confined flames.

The average flame angle is an inaccurate measure for the turbulent flame speed as the velocity profile ahead of the flame is modified by flow deflection due to combustion. The actual turbulent flame speed profiles at stable conditions are therefore depicted in Figure 5.19 for different pressure levels. The turbulent flame speed is obtained with a similar method as for Figure 5.10. The turbulent flame speed profiles are again normalized by the maximum turbulent flame speed of each bulk velocity. The turbulent flame speed profiles confirm the observations from the average flame shapes. The turbulent flame speed decreases with increasing pressure. At  $U_b = 6 \text{ ms}^{-1}$ , the maximum turbulent flame speed at  $p = 2 \text{ bar}$  is only 71 % of the maximum turbulent flame speed at  $p = 0.5 \text{ bar}$ . At  $U_b = 10 \text{ ms}^{-1}$ , the maximum turbulent flame speed at  $p = 3 \text{ bar}$  is reduced to 73 % of the maximum turbulent flame speed at  $p = 0.5 \text{ bar}$ . At  $U_b = 20 \text{ ms}^{-1}$ , the pressure increase to  $p = 2 \text{ bar}$  reduces the maximum turbulent flame speed to 87 % of the maximum turbulent flame speed at atmospheric pressure. According to Equation (1.9), this change in maximum turbulent flame speed would result in a reduction of the flashback channel centerline velocity by 42 %, 40 % and 20 % for  $U_b = 6 \text{ ms}^{-1}$ ,  $U_b = 10 \text{ ms}^{-1}$  and  $U_b = 20 \text{ ms}^{-1}$ , respectively. It can therefore be concluded that the turbulent flame speed and Equation (1.9) are both poor indicators for the susceptibility of BLF. The flashback limit is thus not only dependent on the turbulent flame speed and the expansion ratio of the flame.

#### 5.3.4 Average Pressure and Velocity Fields

Eichler et al. [34] showed in their experimental study that confined flames cause a pressure rise ahead of the flame. Eichler [36] showed that this pres-

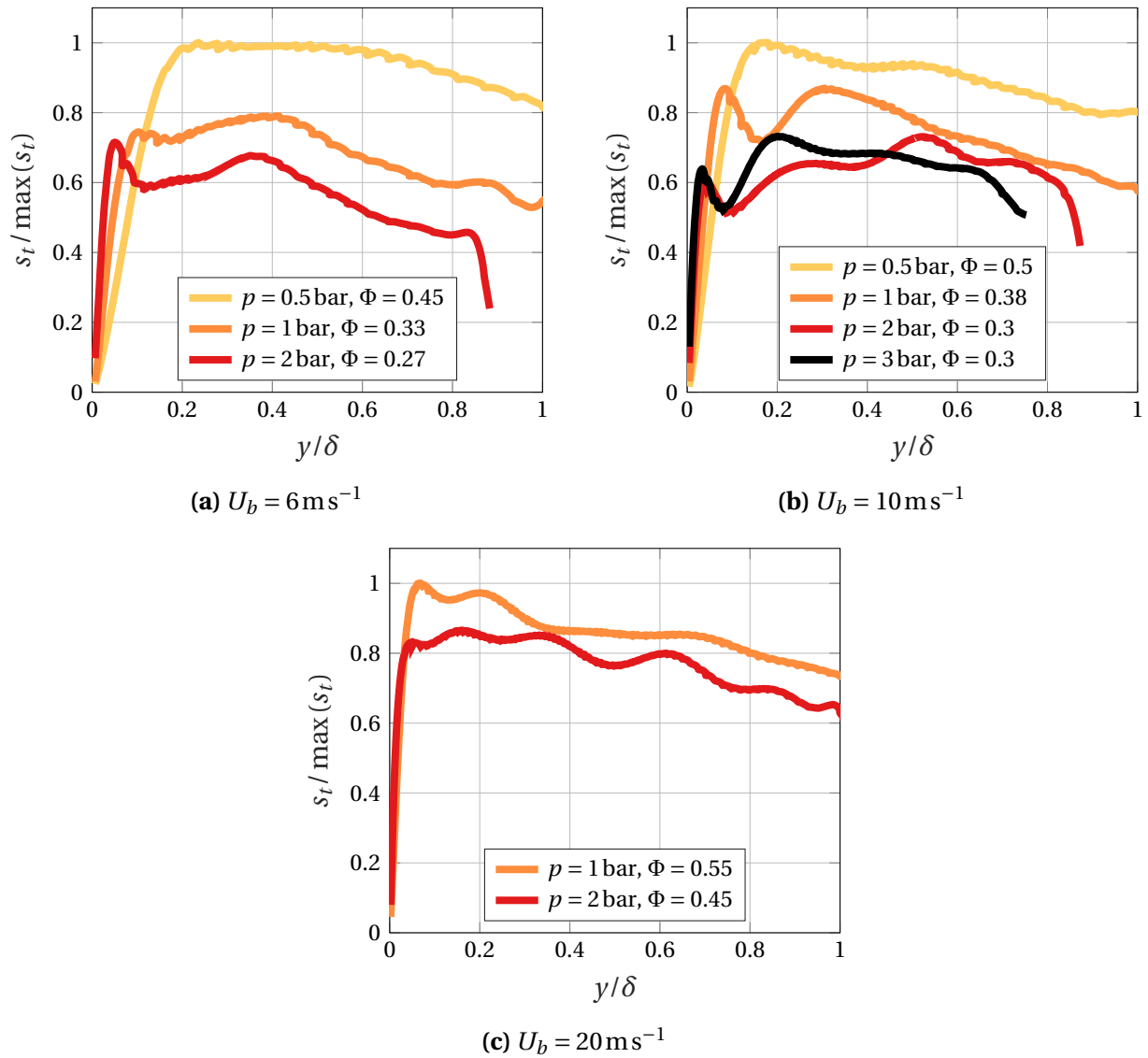


**Figure 5.19:** Normalized turbulent flame speed profiles at different bulk velocities and pressure levels.

sure rise is caused by the streamline curvature due to the two-dimensional flame shape. This is confirmed by the time and spanwise averaged pressure field and streamlines in Figure 5.20 (a). Ahead of the flame front, the streamlines are deflected away from the wall. The pressure field has a peak ahead of the foremost flame position. A sketch of this flow pattern is shown in Figure 5.21. It is evident that the flow pattern is similar to the flow pattern at a convex flame bulge towards the fresh gas in Figure 2.2. At the flame front, the tangen-

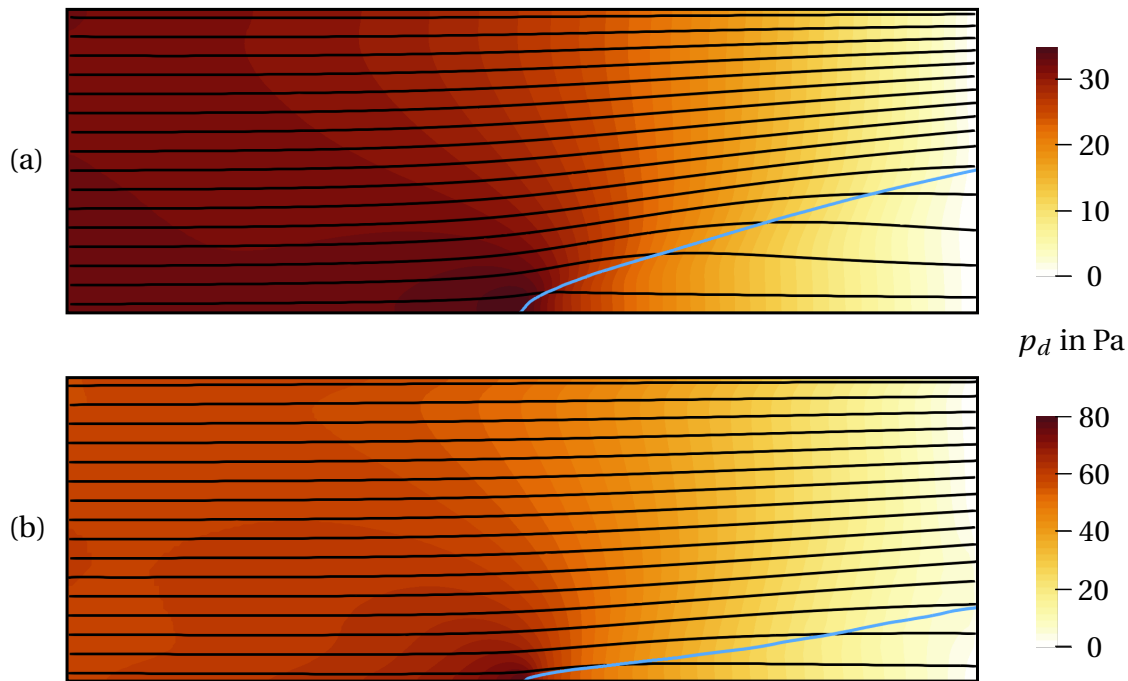


**Figure 5.20:** Average streamlines, flame shape and pressure field at the highest stable equivalence ratio at  $U_b = 10 \text{ ms}^{-1}$  [39]. For (a)  $p = 0.5$  bar and (b)  $p = 3$  bar. The average flame shape is represented by the blue  $\bar{c} = 0.5$  isoline.

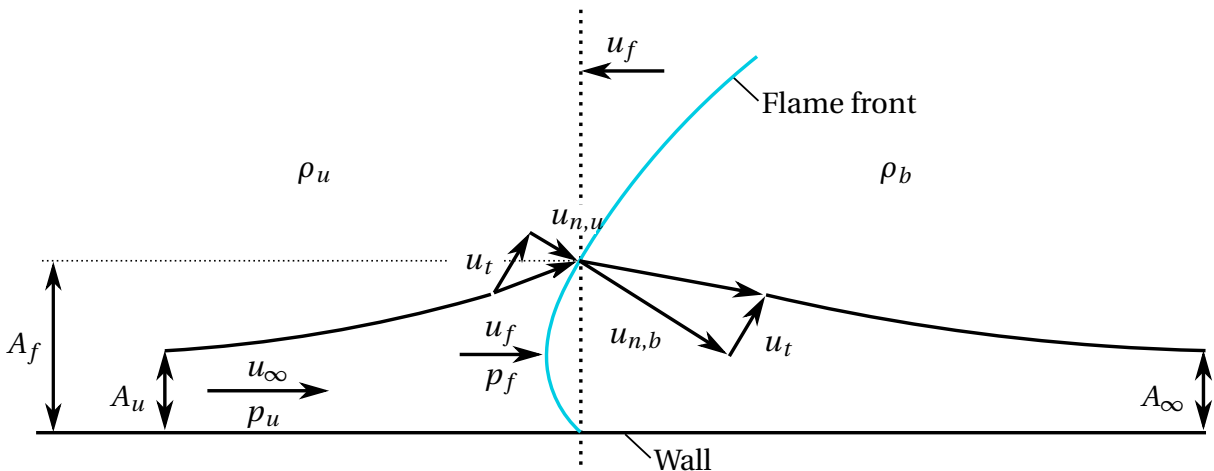


**Figure 5.21:** Flow deflection mechanism ahead of a confined flame front.

tial gas velocity  $u_t$  is not changed by heat release. The velocity component  $u_n$  normal to the flame front increases due to the density drop across the flame front. This redirects the flow towards the normal vector of the flame front and

towards the wall. This in turn causes flow deflection away from the wall ahead of the flame. The streamlines widen and the axial gas velocity decreases in order to fulfill mass conservation upstream of the flame front:

$$\rho_u A_u u_\infty = \rho_u A_f u_f \Rightarrow u_f = \frac{A_u}{A_f} u_\infty < u_\infty. \quad (5.5)$$

When approximately assuming a non-viscous and incompressible fluid, the energy conservation equation

$$p_u + \frac{1}{2} \rho_u u_\infty^2 = p_f + \frac{1}{2} \rho_u u_f^2 \quad (5.6)$$

shows that ahead of the flame, the pressure increases by

$$\Delta p = p_f - p_u = \frac{1}{2} \rho_u u_\infty^2 \left( 1 - \left( \frac{A_u}{A_f} \right)^2 \right) > 0. \quad (5.7)$$

At a bulk velocity of  $10 \text{ ms}^{-1}$ , the pressure rise ahead of the flame in Figure 5.20 is 2.5 Pa at  $p = 0.5 \text{ bar}$  and 26.5 Pa at  $p = 3 \text{ bar}$ . The pressure rise is thus significantly higher at  $p = 3 \text{ bar}$  than at  $p = 0.5 \text{ bar}$ . This can be explained by the higher fresh gas density at higher pressures, which leads to higher inertia.

The flashback equivalence ratio decreases with increasing pressure. This decreases the expansion ratio  $\rho_u/\rho_b$  with increasing pressure and reduces flow redirection at the flame front. At higher pressure levels, the flow deflection by the flame front is therefore weaker than at low pressure levels. This is shown by the comparison of the streamline patterns at  $p = 0.5 \text{ bar}$  and  $p = 3 \text{ bar}$  in Figure 5.20. At  $p = 0.5 \text{ bar}$ , streamline deflection is significantly stronger than at  $p = 3 \text{ bar}$ . According to Equation (5.5), this leads to lower axial gas velocities  $u_f$  at the flame front at lower pressure levels. This implies that the boundary layer at  $p = 0.5 \text{ bar}$  is closer to boundary layer separation than the boundary layer at  $p = 3 \text{ bar}$ .

The difference in flow pattern at different pressure levels shows that average boundary layer separation and average flow deflection ahead of the flame are no reliable indicators for BLF. The same was already concluded for the average flame shape and the turbulent flame speed. These average quantities alone

can thus not predict the BLF propensity of a confined flame. It can instead be assumed that local phenomena at the flame tip - such as flame quenching and local boundary layer separation - have to be taken into account for fully describing the BLF process and propensity.

### 5.3.5 Quenching Distance and Local Boundary Layer Separation

The analysis of the confined BLF process in Section 5.2.1 shows that BLF is initiated by the formation of a flame tongue and its upstream propagation inside a local separation bubble. The upstream propagation process is subject to flame quenching at the isothermal wall. In the average velocity fields in Figure 5.20, no global boundary layer separation is observed prior to BLF. Local boundary layer separation zones are however observed ahead of the flame front prior to and during upstream flame propagation. The upstream propagation velocity is therefore expected to be strongly influenced by the local boundary layer separation zone size ahead of the flame tip.

Figure 5.22 shows examples for hydrogen reaction rate contour plots on a longitudinal cutting plane through the foremost flame tip during flashback at  $U_b = 20 \text{ m s}^{-1}$  and  $p = 1 \text{ bar}$ . In addition, the separation zone is represented by the green line in Figure 5.22. The separation zone is defined as the region where the streamwise velocity  $u_x \leq 0$ . The wall-normal size of this separation zone is the separation zone size  $y_s$ . Figure 5.22 (a) shows that the leading flame tip is located inside the separation zone during upstream flame propagation and that the flame is quenched at the wall. The quenching distance can be obtained from the minimum hydrogen reaction rate profile at the right side of Figure 5.22. The minimum reaction rate profile is obtained from the minimum hydrogen reaction rate evaluated at the wall distances of each cell in wall-normal direction. The quenching distance  $\delta_q$  is then given by the wall distance of the first local maximum of this profile. In Figure 5.22 (a), the quenching distance is for example 0.39 mm and the separation zone size is 0.53 mm. During the phase of flame washout in Figure 5.22 (b), the separation zone size drops to 0.17 mm while the quenching distance is 0.37 mm. The quenching distance is thus approximately constant while the separation zone size is reduced to a

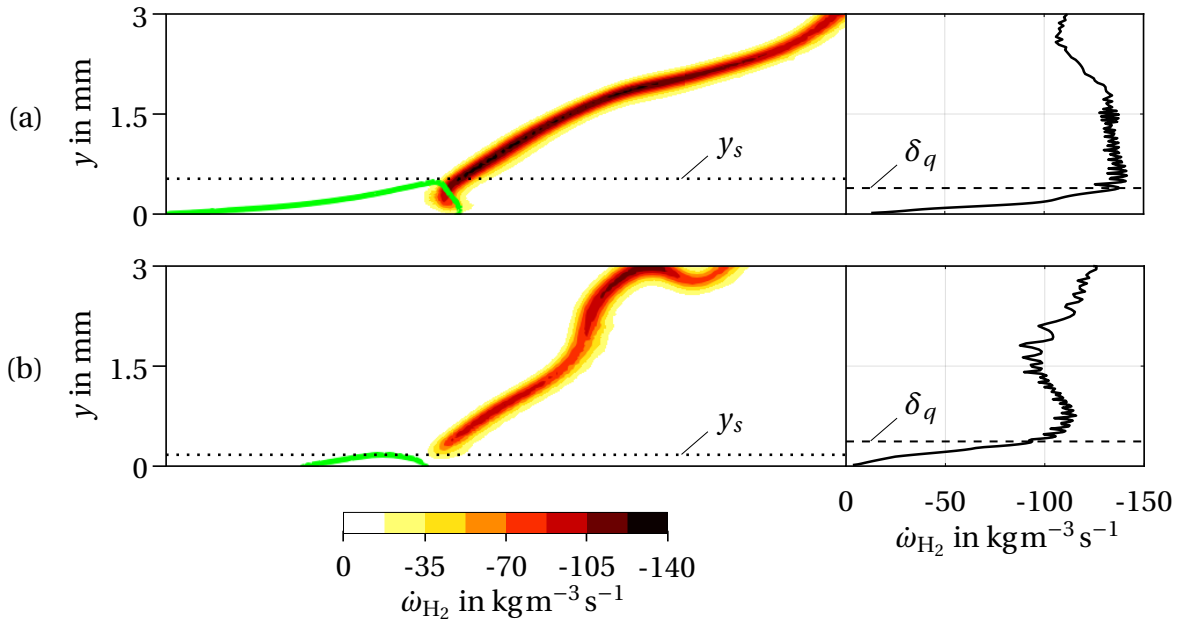


**Figure 5.22:** Hydrogen reaction rate and flame separation zone at one time step during (a) upstream flame propagation and (b) flame washout at  $U_b = 20 \text{ ms}^{-1}$  and  $p = 1 \text{ bar}$ . At the left: contour plot of the hydrogen reaction rate and separation zone represented by the green line. At the right: the resulting maximum hydrogen reaction rate profile.

smaller value than the quenching distance. This has the effect that the flame can no longer propagate inside the separation bubble and that the flame is washed out.

The separation zone size and the quenching distance is evaluated at every time step of upstream flame propagation in order to obtain average quenching and separation parameters at flashback conditions. For  $U_b = 20 \text{ ms}^{-1}$  and  $p = 1 \text{ bar}$ , the separation zone size and the average quenching distance is plotted in Figure 5.23 together with the position  $x_f$  of the leading flame tip. The flame continuously propagates upstream between  $t = 0 \text{ ms}$  and  $t = 2 \text{ ms}$ . Except for a short time interval at  $t \approx 0.9 \text{ ms}$ , the separation zone size is significantly larger than the average quenching distance of  $0.36 \text{ mm}$ . The same holds for later phases of upstream propagation, for example between  $t = 6 \text{ ms}$  and  $t = 7 \text{ ms}$ . When the separation zone size is smaller or has the same order

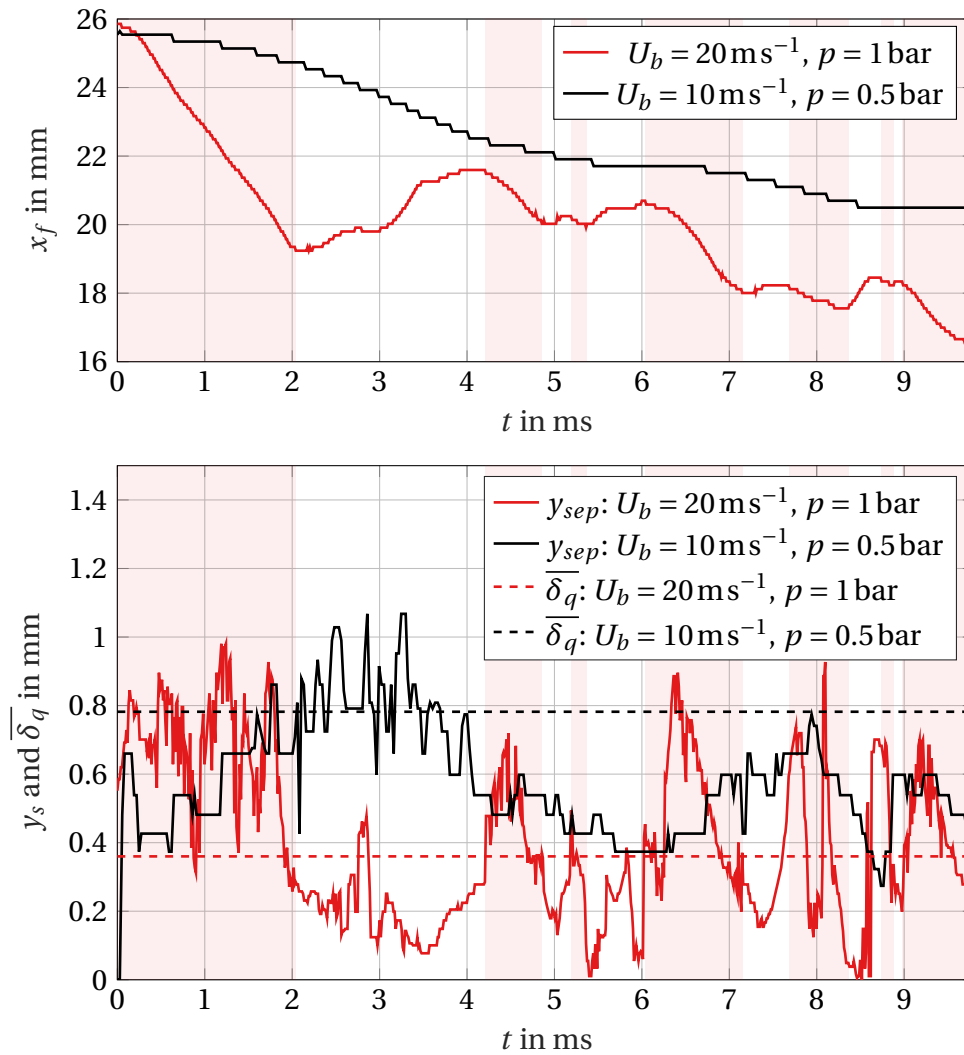


**Figure 5.23:** Flame front position  $x_f$ , local separation zone size  $y_s$  and average quenching thickness  $\overline{\delta}_q$  during flame flashback. The flame front position is defined as the  $x$  position of the foremost cell with  $c > 0.5$ . Phases of upstream flame propagation at  $U_b = 20 \text{ ms}^{-1}$  are highlighted in red.

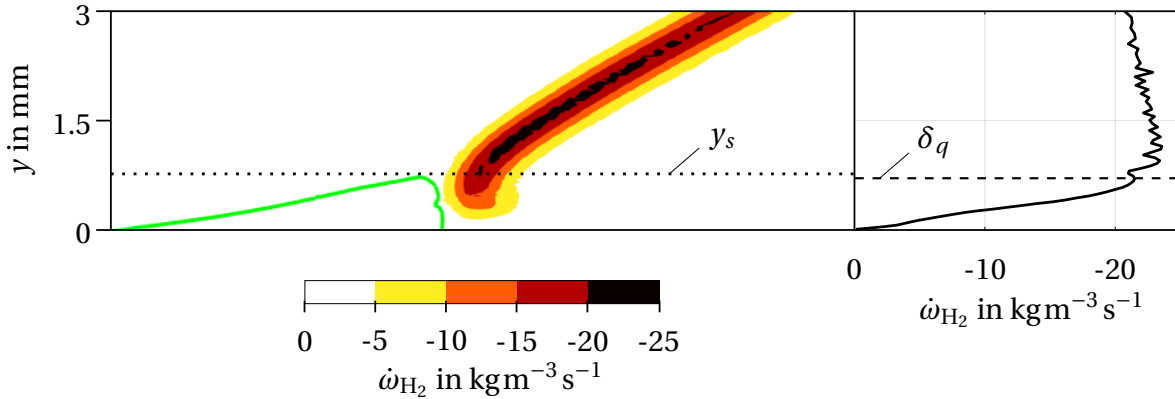


**Figure 5.24:** Hydrogen reaction rate and flame separation zone at one time step during upstream flame propagation at  $U_b = 10 \text{ m s}^{-1}$  and  $p = 0.5 \text{ bar}$ . Similar to Figure 5.22.

of magnitude as the quenching distance, the flame is decelerated or washed downstream by the approaching flow. This is for example the case between  $t = 2 \text{ ms}$  and  $t = 4.2 \text{ ms}$ . The finding of Eichler [36], that BLF occurs when the separation zone size is larger than the quenching distance, is thus confirmed by the simulation at  $U_b = 20 \text{ m s}^{-1}$  and  $p = 1 \text{ bar}$ . The hydrogen reaction rate profile and flame separation zone at  $U_b = 10 \text{ m s}^{-1}$  and  $p = 0.5 \text{ bar}$  in Figure 5.24 however show a different behaviour. During upstream flame propagation at  $p = 0.5 \text{ bar}$ , the flame thickness and the quenching thickness are both larger than at  $U_b = 20 \text{ m s}^{-1}$  and  $p = 1 \text{ bar}$ . The quenching thickness at this particular time instance is  $0.71 \text{ mm}$  and similar to the separation zone size of  $0.77 \text{ mm}$ . The average quenching distance, the separation zone size and the axial flame position for  $U_b = 10 \text{ m s}^{-1}$  and  $p = 0.5 \text{ bar}$  are also plotted in Figure 5.23. The quenching distance temporarily even exceeds the separation zone size in the course of upstream propagation. This is the case for example from the onset of upstream flame propagation up to  $t = 1.7 \text{ ms}$ . The condition that the separation zone size has to exceed the quenching distance is thus not a requirement for BLF at  $U_b = 10 \text{ m s}^{-1}$  and  $p = 0.5 \text{ bar}$ .

The quenching and separation parameters of all cases at flashback conditions are listed in Table 5.3. This allows for a more comprehensive investigation of the relation between the separation zone size and the quenching distance during upstream flame propagation. Both the flame thickness and the quench-

ing distance decrease with increasing pressure. The quenching Peclet number  $Pe_q$  describes the ratio of quenching thickness  $\delta_q$  to the flame thickness  $\delta_f$  at the quenching wall distance. The flame thickness at  $\delta_q$  is obtained from the flame thickness profiles in Figure 5.15. Except for the case at  $U_b = 20 \text{ m s}^{-1}$  and  $p = 2 \text{ bar}$ , which has several cells within the thin reaction zone regime, the quenching Peclet number of the investigated flashback cases ranges from 0.90 to 1.31. Gruber et al. [59] and Dabireau et al. [22] found quenching Peclet numbers of 1.4 and 1.7 for head-on quenching of laminar hydrogen-air and hydrogen-oxygen flames. The quenching Peclet numbers obtained from the current LES are thus smaller but of similar order of magnitude as the literature values. The existing discrepancy can be explained by the difference in quenching configuration. The numerical quenching Peclet numbers in the cited literature are exclusively given for head-on quenching. In head-on quenching, a flame front propagates in normal direction towards a wall. Flame propagation stops at the quenching distance when the heat loss exceeds a critical value [119]. In BLF however, the flame propagates parallel to a wall. This is similar to the sidewall quenching configuration.

**Table 5.3:** Quenching and separation parameters at flashback conditions.

$U_b$ in $\text{m s}^{-1}$	$p$ in bar	$\Phi$	$\overline{\delta}_q$ in mm	$\delta_f _{y=\overline{\delta}_q}$ in mm	$Pe_q$	$\overline{y}_{sep}$ in mm	$\overline{y}_{sep}/\overline{\delta}_q$
6	0.5	0.5	0.83	0.80	1.04	1.03	1.23
6	1	0.36	0.44	0.39	1.12	0.78	1.78
6	2	0.3	0.21	0.24	0.90	0.63	2.91
10	0.5	0.55	0.78	0.81	0.96	0.66	0.84
10	1	0.4	0.42	0.39	1.06	0.65	1.56
10	2	0.33	0.24	0.18	1.31	0.54	2.23
10	3	0.33	0.18	0.18	1.00	0.39	2.16
20	1	0.6	0.36	0.39	0.92	0.55	1.53
20	2	0.5	0.18	0.26	0.68	0.28	1.58
30	1	0.75	0.37	0.39	0.94	0.53	1.45

The average separation zone size during upstream flame propagation also decreases with increasing pressure and with increasing bulk velocity. Higher bulk velocities lead to higher velocity gradients at the wall, which reduces the boundary layer separation propensity. Increasing pressure on the other hand

leads to a lower flame thickness, quenching thickness and flame tip radius. At the same time, the equivalence ratio at flashback conditions is reduced at higher pressure levels. This all leads to lower flow deflection at the flame tip, as already seen from the average velocity fields in Figure 5.20. The separation zone size does nevertheless not decrease as fast with pressure as the quenching distance. This can be observed from the ratio of the average separation zone size to the average quenching distance in Table 5.3. The ratio  $\overline{y_{sep}}/\overline{\delta_q}$  increases with increasing pressure for the investigated conditions. For one pressure level and different bulk velocities,  $\overline{y_{sep}}/\overline{\delta_q}$  is also not constant. It varies between values of 0.84 at  $U_b = 10 \text{ m s}^{-1}$  and  $p = 0.5 \text{ bar}$  up to 2.23 at  $U_b = 10 \text{ m s}^{-1}$  and  $p = 2 \text{ bar}$ . There is thus no unique ratio of separation zone size and quenching distance that predicts the onset of BLF.

## 5.4 Implications for Analytical Flashback Prediction

It was already outlined in Section 5.3.3 that Equation (1.9) used in the analytical model by Hoferichter et al. [71] is not suited for confined BLF prediction. The current simulation results and the findings of Eichler [36] furthermore indicate that the pressure rise calculation in the analytical model according to Equation (1.7) is also incorrect. Equation (1.7) predicts a pressure rise of 32.3 Pa for the stable atmospheric case at  $U_b = 10 \text{ m s}^{-1}$  and  $\Phi = 0.38$ . The pressure rise ahead of the flame observed in the LES results is only 5.5 Pa. This pressure rise is similar to that obtained by Endres and Sattelmayer in [38] with a fully compressible solver at similar conditions. The lower pressure rise compared to the pressure rise obtained from Equation (1.7) is thus not caused by the low Mach number approximation. Instead, it appears that the one-dimensional pressure rise estimation in the analytical flashback model overestimates the actual pressure rise needed to cause BLF. This is confirmed by the other atmospheric cases at  $U_b = 6 \text{ m s}^{-1}$  and  $\Phi = 0.33$ ,  $U_b = 20 \text{ m s}^{-1}$  and  $\Phi = 0.55$  and at  $U_b = 30 \text{ m s}^{-1}$  and  $\Phi = 0.7$ . Here Equation (1.7) predicts a pressure rise of 15.2 Pa, 106.4 Pa and 214.3 Pa while a pressure rise of only 1.7 Pa, 22.9 Pa and 63.7 Pa is observed in the simulations.

While the pressure rise ahead of the flame is overestimated in the analyti-

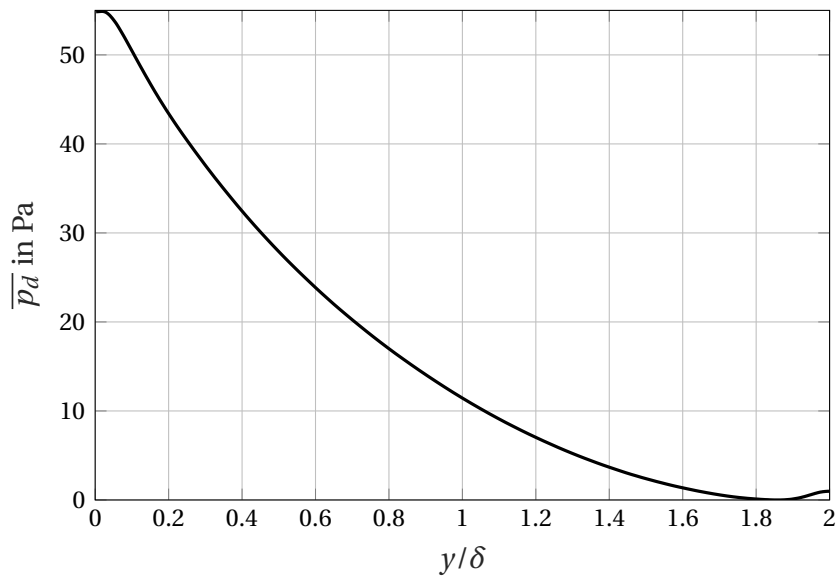


**Figure 5.25:** Wall-normal average pressure profile ahead of the flame front.

cal BLF prediction model of Hoferichter et al., the boundary layer separation propensity is underestimated. The applied Stratford separation criterion is based on the boundary layer theory. One basic assumption of the boundary layer theory is that the pressure in wall-normal direction is uniform in the boundary layer. This requirement is however not fulfilled in confined BLF. Figure 5.25 shows the wall-normal average fluid dynamic pressure profile for the stable atmospheric case at  $U_b = 20 \text{ ms}^{-1}$  and  $\Phi = 0.55$ . In the first half channel height  $\delta$ , the pressure drop is 1.9 times the longitudinal pressure rise ahead of the flame front. It is thus evident that the pressure profile can not be considered uniform in wall-normal direction. In addition to the gas deceleration caused by a uniform axial pressure gradient, the flow is also deflected away from the wall by the wall-normal pressure gradient. This increases the boundary layer separation propensity. The Stratford boundary layer separation criterion cannot be applied in that case as it underestimates the separation propensity of turbulent boundary layers.

The current simulations identified some shortfalls of the analytical flashback prediction model. The boundary layer separation propensity is underestimated and the pressure rise ahead of the flame front is overestimated. Furthermore, the influence of local combustion parameters on the flashback

propensity is neglected in the analytical flashback prediction model. The errors introduced by these shortfalls appear to compensate each other. This allows the analytical flashback prediction model to nevertheless predict flashback limits and to account for changes in flashback influencing parameters such as preheat temperature or fuel composition [69].

## 5.5 Summary of Confined BLF Results

LES with detailed chemical kinetics, a detailed diffusion model and the quasi-laminar combustion model were applied to simulations of confined BLF at atmospheric pressure. It was shown that the implemented solver is capable of reproducing the BLF process as previously observed in experiments. Prior to BLF, local separation zones are formed upstream of the stable flame front in low velocity streaks. A flame tongue is formed and flame propagation inside the separation zone is initiated when the separation zone exceeds a certain limit. Full flashback occurs when upstream flame propagation outweighs flame washout by higher velocity turbulent streaks.

It was further shown that the numerical flashback limits approximately reproduce the experimental flashback limits. An accurate diffusion model was shown to be essential to accurately represent the flashback process of lean hydrogen-air flames. Differential diffusion, non-equidiffusion and Soret diffusion lead to a flame structure, which is similar to a laminar flame with a higher effective equivalence ratio. Neglecting Soret diffusion slightly increases the hydrogen mass fraction in lower temperature regions. However, neglecting Soret diffusion decreases the hydrogen radical concentrations and the hydrogen reaction rates, which leads to lower turbulent flame speeds. The Soret effect is therefore essential for the accurate prediction of BLF limits. The comparison of these results with findings of Grcar, Bell and Day [56] showed that the slight underprediction of flashback propensity at low bulk velocities and equivalence ratios is most likely caused by the mixture averaged formulation of the diffusion model. The channel length of the inert base flow simulations on the other hand only had a limited effect on the flashback limits.

After showing that the computational model is capable of qualitatively and quantitatively reproducing the BLF process, the influencing parameters on flashback limits were assessed by means of simulations at different pressure levels. The comparison of simulation results with the same inert base flow at different pressures showed that increasing the pressure from 0.5 bar to 3 bar decreases the flashback equivalence ratio. The flame thickness is reduced, which leads to stronger flame wrinkling at smaller length scales and smaller flame tip diameters. The average flame angle, turbulent flame speed and average streamline deflection ahead of the flame prior to flashback however decrease with increasing pressure. The investigated average flame properties alone are consequently only a poor indicator for the flashback propensity. Instead, local parameters such as the local separation zone size ahead of the propagating flame tongue and the quenching thickness have to be accounted for. The local flow deflection and the local separation zone size decreases with increasing pressure. This decreases the flashback propensity with increasing pressure. At the same time, the quenching thickness is reduced with increasing pressure. This allows the flame to propagate closer to the wall, which increases flashback propensity. These two local effects are counteracting but do not compensate each other. Instead, the ratio of separation zone size to quenching distance at flashback conditions varies strongly with pressure and bulk velocity. There is no unique  $\overline{y_{sep}}/\overline{\delta_q}$  at which flashback occurs. Flashback can even occur when the separation zone is smaller than the quenching distance if the turbulent flame speed is high enough.

BLF is thus a complex process, which is influenced by the turbulent flame speed, the local separation zone size and the quenching thickness. The turbulent flame speed and the separation zone size in turn result from different pressure dependent parameters such as the gas density, the laminar flame speed and the flame thickness. The overall effect of increasing pressure on BLF is that the ratio of separation zone size to quenching distance increases. This increases the flashback propensity and reduces the turbulent flame speed and thus the equivalence ratio which is necessary to cause upstream flame propagation.

At last, it was demonstrated that the pressure rise ahead of the flame is over-

estimated in the analytical flashback prediction model of Hoferichter et al. [71]. Furthermore, the assumption of a uniform wall-normal pressure is not fulfilled in confined BLF. The boundary layer theory and the Stratford separation criterion are thus not applicable and the Stratford criterion leads to an underestimation of the boundary layer separation propensity. The flashback limit can not be approximated by Equation (1.9) and is consequently not only dependent on the turbulent flame speed and the expansion ratio of the flame. The errors introduced by these shortfalls appear to compensate each other, so that the analytical model is still capable of accurately predicting the flashback propensity at different operating conditions.

## 6 Reactive LES of Unconfined Boundary Layer Flashback

After having successfully simulated the confined case of BLF, the same modelling approach is now applied to the unconfined case of BLF. The goal is to reproduce the flashback behaviour of the experimental jet flame burner of Duan, Shaffer and McDonell [29]. In the experiments with a bulk velocity of  $9 \text{ m s}^{-1}$ , BLF was observed at an average equivalence ratio of 0.53. This experimental flashback limit should also be predicted by the numerical simulations. The simulations are additionally expected to give a more detailed insight into the transition process from an unconfined flame stabilized at a backward facing step to a propagating flame inside a tube. The numerical model for the unconfined simulation is presented in the following. Different combustion parameters at stable and unstable conditions are then analyzed in detail.

### 6.1 Numerical Setup for Unconfined Flashback Simulations

The numerical model for unconfined flashback simulations is similar to the numerical model for confined simulations presented in Chapter 5.1. The stainless steel premixing tube with an inner diameter of  $d = 21.16 \text{ mm}$  from Duan, Shaffer and McDonell [29] is chosen as a reference case. The computational domain is outlined in Figure 6.1 (a) together with a turbulent jet flame stabilized at the burner rim. The premixing tube in the simulations has a length of  $0.75d$ . The premixing tube is followed by a circular enclosure with a diameter of  $88.9 \text{ mm}$  and a total length of  $5d$ . The enclosure diameter is twice the diameter of the small enclosure in [29]. The large enclosure size limits the influence of the boundary conditions at the enclosure walls on the flame. It was noted by Duan et al. [30] that the flashback propensity is only sensitive

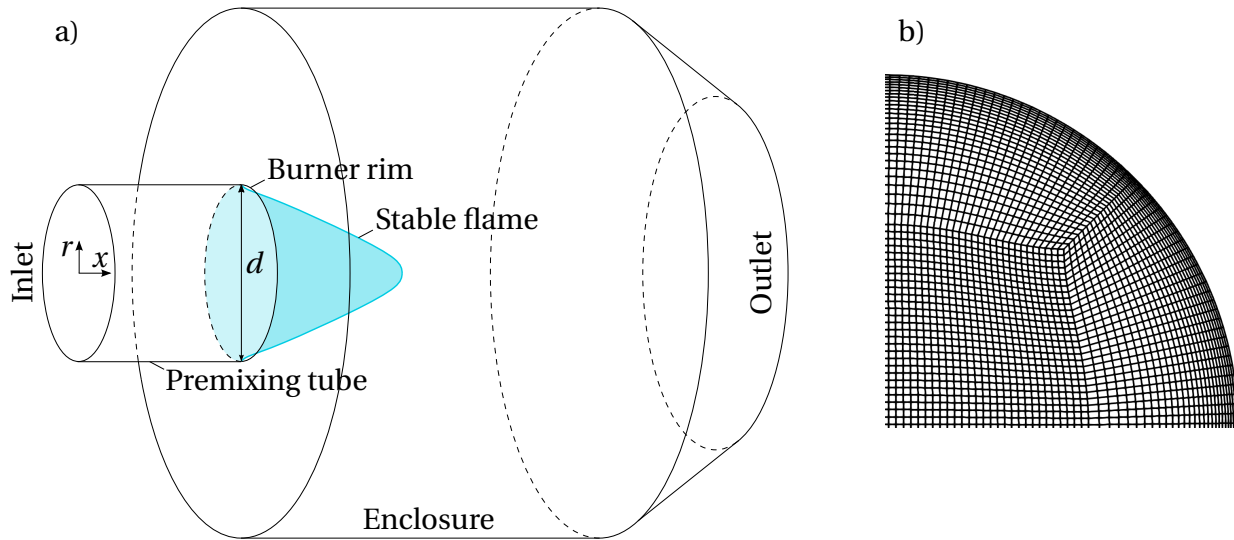


**Figure 6.1:** Computational domain for unconfined flashback simulations with the expected stable flame shape (a) and spatial discretization at the premixing tube inlet (b).

to the change in burner rim temperature and not sensitive to changes in the aerodynamics caused by the enclosure. As the burner rim temperature can be controlled in the simulations, the larger enclosure diameter will not have a significant effect on the results. Starting from  $x = 4.75d$ , the enclosure is tapered towards the outlet to prevent backflow at the outlet. The outlet has a diameter of  $2d$ .

The grid in the premixing tube is again discretized with an o-grid configuration. In contrast to the inert tube, the center grid is not strictly rectangular. This is evident from Figure 6.1 (b), which depicts a quarter of the grid at the premixing tube inlet. The spacing in circumferential direction is similar to the inert grid presented in Chapter 4.1.3. The non-dimensional cell size at the wall is  $\Delta r_W^+ = 2.0$  and thus slightly larger than in the inert simulation. The maximum cell size in radial direction is now  $\Delta r^+ = 10.0$  and the cell size in  $x$  direction is reduced to  $\Delta x^+ = 9.6$  compared to the inert simulations. This results in a more uniform grid spacing. From the premixing tube wall towards the enclosure wall, the grid spacing in radial direction increases by a factor of 16.1. Starting from  $x = 13r$ , the axial grid spacing increases by a factor of 3.9 towards the outlet of the domain. The total cell count with this strategy

is  $9 \times 10^6$ . One additional cell split is applied in the reactive simulations with the adaptive mesh refinement algorithm to ensure a good flame resolution. In addition to the mesh refinement in regions of large hydrogen consumption, the mesh is also refined in regions, where the heat release rate is at least 20 % of the maximum heat release rate in the domain. This results in cell counts over  $11 \times 10^6$  for a stable flame configuration at  $\Phi = 0.5$  with a minimum average resolution of 3.9 cells per flame thickness. With this resolution, all cells lie within the laminar flamelet and DNS regimes of the LES regime diagram.

The unsteady velocity profile from the inert tube simulation at  $9 \text{ m s}^{-1}$  is prescribed at the premixing tube inlet. The hydrogen, oxygen and nitrogen mass fractions are first set to values according to a stable equivalence ratio of 0.5. The inlet gas temperature is set to 294.261 K. The premixing tube and enclosure walls were not cooled in the experiments. The burner rim temperature was instead measured with thermocouples in order to assess the burner rim temperature influence on the flashback limits. The average measured burner rim temperature during flashback at  $U_b = 9 \text{ m s}^{-1}$  was 507 K. The wall temperature profile in the premixing tube is expected to have a strong influence on the flashback limit. Heat transfer inside the premixing tube wall increases the wall temperature upstream of the burner rim. Heat transfer from the tube wall to the near-wall fresh gas flow in turn increases the unburnt gas temperature, the reactivity and the flame speed of the gas mixture. One-dimensional heat transfer inside the tube wall with heat loss to the surroundings results in the temperature profile [132]

$$T = T_u + \frac{\cosh\left(\frac{x}{L}c_{ht}\right)}{\cosh c_{ht}}(T_r - T_u). \quad (6.1)$$

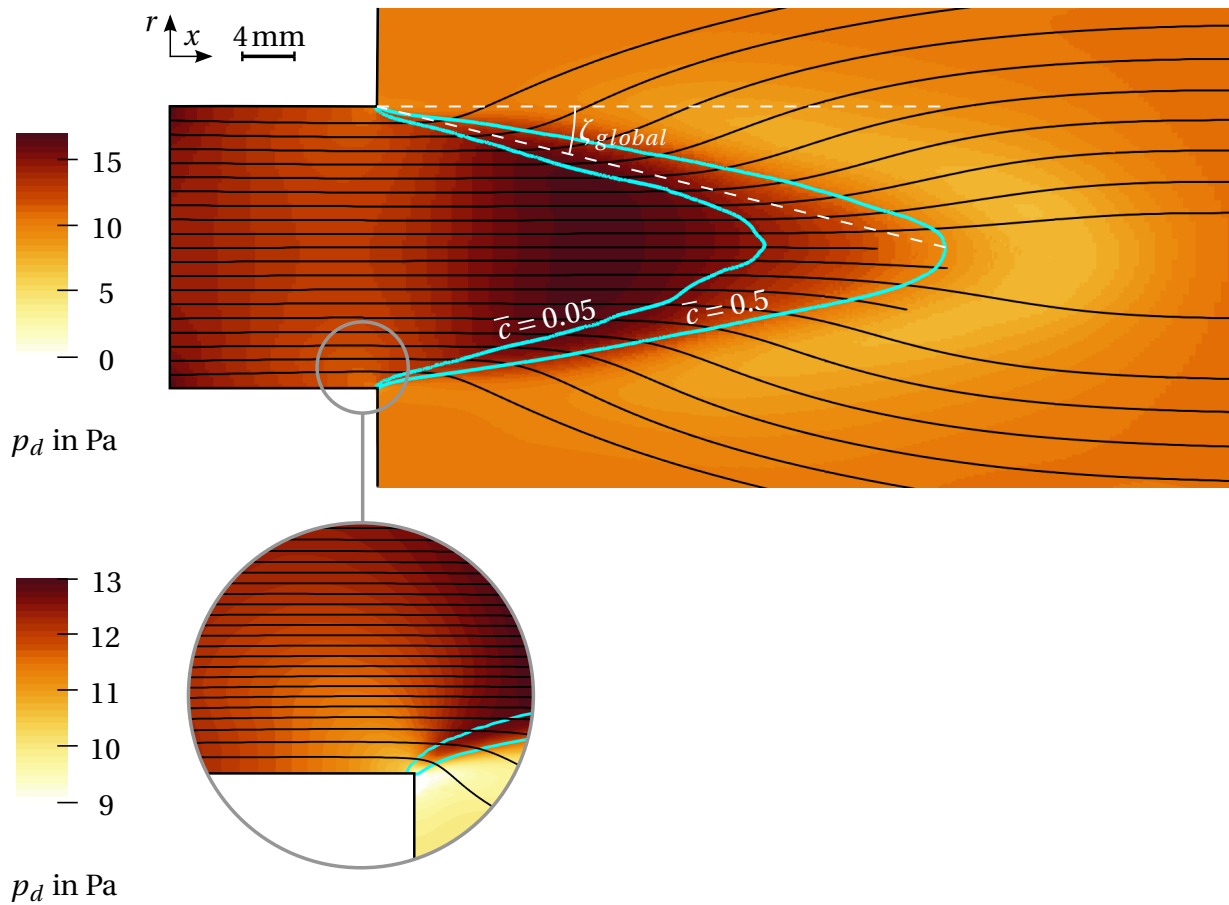
$L$  is the tube length,  $T_r$  is the burner rim temperature and  $c_{ht}$  is a coefficient which represents the heat transfer properties of the tube wall. It is arbitrarily assumed that the unburnt temperature  $T_u$  is reached at  $L = 400 \text{ mm}$  upstream of the burner rim. In the experiments, an additional thermocouple 88.9 mm upstream of the burner rim measured an average temperature of 317.26 K at flashback conditions. Fitting the temperature profile (6.1) to the two measured wall temperatures results in the coefficient  $c_{ht} = 9.821$ . The prescribed wall temperature profile in the simulation thus rises from 438 K at  $x = 0 \text{ mm}$  up to

507 K at the burner rim. The burner rim temperature of 507 K is also prescribed at the x-normal head plate of the enclosure. This ensures that the recirculating gas at the enclosure head plate has the same temperature as the burner rim. The wall temperature of the circumferential walls of the enclosure is set to the unburnt gas temperature of 294.261 K. The velocity boundary condition at all walls is approximated by a no-slip boundary condition. At the outlet, a constant pressure is prescribed and zero-gradient boundary conditions are applied to the species mass fraction, temperature and velocity fields.

## 6.2 Stable Combustion

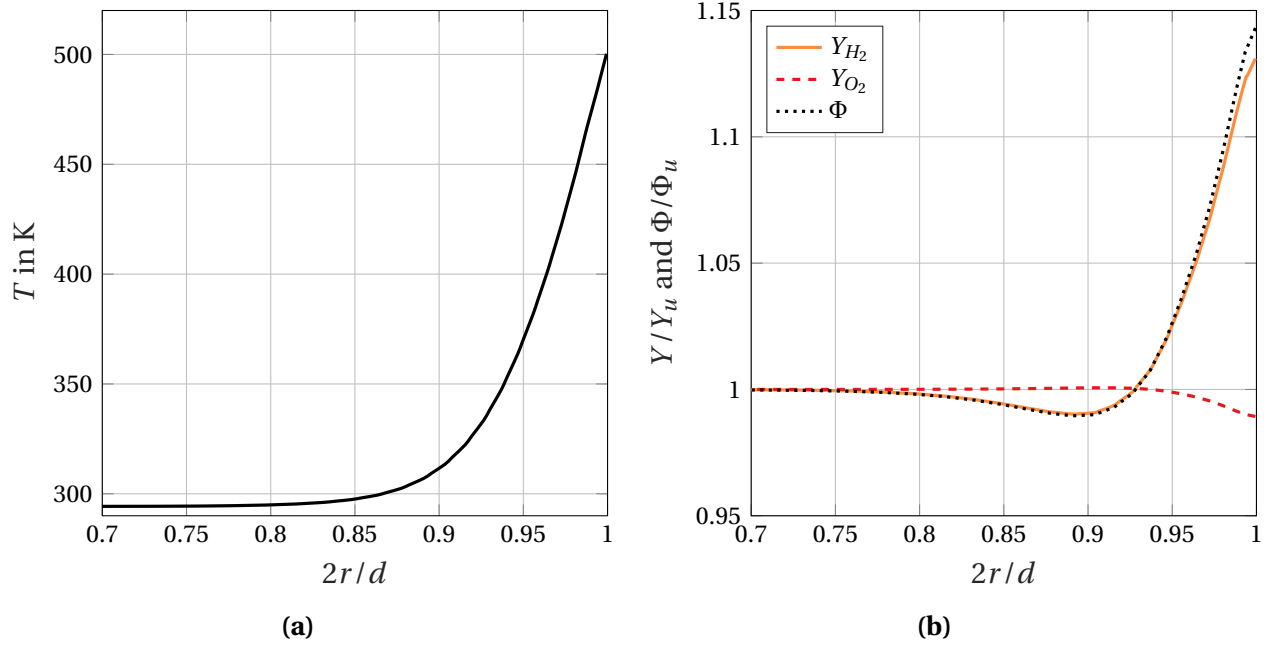
The simulations are initialized with a half spherical flame stabilized at the burner rim. The initial equivalence ratio is set to  $\Phi = 0.5$ . In a thin sheet of 1 mm thickness, temperature and the species mass fractions of hydrogen, oxygen and nitrogen are set to the corresponding equilibrium values. Similar to the confined simulations, the flame front is wrinkled due to thermal-diffusive instabilities and the turbulent velocity fluctuations until a quasi stationary state is attained. Averaging the hydrogen mass fraction field for  $\Phi = 0.5$  over time results in the average flame front on a  $x-r$ -plane in Figure 6.2. The average flame front represents a classical cone shaped flame [24, 129] without an initial outward bend as observed by Baumgartner et al. [3, 5]. Furthermore, the gap flow of fresh gas between between the burner rim and the flame front observed by Baumgartner et al. is not reproduced by the numerical simulations. Instead, the hydrogen mass flow is consumed directly at the burner rim.

Figure 6.2 also shows the average streamlines and the average pressure field of the stable flame. Directly at the flame front, gas expansion due to heat release causes strong streamline deflection away from the burner centerline. This is in accordance with the findings of Baumgartner et al. [3, 5]. The streamlines inside the premixing tube are slightly deflected towards the center of the pipe. This is in contrast to the findings of Baumgartner et al. [3, 5]. The boundary layer deflection is however not directly related to the presence of the flame. Instead, the streamline deflection is caused by gas expansion due to heat transfer from the tube wall to the boundary layer. In the channel burner ex-



**Figure 6.2:** Average streamlines, flame shape and pressure field at stable conditions of the unconfined case. The  $x$ - $r$  plane cuts the domain from  $x = 0$  mm to  $x = 80$  mm and from  $r = -18$  mm to  $r = 18$  mm. The light blue lines represent the  $\bar{c} = 0.05$  and  $\bar{c} = 0.5$  isolines.

periments conducted by Baumgartner et al. [3, 5], the tube wall temperature was controlled by convective air cooling. The burner rim in the experimental setup represented by the current numerical setup was however uncooled, which leads to higher tube wall temperatures. The pressure field in Figure 6.2 does not show a pressure rise at the burner rim. Instead, the pressure field exhibits a minimum at the burner rim. The stable flame thus does not induce a backpressure on the flow inside the premixing tube as in the confined case in Figure 5.20. The difference between the confined and unconfined flame configuration observed by Baumgartner is therefore confirmed by the current numerical simulations.



**Figure 6.3:** Profiles of (a) average temperature and (b) average hydrogen mass fraction, oxygen mass fraction and equivalence ratio in the premixing tube.

The temperature rise at the tube wall does not only have an influence on the velocity field in the tube. The wall temperature also influences the species mass fraction distribution in the premixing tube. Figure 6.3 shows the radial profiles of average temperature, hydrogen mass fraction, oxygen mass fraction and equivalence ratio at a distance of one millimeter upstream of the burner rim. Starting approximately from  $2r = 0.8d$ , the temperature increases from the inlet value of 294.261 K to the tube wall temperature of 500.3 K. This adverse temperature gradient towards the tube wall induces a diffusion mass flux of light molecules towards the wall according to Equation (3.55). The species mass fraction of the light hydrogen molecule at  $2r = 0.87d$  is reduced by up to 0.98 %. At the wall, the hydrogen mass fraction increases by 13.1 %. The diffusion mass flux of the heavier oxygen molecule towards the wall is lower than the diffusion mass flux of the hydrogen molecule. The oxygen mass fraction at the wall is thereby reduced by 1.1 %. The overall effect of Soret diffusion is that the equivalence ratio of the gas mixture is decreased by 1.0 % at  $2r = 0.89d$ . At the wall the equivalence ratio is increased by 14.3 % to  $\Phi = 0.57$ . This strong

fuel enrichment of the gas mixture at the wall is expected to have a strong influence on the near-wall reactivity and the turbulent flame speed. This again demonstrates the importance of the Soret effect in near-wall reactive flows and BLF of hydrogen-rich fuel mixtures.

According to Hoferichter et al. [69, 70], BLF sets in when the local flame brush angle at the position of maximum turbulent velocity fluctuation exceeds the global flame brush angle. The analytical flashback prediction model of Hoferichter et al. [69, 70] includes equations for the turbulent flame speed and the global and local flame angles which can be used for a comparison with the current simulation results. The turbulent flame speed is therefore again analyzed at  $\bar{c} = 0.05$  by means of the average gas velocity normal to the flame front. Here, averaging is performed in time and subsequently in circumferential direction. The resulting turbulent flame speed profile is depicted in Figure 6.4. In the inert simulation, the maximum of the turbulent velocity fluctuation profile lies at a wall distance of  $0.5d - r = 0.65$  mm. At this wall distance, the turbulent flame speed is  $2.19 \text{ m s}^{-1}$ . The average axial velocity 1 mm upstream of the burner rim obtained from a  $x - r$  cutting plane through the domain is  $6.11 \text{ m s}^{-1}$  at the same wall distance. This corresponds to a local flame brush angle of  $\zeta_{local} = 21^\circ$ . According to Equation (1.8) with a constant activation energy and  $s_{l,0}$  according to Equation (5.2), the expected turbulent flame speed at this operating condition is  $2.33 \text{ m s}^{-1}$ . The local turbulent flame speed in the simulations is thus of the same order of magnitude as in the analytical model of Hoferichter et al. [70]. The global flame brush angle evaluated from the analytical flashback model with flame generated turbulence according to Equation (1.14) is  $\zeta_{global} = 19.8^\circ$ . This is in accordance with the average flame brush angle of approximately  $20^\circ$  at  $\bar{c} = 0.05$  in Figure 6.2. The flame brush angle at  $\bar{c} = 0.5$  is however only approximately  $14^\circ$ . This is in turn close to the average flame brush angle of  $13.2^\circ$  predicted from the analytical flashback model with flame generated turbulence according to Equation (1.13). This illustrates the importance of the choice of the  $\bar{c}$  isoline used for the definition of the average flame brush angle.

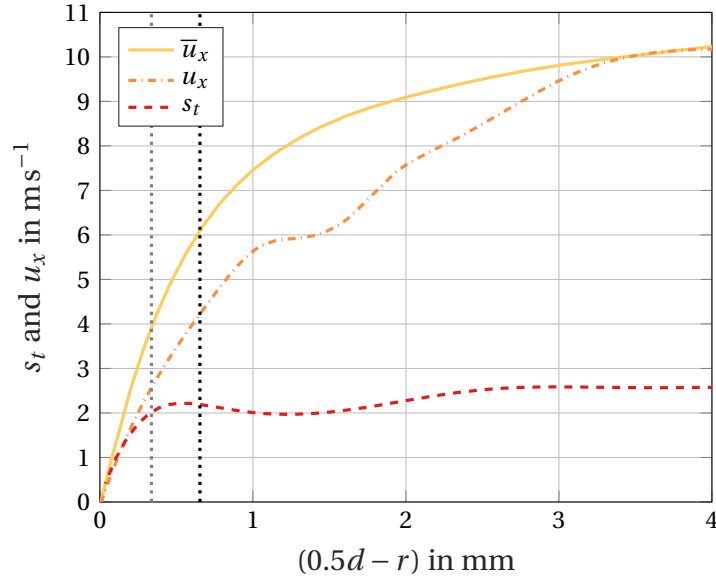


**Figure 6.4:** Turbulent flame speed profile of the unconfined stable flame at  $\Phi = 0.5$  and axial velocity profile in the premixing tube. The black vertical dotted line represents the wall distance of the maximum turbulent velocity fluctuation in the inert simulation. The gray vertical dotted line represents the average quenching distance during upstream flame propagation.

### 6.3 The Unconfined Boundary Layer Flashback Process

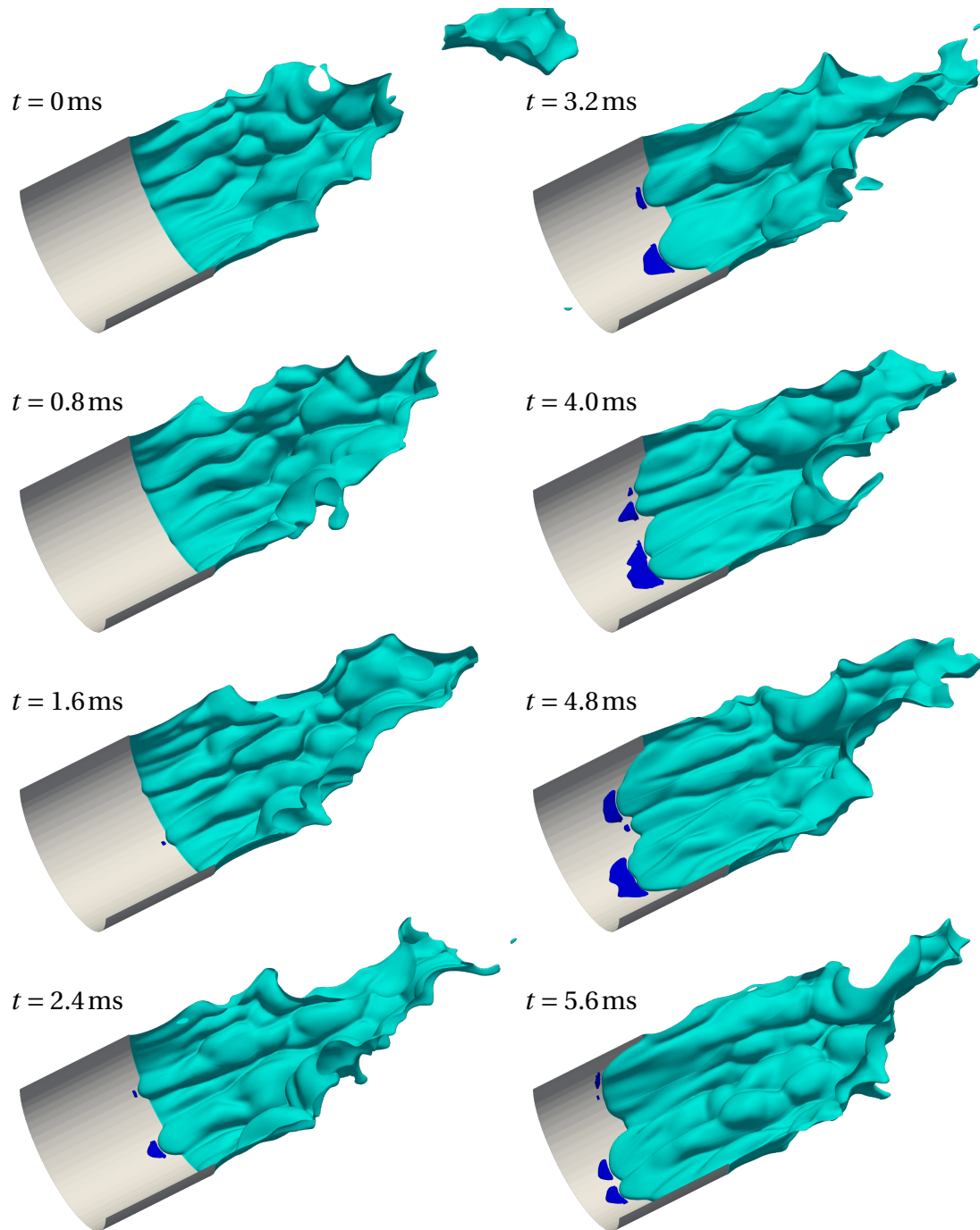
Stable combustion was investigated in the previous section for an equivalence ratio of 0.5. In the reference experiments, BLF was observed at an average equivalence ratio of 0.53. The equivalence ratio in the simulation is therefore increased by 0.05 to  $\Phi = 0.55$  after reaching a quasi stationary state of the flame. Upstream flame propagation is observed shortly after the gas mixture of higher equivalence ratio reaches the turbulent flame front. The experimental flashback limit is thus reproduced by the numerical simulation. This shows that all relevant physical phenomena are incorporated in the numerical model for unconfined BLF and that the boundary conditions accurately represent the experimental conditions.

The unconfined boundary layer flashback process of the numerical simula-

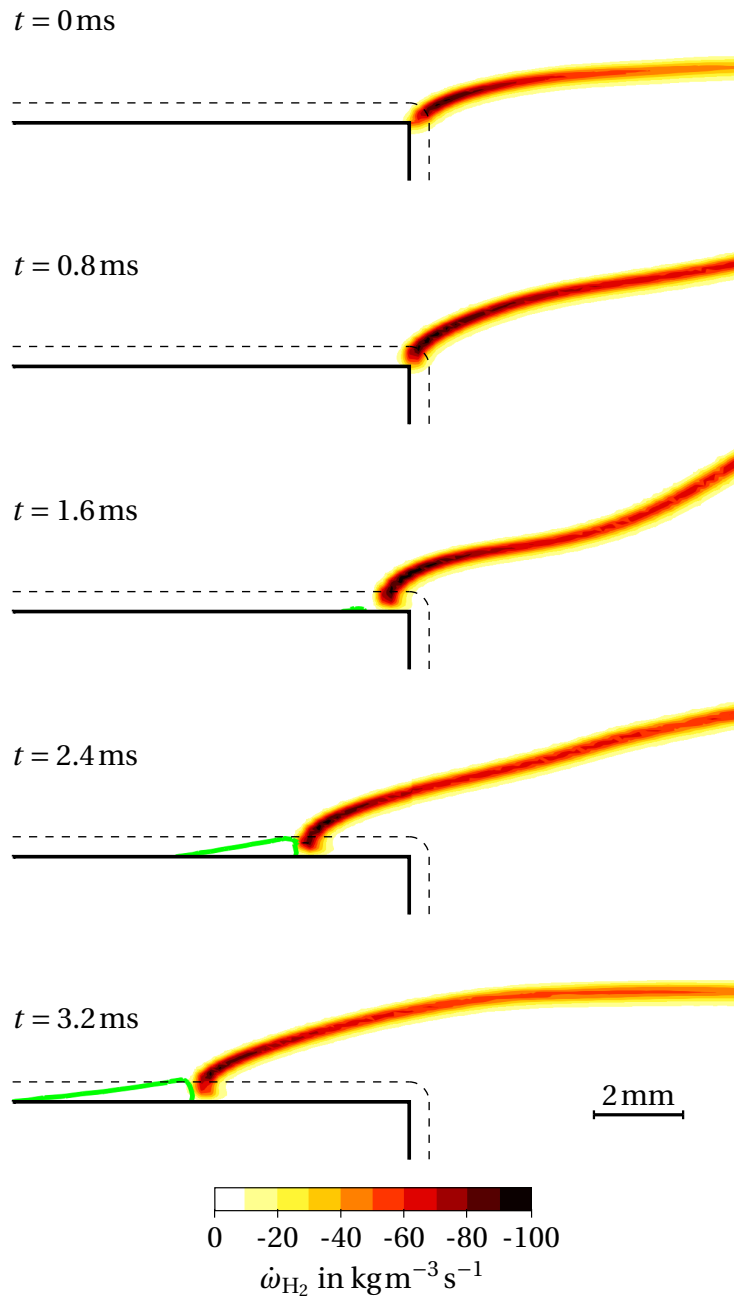
tion can be observed in Figure 6.5. At  $t = 0$  ms, the flame is still stabilized at the burner rim. Similar to the confined case, the flame front is wrinkled and flame bulges are present at the burner rim. As already observed in experimental investigations [3, 5], the approaching flow is however not strongly affected by the presence of the flame and no backflow regions are observed at this stage. Starting from  $t = 0.8$  ms, one flame bulge in the lower part of the burner is lifted up into the premixing tube. At  $t = 1.6$  ms, this flame bulge is already located inside the premixing tube and first boundary layer separation zones appear. As soon as the flame is located inside the premixing tube, the gas acceleration at the flame front towards the tube wall leads to flow deflection ahead of the flame front. From this time step on, the flashback process is similar to the confined case. A second flame bulge is simultaneously lifted over the burner rim and into the premixing tube. The flame front propagates inside the separation zones and follows the streaks of low axial velocity in the boundary layer. During upstream propagation, new flame cusps are formed which either propagate upstream or are washed out.

Figure 6.6 gives a more detailed insight into the transition of the stable flame to the propagating flame inside the premixing tube. It depicts the hydrogen reaction rate and the separation zone on a  $x - r$  cutting plane through the leading flame tip at the bottom of the premixing tube. At  $t = 0$  ms, the flame is still stabilized at the burner rim. It is evident that despite flame quenching at the wall, the hydrogen reaction rate is not zero at the burner rim. In the simulations, there is thus no gap flow of fresh gas between the burner rim and the flame front, which was already assumed from Figure 6.2. The hydrogen reaction rate profile is consistent with the hydrogen reaction rate profile of a confined flame with an isothermal cold wall in Figure 5.22. The hydrogen reaction rate at the isothermal wall is significantly reduced but does not completely extinguish in the vicinity of the wall.

At  $t = 0$  ms, a low velocity turbulence structure is approaching the burner rim. This is evident from Figure 6.4, where the wall normal profile of the instantaneous axial velocity  $u_x$  5 mm upstream of the burner rim is plotted for  $t = 0$  ms. This low axial velocity lifts the flame above the burner rim and into the premixing tube at  $t = 0.8$  ms. At  $t = 1.6$  ms, the flame tip is already located inside



**Figure 6.5:** Unconfined flashback process. The light blue isosurface at  $\bar{c} = 0.5$  represents the flame front in the lower half of the burner and the dark blue isosurface at  $u_x = 0$  represents the separation zone in the premixing tube. The grey surface is the tube wall.



**Figure 6.6:** Hydrogen reaction rate and separation zone during unconfined BLF. The separation zone is depicted by the green isoline. The bold black line is the tube wall and the dashed black line shows the average quenching wall distance.

the premixing tube. This leads to flow deflection and the first occurrence of boundary layer separation. At this stage, the shape of the flame front is already similar to the propagating confined flame in Figure 5.22. In the further propagation process, the separation zone size grows and the flame is accelerated until it approaches the inlet.

### 6.3.1 Flame Quenching during Unconfined Flashback

The hydrogen reaction rate profiles inside the premixing tube allow for the estimation of the quenching distance during upstream propagation. With the same approach as presented for the confined case in Section 5.3.5, the quenching distance at  $\Phi = 0.55$  in the unconfined case is 0.34 mm. This quenching distance is marked as a dashed black line in Figure 6.6. It is evident from the hydrogen reaction rate contour plots that the leading flame tip follows a trajectory with a wall distance similar to the quenching distance. This explains the strong influence of the quenching distance on flashback limits observed in experiments [24, 80]. Furthermore, the hydrogen reaction rate contours at  $t = 0$  ms exhibit their first local maximum at a similar wall distance as the quenching distance during the following upstream flame propagation. Quenching of the stable flame at the burner rim is thus very similar to the sidewall quenching configuration during upstream propagation. The simulations thus do not show the expected transition from head-on quenching to sidewall quenching [3].

The quenching distances in the confined case are  $\delta_q = 0.42$  mm at  $\Phi = 0.4$  and  $\delta_q = 0.36$  mm at  $\Phi = 0.6$ . The quenching distance at an elevated wall temperature in the unconfined case is thus slightly smaller than with a cold wall in the confined case. When neglecting the influence of the flow Reynolds number on the quenching distance, the linearly interpolated quenching distance at a cold isothermal wall at  $\Phi = 0.55$  is estimated to  $\delta_q = 0.375$  mm. The higher wall temperature however also increases the unburnt gas temperature and equivalence ratio. In the stable case, the gas temperature at a wall distance of 0.34 mm increases to 407.6 K and the equivalence ratio rises by 0.03 (Figure 6.3). Locally increasing the equivalence ratio by 0.03 increases the lami-

nar flame speed by 12.3 % according to Equation (5.2). Subsequently increasing the preheat temperature from 294.261 K to 407.6 K additionally leads to a 109.0 % higher laminar flame speed according to one-dimensional freely propagating flame simulations with Cantera. The actual quenching distance at a wall temperature of up to 507 K only lowers the quenching distance by 9.3 % compared to the estimated value at a wall temperature of 293.15 K. The influence of the wall temperature on the flashback limit is thus mainly driven by the increase in local flame speed due to hydrogen enrichment and elevated preheat temperatures.

#### 6.3.2 Comparison with Experimental Results

The onset of BLF observed in Figures 6.5 and 6.6 does not coincide with previous experimental findings of Baumgartner et al. [3, 5]. In their experiments with a cooled channel burner configuration, the flame had an initial outward bend before adapting to a cone shape. A gap flow of fresh gas was observed between the burner rim and the flame front. BLF was initiated at a distance downstream of the burner rim, which was significantly larger than the quenching distance. In the current simulation, the stable flame is cone shaped and no gap flow is observed between the burner rim and the flame front. Flashback occurs directly at the burner rim. The flame is lifted up into the premixing tube by a turbulence structure with low axial velocity. The wall distance of the propagating flame front throughout this transition process is equal to the quenching distance. This flashback process is consistent with the previously observed process of unconfined laminar [97, 106, 144] and turbulent [31, 129] BLF in tube burners.

The cause for the peculiar flame shape and flashback process was not fully clarified by Baumgartner [5]. The experiments of Baumgartner et al. [3, 5] and the reference experiments of the current simulations differ in wall temperature and in burner shape. For lean flames at equivalence ratios below 0.6, Baumgartner et al. [3, 5] noted a strong difference in flashback limits of tube and channel burners. It is thus possible that the burner type also affects the flame shape and the flashback process. A more plausible reason for the differ-

ence in stable flame shape and flame propagation path is the lack of gap flow between the burner rim and the flame front in the numerical simulations. In Chapter 6.3.1 it was shown that lower wall temperatures lead to slightly higher quenching distances and to significantly lower flame speeds at the burner rim. This could prevent flame stabilization directly at the burner rim and lead to the observed gap flow. The difference in stable flame shape and flame propagation path could however also be caused by the numerical model, which might be incapable of correctly reproducing the streamline curvature or flame quenching at the burner rim. This can however not be answered on the basis of the current numerical results. The reason for the lack of gap flow in the current simulations should therefore be investigated in future studies by testing different burner configurations and different operating conditions.

### 6.3.3 Comparison with Analytical Boundary Layer Flashback Models

The average flame fronts in Figure 6.2 already showed that the global flame brush angles used for the analytical flashback prediction model of Hoferichter et al. [69, 70] strongly depend on the choice of  $\bar{c}$  for the flame angle evaluation. This implies that also the comparison of local flame brush angle and global flame brush angle strongly relies on the choice of  $\bar{c}$  for the global flame angle evaluation. Furthermore, the simulations indicate that even for  $\bar{c} = 0.05$ , the local flame brush angle of  $21^\circ$  at  $\Phi = 0.5$  is higher than the global flame brush angle of  $20^\circ$ . The stable flame thus already fulfills the flashback condition of the analytical model of Hoferichter et al. [70].

Instead of the flashback condition  $\zeta_{local} > \zeta_{global}$  in the analytical flashback prediction model [70], the current numerical simulations indicate a physically more plausible condition for the onset of BLF. In accordance with the findings of Baumgartner [5], upstream flame propagation is initiated in the simulations when the turbulent flame speed exceeds the temporary local gas velocity. At  $t = 0$  ms, the local gas velocity  $u_x$  in Figure 6.4 at the quenching distance is only 27.3 % higher than the local turbulent flame speed. This temporarily allows for local flame angles close to  $90^\circ$  when slightly increasing the equivalence ration from  $\Phi = 0.5$  to  $\Phi = 0.55$ . Flame flashback thus commences when

the local flame speed at the quenching distance is higher than the temporary local gas velocity. This is in accordance with the critical gradient model when calculating the critical gradient from the temporary local gas velocity at the quenching distance instead of from the average velocity profile. The analytical flashback model of Hoferichter et al. [69, 70] can nevertheless be seen as a valid flashback prediction model, which accurately accounts for the influence of fuel composition, preheat temperature and the turbulent duct flow on BLF limits.



## 7 Summary and Conclusions

BLF is an inherent threat in premixed combustion of hydrogen rich fuels. The ability to predict flashback limits is important for the safe operation of gas turbine burners. One method to predict the BLF limits is by conducting numerical simulations. The BLF limits of hydrogen-rich fuels have however not yet been accurately predicted with numerical simulations. The goal of this study was therefore to model confined and unconfined BLF numerically, accurately predict the BLF limits and gain a detailed insight into the BLF process.

A realistic inert base flow is essential for the accurate reproduction of experimental BLF limits. Inert LES of a turbulent channel and pipe flow have therefore been conducted with the incompressible OpenFOAM solver `pimpleFoam`. It was found that LES with the Smagorinsky turbulence model accurately reproduce DNS profiles of average velocity and turbulent kinetic energy at high Reynolds numbers. The Smagorinsky model however overestimated the SGS viscosity at low Reynolds numbers. The implicit turbulence modelling approach on the contrary was found to accurately predict low Reynolds DNS data from literature.

Confined and unconfined BLF of hydrogen-air flames was investigated after having obtained an accurate inert base flow. A computational fluid dynamics solver on the basis of the OpenFOAM solver `reactingFoam` was developed for this purpose. The reactive solver incorporates adaptive mesh refinement, finite rate chemistry and a detailed mixture averaged diffusion model with Soret diffusion. LES with this solver were capable of quantitatively reproducing experimental flashback limits of confined and unconfined BLF. The confined flashback propensity was only slightly underestimated at very lean gas mixtures. The investigation of the diffusion model influence on the predicted flashback limits showed that a detailed diffusion model is essential for BLF modelling of hydrogen-air flames. Preferential diffusion and non-equi diffu-

sion leads to higher flame wrinkling and higher turbulent flame speeds. Preferential diffusion also increases the effective equivalence ratio of the gas mixture and thereby affects the inner flame structure. Soret diffusion increases radical concentrations in the flame and thereby also increases the turbulent flame speed. At hot surfaces, the Soret effect additionally increases the local equivalence ratio, which leads to higher turbulent flame speeds and to lower quenching distances. Soret diffusion can therefore not be neglected when modelling combustion of hydrogen-rich fuels. The underestimation of confined flashback limits at low equivalence ratios was traced back to the mixture averaged diffusion model. A full multicomponent diffusion model should therefore be tested in future studies with regard to the prediction accuracy of experimental flashback limits.

The phenomenological investigation of the confined BLF process observed in the LES showed high correspondence with the BLF process previously observed in experimental investigations and laminar simulations. It was confirmed that backflow regions already exist ahead of the stable flame front prior to BLF. These separation zones are formed in turbulence streaks of low axial velocity. Upstream flame propagation is initiated when the separation zone size exceeds a critical value. During upstream flame propagation, the flame propagates inside the separation zone and the separation zone follows the path of the low velocity streaks. The turbulence structures in the boundary layer additionally affect the BLF process by inducing flame washout and the formation and coalescence of flame cusps. Full flame flashback was only observed when phases of upstream propagation outweighed the phases of flame washout.

Additional LES of confined flashback were conducted at different pressure levels between 0.5 bar and 3 bar in order to investigate the pressure influence on different combustion parameters during BLF. It was found that the flashback equivalence ratio decreases with increasing pressure. This is caused by a combination of several local and global effects. Pressure has an influence on the laminar flame speed, the flame thickness, the local quenching distance, the local separation zone size and on flame wrinkling. In the investigated pressure range, the ratio of separation zone size to quenching distance increases

---

with increasing pressure. This leads to a higher flashback propensity. Lower turbulent flame speeds and equivalence ratios are therefore necessary to initiate upstream flame propagation at higher pressures. Confined BLF limits are thus not only dependent on average flame properties such as the turbulent flame speed and the average flow deflection. Instead, local effects at the flame tip, such as local flame quenching and local boundary layer separation have to be accounted for.

The unconfined BLF process of a tube burner without burner rim cooling was also investigated in this work. The stable flame in the present simulations was cone shaped and the flow inside the premixing tube was not influenced by combustion. The quenching configuration at the burner rim was similar to sidewall quenching and the corresponding quenching distances were small enough to prevent a gap flow of fresh gas between the burner rim and the flame. The unconfined BLF simulations showed that upstream flame propagation is initiated when the flame speed temporarily exceeds the axial gas velocity in the turbulent boundary layer. A low velocity turbulence structure lifts the flame into the premixing tube directly at the burner rim. The wall distance of the leading flame tip trajectory is thereby constant and similar to the sidewall quenching distance. The current simulation results therefore indicate that the critical gradient model is valid for unconfined BLF when calculating the critical gradient from the minimum temporary local gas velocity instead of the average gas velocity at the quenching distance. As soon as the flame is located inside the premixing duct, the redirection of burnt gas by the tube wall leads to flow deflection ahead of the flame front. The following propagation process is therefore similar to the confined BLF process. It was furthermore found that the burner rim temperature mainly influences the unconfined flashback limits by increasing the local flame speeds near the wall. The flame speeds are increased by hydrogen enrichment due to Soret diffusion and by elevating the unburnt gas temperature. The influence of wall temperature on the quenching distance in contrast was found to be small.

The simulations of a tube burner without burner rim cooling showed some differences to previous experimental results of a channel burner with burner rim cooling. In previous experimental results, the stable flame was not cone

shaped, a gap flow was observed between the burner rim and the flame front and flashback was initiated at a certain distance downstream of the burner rim. The reason for the discrepancy in numerical and experimental flashback process could not be clarified by the current simulations alone. The discrepancies are either caused by differences in burner rim cooling between the different experimental configurations or by an inaccurate representation of flow pattern at the burner rim in the numerical simulations. Further numerical simulations of different burner configurations with different wall temperatures should therefore be conducted in future studies.

At last, the numerical simulations pointed out some deficiencies in analytical flashback prediction models. It was shown that the Stratford separation criterion is not valid in confined BLF and that the pressure rise ahead of the flame front is overestimated in the analytical prediction model for confined BLF. In addition, the analytical prediction model does not take the influence of the quenching distance and of the local separation zone size on flashback limits into account. Instead, the analytical prediction model falsely assumed that confined BLF limits only depend on the turbulent flame speed and the expansion ratio. For the unconfined flashback prediction model it was found that the prediction quality is strongly influenced by the value of reaction progress variable chosen for the flame angle evaluation and by the flame generated turbulence model. Both analytical models can nevertheless be regarded as valid flashback prediction models, which are capable of accurately accounting for parameters such as the fuel composition, preheat temperature and the turbulent duct flow on flashback limits.

The presented results of confined and unconfined BLF obtained with LES underline the importance of numerical simulations for a detailed analysis of the flashback process. The deficiencies of analytical flashback models additionally underline the importance of numerical simulations for predicting BLF limits of different burners at different operating conditions. There are however still open questions that should be addressed in future studies of BLF. The differences in the unconfined flashback process observed in experiments and numerical simulations should be clarified. The influence of the mixture averaged formulation of the diffusion model on the predicted BLF limits could

---

be investigated and confined BLF should be simulated at even higher pressure levels. The investigation of different burner types and higher pressure levels is however limited by the high computing times associated with the quasi-laminar combustion model. This could be prevented by applying combustion models which model the influence of SGS turbulence on combustion and still incorporate the sophisticated diffusion processes that characterize the combustion of hydrogen-rich fuels. A possible candidate for this application would be the linear eddy model [99], for example.



# Bibliography

- [1] ANSYS. ANSYS Fluent Theory Guide, 2015.
- [2] ANSYS. ANSYS Fluent User's Guide, 2015.
- [3] G. Baumgartner, L. R. Böck, and T. Sattelmayer. Experimental Investigation of the Transition Mechanism From Stable Flame to Flashback in a Generic Premixed Combustion System With High-Speed Micro-PIV and Micro-PLIF Combined With Chemiluminescence Imaging. In *Volume 4A: Combustion, Fuels and Emissions*, Montreal, Quebec, Canada, June 2015. American Society of Mechanical Engineers.
- [4] G. Baumgartner and T. Sattelmayer. Experimental Investigation of the Flashback Limits and Flame Propagation Mechanisms for Premixed Hydrogen-Air Flames in Non-Swirling and Swirling Flow. In *Volume 1A: Combustion, Fuels and Emissions*, page V01AT04A010, San Antonio, Texas, USA, June 2013. ASME.
- [5] G. M. Baumgartner. *Flame Flashback in Premixed Hydrogen-Air Combustion Systems*. PhD thesis, Universität München, 2014.
- [6] J. K. Bechtold and M. Matalon. The Dependence of the Markstein Length on Stoichiometry. *Combustion and Flame*, 127(1-2):1906–1913, 2001.
- [7] H. Blasius. Das Ähnlichkeitsgesetz bei Reibungsvorgängen in Flüssigkeiten. In Verein deutscher Ingenieure, editor, *Mitteilungen über Forschungsarbeiten auf dem Gebiete des Ingenieurwesens*, pages 1–41. Springer Berlin Heidelberg, Berlin, Heidelberg, 1913.

- [8] L. R. Böck. *Deflagration-to-Detonation Transition and Detonation Propagation in H<sub>2</sub>-Air Mixtures with Transverse Concentration Gradients*. PhD Thesis, Technische Universität München, 2015.
- [9] O. Bolland and H. Undrum. A Novel Methodology for Comparing CO<sub>2</sub> Capture Options for Natural Gas-Fired Combined Cycle Plants. *Advances in Environmental Research*, 7(4):901–911, 2003.
- [10] L. E. Bollinger and R. Edse. Effect of Burner-Tip Temperature on Flash Back of Turbulent Hydrogen-Oxygen Flames. *Industrial & Engineering Chemistry*, 48(4):802–807, 1956.
- [11] H. Bongers and de Goey, L. P. H. The Effect of Simplified Transport Modeling on the Burning Velocity of Laminar Premixed Flames. *Combustion Science and Technology*, 175(10):1915–1928, 2003.
- [12] R. Borghi. Turbulent Combustion Modelling. *Progress in Energy and Combustion Science*, 14(4):245–292, 1988.
- [13] D. Bradley, M. Lawes, Kexin Liu, S. Verhelst, and R. Woolley. Laminar Burning Velocities of Lean Hydrogen-Air Mixtures at Pressures up to 1.0 MPa. *Combustion and Flame*, 149(1-2):162–172, April 2007.
- [14] R. S. Brokaw. Predicting Transport Properties of Dilute Gases. *Industrial & Engineering Chemistry Process Design and Development*, 8(2):240–253, 1969.
- [15] M. P. Burke, M. Chaos, Y. Ju, F. L. Dryer, and S. J. Klippenstein. Comprehensive H<sub>2</sub>/O<sub>2</sub> Kinetic Model for High-Pressure Combustion. *International Journal of Chemical Kinetics*, 44(7):444–474, 2012.
- [16] C. Chin, A. S. H. Ooi, I. Marusic, and H. M. Blackburn. The Influence of Pipe Length on Turbulence Statistics Computed from Direct Numerical Simulation Data. *Physics of Fluids*, 22(11):115107, 2010.
- [17] P. Clavin. Dynamic Behavior of Premixed Flame Fronts in Laminar and Turbulent Flows. *Progress in Energy and Combustion Science*, 11(1):1–59, 1985.

- [18] N. Clemens and V. Raman. Large Eddy Simulation Modeling of Flashback and Flame Stabilization in Hydrogen-Rich Gas Turbines Using a Hierarchical Validation Approach.
- [19] O. Colin, F. Ducros, D. Veynante, and T. Poinso. A Thickened Flame Model for Large Eddy Simulations of Turbulent Premixed Combustion. *Physics of Fluids*, 12(7):1843–1863, 2000.
- [20] F. Contino, H. Jeanmart, T. Lucchini, and G. D’Errico. Coupling of In Situ Adaptive Tabulation and Dynamic Adaptive Chemistry: An Effective Method for Solving Combustion in Engine Simulations. *Proceedings of the Combustion Institute*, 33(2):3057–3064, January 2011.
- [21] H. F. Coward and F. Brinsley. CLXXIV. The Dilution-Limits of Inflammability of Gaseous Mixtures. Part I. The Determination of Dilution-Limits. Part II. The Lower Limits for Hydrogen, Methane, and Carbon Monoxide in Air. *Journal of the Chemical Society, Transactions*, 105(0):1859–1885, 1914.
- [22] F. Dabireau, B. Cuenot, O. Vermorel, and T. Poinso. Interaction of Flames of  $H_2 + O_2$  with Inert Walls. *Combustion and Flame*, 135(1-2):123–133, 2003.
- [23] B. Dam, N. Love, and A. Choudhuri. Flashback Propensity of Syngas Fuels. *Fuel*, 90(2):618–625, February 2011.
- [24] S. Daniele, P. Jansohn, and K. Boulouchos. Flashback Propensity of Syngas Flames at High Pressure: Diagnostic and Control. In *Volume 2: Combustion, Fuels and Emissions, Parts A and B*, pages 1169–1175, Glasgow, UK, 2010. ASME.
- [25] L.P.H. de Goey, J.A. van Oijen, and R. J. M. Bastiaans. Premixed Turbulent Combustion Modelling with FGM Including Preferential Diffusion Effects. In *Verbrennung und Feuerung : 24. Deutscher Flammentag ; Tagung Bochum, 16. und 17. September 2009*, volume 2056 of *VDI-Berichte*, pages 379–384. VDI-Verlag, 2009.
- [26] de Swart, J. A. M., R. J. M. Bastiaans, J. A. van Oijen, de Goey, L. P. H., and R. S. Cant. Inclusion of Preferential Diffusion in Simulations of Premixed

- Combustion of Hydrogen/Methane Mixtures with Flamelet Generated Manifolds. *Flow, Turbulence and Combustion*, 85(3-4):473–511, 2010.
- [27] J. W. Deardorff. Stratocumulus-Capped Mixed Layers Derived from a Three-Dimensional Model. *Boundary-Layer Meteorology*, 18(4):495–527, 1980.
- [28] G. Dixon-Lewis. Flame Structure and Flame Reaction Kinetics. II. Transport Phenomena in Multicomponent Systems. *Proceedings of the Royal Society A: Mathematical, Physical and Engineering Sciences*, 307(1488):111–135, 1968.
- [29] Z. Duan, B. Shaffer, and V. McDonell. Study of Fuel Composition, Burner Material, and Tip Temperature Effects on Flashback of Enclosed Jet Flame. *Journal of Engineering for Gas Turbines and Power*, 135(12):121504, 2013.
- [30] Z. Duan, B. Shaffer, V. McDonell, G. Baumgartner, and T. Sattelmayer. Influence of Burner Material, Tip Temperature, and Geometrical Flame Configuration on Flashback Propensity of H<sub>2</sub>-Air Jet Flames. *Journal of Engineering for Gas Turbines and Power*, 136(2):021502, 2014.
- [31] G. L. Dugger. Flame Stability of Preheated Propane-Air Mixtures. *Industrial & Engineering Chemistry*, 47(1):109–114, 1955.
- [32] C. Duwig, K. Nogenmyr, C. Chan, and M. J. Dunn. Large Eddy Simulations of a Piloted Lean Premix Jet Flame Using Finite-Rate Chemistry. *Combustion Theory and Modelling*, 15(4):537–568, 2011.
- [33] T. Echekki and E. Mastorakos, editors. *Turbulent Combustion Modeling: Advances, New Trends and Perspectives*, volume 95 of *Fluid Mechanics and Its Applications*. Springer Science + Business Media B.V., Dordrecht, 2011.
- [34] C. Eichler, G. Baumgartner, and T. Sattelmayer. Experimental Investigation of Turbulent Boundary Layer Flashback Limits for Premixed Hydrogen-Air Flames Confined in Ducts. *Journal of Engineering for Gas Turbines and Power*, 134(1):011502, 2012.

- [35] C. Eichler and T. Sattelmayer. Experiments on Flame Flashback in a Quasi-2D Turbulent Wall Boundary Layer for Premixed Methane-Hydrogen-Air Mixtures. *Journal of Engineering for Gas Turbines and Power*, 133(1):011503, 2011.
- [36] C. T. Eichler. *Flame Flashback in Wall Boundary Layers of Premixed Combustion Systems*. Verlag Dr. Hut, 2011.
- [37] G. K. El Khoury, P. Schlatter, A. Noorani, P. F. Fischer, G. Brethouwer, and A. V. Johansson. Direct Numerical Simulation of Turbulent Pipe Flow at Moderately High Reynolds Numbers. *Flow, Turbulence and Combustion*, 91(3):475–495, October 2013.
- [38] A. Endres and T. Sattelmayer. Large Eddy Simulation of Confined Turbulent Boundary Layer Flashback of Premixed Hydrogen-Air Flames. *International Journal of Heat and Fluid Flow*, 72:151–160, August 2018.
- [39] A. Endres and T. Sattelmayer. Numerical Investigation of Pressure Influence on the Confined Turbulent Boundary Layer Flashback Process. *Fluids*, 4(3):146, August 2019.
- [40] A. Ern and V. Giovangigli. Thermal Diffusion Effects in Hydrogen-Air and Methane-Air Flames. *Combustion Theory and Modelling*, 2(4):349–372, 1998.
- [41] J. H. Ferziger and M. Perić. *Computational Methods for Fluid Dynamics*. Springer Berlin Heidelberg, Berlin, Heidelberg and s.l., third, revised edition edition, 2002.
- [42] A. Fick. Über Diffusion. *Annalen der Physik und Chemie*, 170(1):59–86, 1855.
- [43] B. Fine. Stability Limits and Burning Velocities of Laminar Hydrogen-Air Flames at Reduced Pressure, 1956.
- [44] B. Fine. *Effect of Initial Temperature on the Flashback of Laminar and Turbulent Burner Flames*. National Advisory Committee for Aeronautics, Cleveland, OH, 1958.

- [45] B. Fine. The Flashback of Laminar and Turbulent Burner Flames at Reduced Pressure. *Combustion and Flame*, 2(3):253–266, 1958.
- [46] D. H. France. Flashback of Laminar Monoport Burner Flames. *Journal of the Institute of Fuel*, 50(404):147–152, 1977.
- [47] J. Fritz, M. Kröner, and T. Sattelmayer. Flashback in a Swirl Burner with Cylindrical Premixing Zone. *Journal of Engineering for Gas Turbines and Power*, 126(2):276–, 2004.
- [48] C. Fureby. Comparison of Flamelet and Finite Rate Chemistry LES for Premixed Turbulent Combustion. In *45th AIAA Aerospace Sciences Meeting and Exhibit*, page 1413, 2007.
- [49] C. Fureby, G. Tabor, H. G. Weller, and A. D. Gosman. A Comparative Study of Subgrid Scale Models in Homogeneous Isotropic Turbulence. *Physics of Fluids*, 9(5):1416–1429, 1997.
- [50] E. Garnier, M. Mossi, P. Sagaut, P. Comte, and M. Deville. On the Use of Shock-Capturing Schemes for Large-Eddy Simulation. *Journal of Computational Physics*, 153(2):273–311, 1999.
- [51] P. Gerlinger. *Numerische Verbrennungssimulation: Effiziente Numerische Simulation Turbulenter Verbrennung*. Springer-Verlag Berlin Heidelberg, Berlin, Heidelberg, 2005.
- [52] M. Germano, U. Piomelli, P. Moin, and W. H. Cabot. A Dynamic Subgrid-Scale Eddy Viscosity Model. *Physics of Fluids A: Fluid Dynamics*, 3(7):1760–1765, 1991.
- [53] D. G. Goodwin, H. K. Moffat, and R. L. Speth. *Cantera: An Object-Oriented Software Toolkit for Chemical Kinetics, Thermodynamics, and Transport Processes*, 2017.
- [54] M. Götz, J. Lefebvre, F. Mörs, A. McDaniel Koch, F. Graf, S. Bajohr, R. Reimert, and T. Kolb. Renewable Power-to-Gas: A Technological and Economic Review. *Renewable Energy*, 85:1371–1390, January 2016.

- [55] J. F. Grcar. A New Type of Steady and Stable, Laminar, Premixed Flame in Ultra-Lean, Hydrogen-Air Combustion. *Proceedings of the Combustion Institute*, 32(1):1011–1018, 2009.
- [56] J. F. Grcar, J. B. Bell, and M. S. Day. The Soret Effect in Naturally Propagating, Premixed, Lean, Hydrogen-Air Flames. *Proceedings of the Combustion Institute*, 32(1):1173–1180, 2009.
- [57] A. Gruber, J. H. Chen, D. Valiev, and C. K. Law. Direct Numerical Simulation of Premixed Flame Boundary Layer Flashback in Turbulent Channel Flow. *Journal of Fluid Mechanics*, 709:516–542, 2012.
- [58] A. Gruber, A. R. Kerstein, D. Valiev, C. K. Law, H. Kolla, and J. H. Chen. Modeling of Mean Flame Shape During Premixed Flame Flashback in Turbulent Boundary Layers. *Proceedings of the Combustion Institute*, 35(2):1485–1492, 2015.
- [59] A. Gruber, R. Sankaran, E. R. Hawkes, and J. H. Chen. Turbulent Flame-Wall Interaction: A Direct Numerical Simulation Study. *Journal of Fluid Mechanics*, 658:5–32, 2010.
- [60] J. Grumer. Predicting Burner Performance with Interchanged Fuel Gases. *Industrial & Engineering Chemistry*, 41(12):2756–2761, 1949.
- [61] J. Grumer and M. E. Harris. Flame-Stability Limits of Methane, Hydrogen, and Carbon Monoxide Mixtures. *Industrial & Engineering Chemistry*, 44(7):1547–1553, 1952.
- [62] J. Gullbrand and F. K. Chow. The Effect of Numerical Errors and Turbulence Models in Large-Eddy Simulations of Channel Flow, with and without Explicit Filtering. *Journal of fluid mechanics*, 495:323–341, 2003.
- [63] E. Hairer and G. Wanner. *Solving Ordinary Differential Equations II*, volume 14 of *Springer Series in Computational Mathematics*. Springer Berlin Heidelberg, Berlin, Heidelberg, 1996.
- [64] M. Hassanaly, H. Koo, C. F. Lietz, S. T. Chong, and V. Raman. A Minimally-Dissipative Low-Mach Number Solver for Complex Reacting Flows in OpenFOAM. *Computers & Fluids*, 162:11–25, 2018.

- [65] C. Heeger, R. L. Gordon, M. J. Tummers, T. Sattelmayer, and A. Dreizler. Experimental Analysis of Flashback in Lean Premixed Swirling Flames: Upstream Flame Propagation. *Experiments in Fluids*, 49(4):853–863, 2010.
- [66] J. M. Heimerl and T. P. Coffee. Transport Algorithms for Methane Flames. *Combustion Science and Technology*, 34(1-6):31–43, 1983.
- [67] S. Hickel. *Implicit Turbulence Modeling for Large-Eddy Simulation*. PhD thesis, Technische Universität München, 2008.
- [68] J. O. Hirschfelder, R. B. Bird, and E. L. Spotz. The Transport Properties of Gases and Gaseous Mixtures. II. *Chemical Reviews*, 44(1):205–231, 1949.
- [69] V. Hoferichter. *Boundary Layer Flashback in Premixed Combustion Systems*. Energietechnik. Dr. Hut, München, 2017.
- [70] V. Hoferichter, C. Hirsch, and T. Sattelmayer. Analytic Prediction of Unconfined Boundary Layer Flashback Limits in Premixed Hydrogen-Air Flames. *Combustion Theory and Modelling*, 136:1–37, 2016.
- [71] V. Hoferichter, C. Hirsch, and T. Sattelmayer. Prediction of Confined Flame Flashback Limits Using Boundary Layer Separation Theory. *Journal of Engineering for Gas Turbines and Power*, 139(2):021505, 2017.
- [72] Vera Hoferichter and Thomas Sattelmayer. Boundary Layer Flashback in Premixed Hydrogen-Air Flames With Acoustic Excitation. *Journal of Engineering for Gas Turbines and Power*, 140(5):051502, 2018.
- [73] T. Holzmann. *Mathematics, Numerics, Derivations and OpenFOAM*. Holzmann CFD, 2016.
- [74] International Energy Agency. *World Energy Outlook 2017*. World Energy Outlook. OECD, November 2017.
- [75] H. Jasak. *Error Analysis and Estimation for Finite Volume Method with Applications to Fluid Flow*. PhD thesis, University of London, 1996.
- [76] H. Jasak. Numerical Solution Algorithms for Compressible Flows. Lecture Notes, Faculty of Mechanical Engineering and Naval Architecture,

- University of Zagreb, <https://de.scribd.com/document/27927305/Numerical-Solution-Algorithms-for-Compressible-Flows>, 2006. Accessed on 4 November 2019.
- [77] W. P. Jones, A. J. Marquis, and F. Wang. Large Eddy Simulation of a Premixed Propane Turbulent Bluff Body Flame Using the Eulerian Stochastic Field Method. *Fuel*, 140:514–525, 2015.
- [78] W. P. Jones and S. Navarro-Martinez. Large Eddy Simulation of Autoignition with a Subgrid Probability Density Function Method. *Combustion and Flame*, 150(3):170–187, 2007.
- [79] A. Kalantari and V. McDonell. Boundary Layer Flashback of Non-Swirling Premixed Flames: Mechanisms, Fundamental Research, and Recent Advances. *Progress in Energy and Combustion Science*, 61:249–292, July 2017.
- [80] A. Kalantari, E. Sullivan-Lewis, and V. McDonell. Flashback Propensity of Turbulent Hydrogen-Air Jet Flames at Gas Turbine Premixer Conditions. *Journal of Engineering for Gas Turbines and Power*, 138(6):061506, 2016.
- [81] A. Kalantari, E. Sullivan-Lewis, and V. McDonell. Application of a Turbulent Jet Flame Flashback Propensity Model to a Commercial Gas Turbine Combustor. *Journal of Engineering for Gas Turbines and Power*, 139(4):041506, 2017.
- [82] R. J. Kee, G. Dixon-Lewis, J. Warnatz, M. E. Coltrin, J. A. Miller, and H. K. Moffat. Transport: A Software Package for the Evaluation of Gas-Phase, Multicomponent Transport Properties. *Chemkin Collection*, 1999.
- [83] R. J. Kee, F. M. Rupley, E. Meeks, and J. A. Miller. CHEMKIN-III: A FORTRAN Chemical Kinetics Package for the Analysis of Gas-Phase Chemical and Plasma Kinetics. *Sandia national laboratories report SAND96-8216*, 1996.
- [84] J. O. Keller, L. Vaneveld, D. Korschelt, G. L. Hubbard, A. F. Ghoniem, J. W. Daily, and A. K. Oppenheim. Mechanism of Instabilities in Turbulent Combustion Leading to Flashback. *Aiaa Journal*, 20(2):254–262, 1982.

- [85] L. N. Khitrin, P. B. Moin, D. B. Smirnov, and V. U. Shevchuk. Peculiarities of Laminar- and Turbulent-Flame Flashbacks. *Symposium (International) on Combustion*, 10(1):1285–1291, 1965.
- [86] F. Kieseewetter, C. Hirsch, J. Fritz, M. Kröner, and T. Sattelmayer. Two-Dimensional Flashback Simulation in Strongly Swirling Flows. In *Volume 2: Turbo Expo 2003*, pages 293–300, Atlanta, Georgia, USA, 2003. ASME.
- [87] F. Kieseewetter, M. Konle, and T. Sattelmayer. Analysis of Combustion Induced Vortex Breakdown Driven Flame Flashback in a Premix Burner With Cylindrical Mixing Zone. *Journal of Engineering for Gas Turbines and Power*, 129(4):929, 2007.
- [88] W. Kim and S. Menon. A New Dynamic One-Equation Subgrid-Scale Model for Large Eddy Simulations. In *33rd Aerospace Sciences Meeting and Exhibit*, page 356, 1995.
- [89] M. Konle, F. Kieseewetter, and T. Sattelmayer. Simultaneous High Repetition Rate PIV-LIF-Measurements of CIVB Driven Flashback. *Experiments in Fluids*, 44(4):529–538, April 2008.
- [90] M. Konle and T. Sattelmayer. Interaction of Heat Release and Vortex Breakdown During Flame Flashback Driven by Combustion Induced Vortex Breakdown. *Experiments in Fluids*, 47(4-5):627–635, October 2009.
- [91] K. K. Kuo and R. Acharya. *Applications of Turbulent and Multiphase Combustion*. Wiley, Hoboken, NJ, 2012.
- [92] V. Kurdyumov, E. Fernández-Tarrazo, J.-M. Truffaut, J. Quinard, A. Wangher, and G. Searby. Experimental and Numerical Study of Premixed Flame Flashback. *Proceedings of the Combustion Institute*, 31(1):1275–1282, 2007.
- [93] L. D. Landau. On the Theory of Slow Combustion. *Acta Physicochim (USSR)*, 19:77–85, 1944.

- [94] C. K. Law. *Combustion Physics*. Cambridge University Press, Cambridge and New York, 2006.
- [95] S. T. Lee and J. S. T'ien. A Numerical Analysis of Flame Flashback in a Premixed Laminar System. *Combustion and Flame*, 48:273–285, 1982.
- [96] J. Legier, T. Poinso, and D. Veynante. Dynamically Thickened Flame LES Model for Premixed and Non-Premixed Turbulent Combustion. In *Proc. of the Summer Program*, pages 157–168, 2000.
- [97] B. Lewis and G. von Elbe. Stability and Structure of Burner Flames. *The Journal of Chemical Physics*, 11(2):75–97, 1943.
- [98] J. Li, Z. Zhao, A. Kazakov, and F. L. Dryer. An Updated Comprehensive Kinetic Model of Hydrogen Combustion. *International Journal of Chemical Kinetics*, 36(10):566–575, 2004.
- [99] S. Li, Y. Zheng, D. Mira, S. Li, M. Zhu, and X. Jiang. A Large-Eddy Simulation–Linear-Eddy Model Study of Preferential Diffusion Processes in a Partially Premixed Swirling Combustor With Synthesis Gases. *Journal of Engineering for Gas Turbines and Power*, 139(3):031501, 2017.
- [100] C. Lietz, M. Hassanaly, V. Raman, H. Kolla, J. Chen, and A. Gruber. LES of Premixed Flame Flashback in a Turbulent Channel. In *52nd Aerospace Sciences Meeting*, Reston, Virginia, 2014. American Institute of Aeronautics and Astronautics.
- [101] T. Lieuwen, V. McDonell, E. Petersen, and D. Santavicca. Fuel Flexibility Influences on Premixed Combustor Blowout, Flashback, Autoignition and Instability. In *Volume 1: Combustion and Fuels, Education*, volume 2006, pages 601–615, Barcelona, Spain, 2006. ASME.
- [102] T. Lieuwen, V. McDonell, D. Santavicca, and T. Sattelmayer. Burner Development and Operability Issues Associated with Steady Flowing Syngas Fired Combustors. *Combustion Science and Technology*, 180(6):1169–1192, May 2008.

- [103] D. K. Lilly. The Representation of Small Scale Turbulence in Numerical Simulation Experiments. In *IBM Scientific Computing Symposium on environmental sciences*, pages 195–210, Yorktown heights, 1967.
- [104] Y. Liu. *Untersuchung zur Stationären Ausbreitung Turbulenter Vormischflammen*. Universtität Fridericiana Karlsruhe, 1991.
- [105] T. S. Lund. The Use of Explicit Filters in Large Eddy Simulation. *Computers & Mathematics with Applications*, 46(4):603–616, 2003.
- [106] R. M. M. Mallens and L. P. H. de Goey. Flash-Back of Laminar Premixed Methane/Air Flames on Slit and Tube Burners. *Combustion Science and Technology*, 136(1):41–54, 1998.
- [107] G. H. Markstein. *Nonsteady Flame Propagation*, volume v.75 of *AGAR-Dograph*. Elsevier Science, Burlington, 2014.
- [108] C. Mayer, J. Sangl, T. Sattelmayer, T. Lachaux, and S. Bernero. Study on the Operational Window of a Swirl Stabilized Syngas Burner Under Atmospheric and High Pressure Conditions. In *Volume 2: Combustion, Fuels and Emissions, Parts A and B*, pages 141–152, Vancouver, British Columbia, Canada, 2011. ASME.
- [109] P. Moin and J. Kim. Numerical Investigation of Turbulent Channel Flow. *Journal of fluid mechanics*, 118(-1):341, 1982.
- [110] R. D. Moser, J. Kim, and N. N. Mansour. Direct Numerical Simulation of Turbulent Channel Flow up to  $Re_{\tau}=590$ . *Physics of Fluids*, 11(4):943–945, 1999.
- [111] T. Mukha and M. Liefvendahl. Large-Eddy Simulation of Turbulent Channel Flow. <https://www.it.uu.se/research/publications/reports/2015-014/2015-014.pdf>. Accessed on 6 September 2017.
- [112] United Nations. Paris Agreement. [https://treaties.un.org/pages/ViewDetails.aspx?src=TREATY&mtdsg\\_no=XXVII-7-d&chapter=27&clang=\\_en](https://treaties.un.org/pages/ViewDetails.aspx?src=TREATY&mtdsg_no=XXVII-7-d&chapter=27&clang=_en), 2015. Accessed on 11 March 2019.

- [113] S. Navarro-Martinez, A. Kronenburg, and F. Di Mare. Conditional Moment Closure for Large Eddy Simulations. *Flow, Turbulence and Combustion*, 75(1-4):245–274, 2005.
- [114] F. Nozaki. Smagorinsky SGS Model in OpenFOAM. <http://caefn.com/openfoam/smagorinsky-sgs-model>, 2016. Accessed on 23 January 2018.
- [115] G. Patnaik and K. Kailasanath. Effect of Gravity on the Stability and Structure of Lean Hydrogen-Air Flames. *Symposium (International) on Combustion*, 23(1):1641–1647, 1991.
- [116] N. Peters. The Turbulent Burning Velocity for Large-Scale and Small-Scale Turbulence. *Journal of Fluid Mechanics*, 384:107–132, 1999.
- [117] N. Peters. *Turbulent Combustion*. Cambridge Monographs on Mechanics. Cambridge University Press, Cambridge England and New York, 2000.
- [118] H. Pitsch and L. Duchamp de Lageneste. Large-Eddy Simulation of Premixed Turbulent Combustion Using a Level-Set Approach. *Proceedings of the Combustion Institute*, 29(2):2001–2008, 2002.
- [119] T. Poinso. and D. Veynante. *Theoretical and Numerical Combustion*. Edwards, Philadelphia, 2. ed. edition, 2005.
- [120] S. B. Pope. The Statistical Theory of Turbulent Flames. *Philosophical Transactions of the Royal Society A: Mathematical, Physical and Engineering Sciences*, 291(1384):529–568, 1979.
- [121] S. B. Pope. PDF Methods for Turbulent Reactive Flows. *Progress in Energy and Combustion Science*, 11:119–192, 1985.
- [122] S. B. Pope. *Turbulent Flows*. Cambridge University Press, 2000.
- [123] S.B. Pope. Computationally efficient implementation of combustion chemistry using in situ adaptive tabulation. *Combustion Theory and Modelling*, 1(1):41–63, January 1997.

- [124] A. A. Putnam and R. A. Jensen. Application of Dimensionless Numbers to Flash-Back and Other Combustion Phenomena. *Symposium on Combustion and Flame, and Explosion Phenomena*, 3(1):89–98, 1948.
- [125] P. Sagaut. *Large Eddy Simulation for Incompressible Flows*. Springer Berlin Heidelberg, Berlin, Heidelberg, 2002.
- [126] T. Sattelmayer, C. Mayer, and J. Sangl. Interaction of Flame Flashback Mechanisms in Premixed Hydrogen-Air Swirl Flames. *Journal of Engineering for Gas Turbines and Power*, 138(1):011503, August 2015.
- [127] H. Schlichting and K. Gersten. *Boundary-Layer Theory*. Springer Berlin Heidelberg, Berlin, Heidelberg, 2017.
- [128] M. M. Schorr and J. Chalfin. Gas Turbine NOx Emissions Approaching Zero - Is It Worth the Price? *General Electric Power Generation, Report No. GER*, 4172, 1999.
- [129] B. Shaffer, Z. Duan, and V. McDonell. Study of Fuel Composition Effects on Flashback Using a Confined Jet Flame Burner. *Journal of Engineering for Gas Turbines and Power*, 135(1):011502, 2013.
- [130] J. Smagorinsky. General Circulation Experiments with the Primitive Equations: I. The Basic Experiment. *Monthly weather review*, 91(3):99–164, 1963.
- [131] S. Sogo and S. Yuasa. Flame Stretch Rate of Laminar Flame Base Just Before Flashback at Different Burner Temperatures. In *20th International Colloquium on the Dynamics of Explosions and Reactive Systems, Montreal, Canada, July, 2005*.
- [132] Z. S. Spakovszky. Thermal Energy, MIT Course 16, Fall 2002. Lecture Notes, Massachusetts Institute of Technology, <https://ocw.mit.edu/courses/aeronautics-and-astronautics/16-050-thermal-energy-fall-2002/lecture-notes/>, 2002. Accessed on 27 September 2019.
- [133] B. S. Stratford. The Prediction of Separation of the Turbulent Boundary Layer. *Journal of fluid mechanics*, 5(01):1–16, 1959.

- [134] W. Sutherland. LII. The Viscosity of Gases and Molecular Force. *Philosophical Magazine Series 5*, 36(223):507–531, 1893.
- [135] P. K. Sweby. High Resolution Schemes Using Flux Limiters for Hyperbolic Conservation Laws. *SIAM Journal on Numerical Analysis*, 21(5):995–1011, 1984.
- [136] G. Taylor. The Instability of Liquid Surfaces when Accelerated in a Direction Perpendicular to their Planes. I. *Proceedings of the Royal Society of London. Series A, Mathematical and Physical Sciences*, 201(1065):192–196, 1950.
- [137] D. Thibaut and S. Candel. Numerical Study of Unsteady Turbulent Premixed Combustion: Application to Flashback Simulation. *Combustion and Flame*, 113(1-2):53–65, 1998.
- [138] A. Trouvé and T. Poinsot. The Evolution Equation for the Flame Surface Density in Turbulent Premixed Combustion. *Journal of Fluid Mechanics*, 278:1–31, November 1994.
- [139] J. A. Turner. Sustainable Hydrogen Production. *Science*, 305(5686):972–974, August 2004.
- [140] S. R. Turns. *An Introduction to Combustion: Concepts and Applications*. McGraw-Hill Series in Mechanical Engineering. McGraw-Hill, Boston, Mass., 2. ed. edition, 2000.
- [141] E. R. van Driest. On Turbulent Flow Near a Wall. *Journal of the Aeronautical Sciences*, 23:1007–1011, 1956.
- [142] D. W. van Krevelen and H.A.G. Chermin. Generalized Flame Stability Diagram for the Prediction of Interchangeability of Gases. *Symposium (International) on Combustion*, 7(1):358–368, 1958.
- [143] M. Voldsund, K. Jordal, and R. Anantharaman. Hydrogen Production with CO<sub>2</sub> Capture. *International Journal of Hydrogen Energy*, 41(9):4969–4992, 2016.

- [144] G. von Elbe and M. Mentser. Further Studies of the Structure and Stability of Burner Flames. *The Journal of Chemical Physics*, 13(2):89–100, February 1945.
- [145] H. G. Weller, G. Tabor, H. Jasak, and C. Fureby. A Tensorial Approach to Computational Continuum Mechanics Using Object-Oriented Techniques. *Computers in Physics*, 12(6):620, 1998.
- [146] J. R. Welty. *Fundamentals of Momentum, Heat, and Mass Transfer*. Wiley, Hoboken, NJ, 5. ed. edition, 2008.
- [147] F. A. Williams. *Combustion Theory: The Fundamental Theory of Chemically Reacting Flow Systems*. Combustion Science and Engineering Series. Perseus Books, Cambridge, Mass., 2. ed. edition, 1985.
- [148] F. A. Williams and J. F. Grcar. A Hypothetical Burning-Velocity Formula for Very Lean Hydrogen-Air Mixtures. *Proceedings of the Combustion Institute*, 32(1):1351–1357, 2009.
- [149] K. Wohl. Quenching, Flash-Back, Blow-Off – Theory and Experiment. *Symposium (International) on Combustion*, 4(1):68–89, 1953.
- [150] A. Yoshizawa. Bridging Between Eddy-Viscosity-Type and Second-Order Turbulence Models through a Two-Scale Turbulence Theory. *Phys. Rev. E*, 48(1):273–281, 1993.
- [151] Z. Zhou, F. E. Hernández-Pérez, Y. Shoshin, J. A. van Oijen, and de Goey, L. P. H. de. Effect of Soret Diffusion on Lean Hydrogen/Air Flames at Normal and Elevated Pressure and Temperature. *Combustion Theory and Modelling*, 21(5):879–896, 2017.